GRAIN-RESOLVED STATISTICAL ANALYSIS OF IN-SITU STRAIN FIELDS WITH COMBINED IMAGE CORRELATION AND ORIENTATION MAPPING

by

Olcay Türkoğlu

B.S., Mechanical Engineering, ITU, 2010

M.S., Materials and Manufacturing, ITU, 2013

Submitted to the Institute for Graduate Studies in
Science and Engineering in partial fulfillment of
the requirements for the degree of
Doctor of Philosophy

Graduate Program in Mechanical Engineering

Boğaziçi University

2024

ACKNOWLEDGEMENTS

Reaching this point in my academic journey would not have been possible without the unwavering support and significant contributions of numerous individuals.

First and foremost, heartfelt thanks to my parents, the very foundation of my existence. Their love and support have been instrumental throughout my life, enabling me to attain this degree. From childhood to adulthood, they provided unwavering support, allowing me the freedom to shape my own path. As an adult, I now comprehend the value of growing up with an open mind and freedom, and my gratitude for their love and support knows no bounds. To my late father, I am certain that you are observing this milestone and the conclusion of my PhD journey, and I am forever proud to be your child. To my mother, I acknowledge the moments of patience lost during this challenging PhD and studentship, but the good news is that officially, I am no longer a student (though I will always be a perpetual learner). Also, I thank my brother, Tevfik, for being there.

I extend my gratitude to my advisor, Assoc. Prof. Dr. C. Can Aydıner, whose continuous support and tireless collaboration significantly contributed to my research career. Without his wisdom and understanding, attaining this degree would have been inconceivable. I am grateful for all that he has done for me. I also express my thanks to all current and past members of my thesis committee, Assoc. Prof. Dr. Ali Özgün Konca, Dr. Sertan Alkan, Prof. Dr. Nuri Ersoy, Prof. Dr. Günay Anlaş, and Assoc. Prof. Dr. Jeremy Kyle Mason, for their invaluable comments and support.

Special appreciation is reserved for Dr. Eda Aydoğan from Metallurgical and Materials Engineering Faculty, METU, for facilitating EBSD scans throughout a whole weekend. I extend my sincere thanks to graduate student Yeşim Yalçın for operating SEM and EBSD scans at the SEM Laboratory, METU. I also appreciate the earlier support for pilot EBSD scans provided by Dr. Mert Efe and Dr. Baran Güler.

Special recognition and thanks are due to all past and present members of the Mechanics of Advanced Materials Laboratory, Mechanical Engineering Department, Boğaziçi University. Special awards go to Assoc. Prof. Dr. C. Can Aydıner for the "Blackest Coffee Award", Dr. Nima Şafak (Shafagi) for the "Longest Studentship-Mate Award", Dr. Enver Kapan for the "Loudest Singer in the Lab Award", Buğra Üçel for the "Calmest in the Lab Award", Necdet Ali Özdür for the "Meal Provider Award", Sefer Can Erman for the "Most Agile in Action Award", and Hasan Can Kubat for the "Gamer in the Lab Award". I thank all of them for their warm friendship and endless support during my PhD journey.

I extend special thanks to the Mechanical Engineering Department of Işık University, including the late Sadettin Ozan, a remarkable technician, mechanic, and teacher; Prof. Dr. Ahmet Aran, my first employer and mentor in academia; and Prof. Dr. Mehmet Demirkol, my first influencer in materials science research, my Master of Science thesis advisor, and an outstanding administrator. I am sincerely grateful for their contributions to my academic journey. I also express my thanks to all other colleagues in the department for their support and friendship, including Assoc. Prof. Dr. Erkin Dinçmen, Assoc. Prof. Dr. Umut Karagüzel, Dr. Ali Taner Kuzu, Dr. Hıdır Maral, Dr. Onur Keskin, Dr. Kerem Altun, Dr. Sinan Eren Yalçın, Tunca Zeki Berkkurt, Buğra Kaplan, Anıl Gökhan Göktaş, and Burak Kılıç.

Additionally, my heartfelt thanks go to my friends Dolunay Uğur, Onur Akaydın, and Desen Karabağlar, who have been steadfast companions for almost two decades. Your presence has made the good times fantastic and the tough times bearable.

Last but certainly not least, I extend my thanks to my one-year-old niece, Duru. Her presence has brought light to our family and provided a source of peace and joy, helping me overcome the challenges of the last few stressful years.

ABSTRACT

GRAIN-RESOLVED STATISTICAL ANALYSIS OF IN-SITU STRAIN FIELDS WITH COMBINED IMAGE CORRELATION AND ORIENTATION MAPPING

Metallic polycrystals, the common form of engineering materials, are complex composites of anisotropic grains. For these materials, there is an intense drive to form high-fidelity crystal-plasticity models that build the mechanical response from the grain scales since such models can represent multiple microstructures of the same material without the need for repetitive experimentation. Historically, bulk diffraction has been the primary experimental method in validating these models. More recently, however, the real space method of digital image correlation (DIC) has been implemented with in-situ microscopy, generating immense data sets of high statistical significance and resolution, potentially offering a multi-scale validation of such models. This thesis features an area-scanning, high-resolution DIC variant with optical microscopy that has nominal 1 μm data spacing and thousands of grains field coverage, conducted in-situ with fine load intervals. The distinguishing feature of the current effort, however, is to form and incorporate a grain mask that will allow singling out strain fields of individual grains and their subzones. As critically, grain orientations are also predetermined over identical fields by electron back scatter diffraction. A basic material is opted in this study, high-purity FCC nickel, though its large anisotropy ratio (2.5) is opted for high strain heterogeneity among grains that will be the subject of a statistical analysis. The goals of the study are two fold, associated with elastic and plastic strains. The first part explores the measurement of elastic strains, which DIC is typically not sufficiently sensitive for, by improving accuracy with over-the-grain averaging. The measurement of grain-averaged elastic strain through partial unloads is then used to offer a technique for grain-averaged stress estimation. The second part explores the statistical trends in the plastic strain accommodation of grains with differing orientation and sizes.

ÖZET

İMGE KORELASYONU VE KRİSTAL YÖNÜ BELİRLEMELERİ İLE TANECİK GERİNİM ALANLARININ İSTATİKSEL ANALİZİ

Metalik polikristaller, mühendislik malzemelerinin yaygın formu olup, anizotropik tanelerden oluşan karmaşık kompozitleridir. Bu tür malzemeler için, taneler arası ölçeklerde mekanik cevap veren yüksek sadakatli kristal-plastisite modelleri oluşturma konusunda yoğun bir çaba vardır. Çünkü bu tür modeller aynı malzemenin farklı mikroyapılarını yeni deneyler gerektirmeden yansıtabilir. Tarihsel olarak, büyük hacimli kırınım, bu modellerin doğrulanmasında ana deneysel teknik olmuştur. Ancak yakın zamanda, bir gerçek uzay tekniği olan dijital imge korelasyonu (DIC), in-situ mikroskopi ile birlikte uygulanıp yüksek istatistiksel öneme ve çözünürlüğe sahip büyük veriler oluşturabilmekte ve çok ölçekli modellerin doğrulanabilmesi için fırsat sunmaktadır. Bu tez, optik mikroskopi ile gerçekleştirilen, alan-taramalı yüksek çözünürlüklü bir DIC türünü içermekte olup 1 μm veri aralığı ile, in-situ ve hassas olarak yüklenen, binlerce taneciği kapsamına alır. Ancak çalışmanın en ayırt edici yönü, tanelerin tek tek gerinim alanlarını ve iç bölgelerini ayırt etmeye izin veren tane maskeleri oluşturmaktır. Bu tanelerin yönelimleri de elektron geri saçınım kırınımı (EBSD) ile önceden belirlenmiştir. Malzeme olarak yüksek saflıkta FCC Nikel, yüksek anizotropi oranı (2.5) nedeniyle tanecikler arasında yüksek gerinim heterojenliği sağlamak için seçilmiştir ve bu da istatistiksel analizin konusu olacaktır. Çalışmanın iki ana hedefinin ilki elastik gerinimlerle ve ikincisi plastik gerinimlerle ilgilidir. İlkinde, elastik gerinimlerin ölçümü (genellikle DIC bunları ölçmek için yeterince duyarlı değildir), tane içi averajlama ile ölçüm hassasiyeti arttırılarak ele alınmaktadır. Kısmi yük boşaltmaları ile taneler için ortalama elastik gerinim ölçümleri yapılıp tanelere ait ortalama gerilme durumunu tahmin eden yöntem sunulmuştur. İkincisi ise, değişken yönelimli ve değişken boyutlu tanelerin plastik gerinim eğilimlerine ait istatistiksel trendleri incelemektedir.

TABLE OF CONTENTS

ACKNOWLEDGEMENTS iii
ABSTRACT v
ÖZET vi
LIST OF FIGURES ix
LIST OF TABLES xiv
LIST OF SYMBOLS xv
LIST OF ACRONYMS/ABBREVIATIONS xvi
1. INTRODUCTION 1
1.1. Motivation 1
1.2. Objectives and Scope 3
2. BACKGROUND AND LITERATURE REVIEW 5
2.1. Generalized Hooke's law 5
2.2. Deformation of FCC Crystals and Polycrystals 7
2.3. Polycrystal Models 10
2.3.1. Mean-field Models 10
2.3.2. Full-field Models 10
2.4. Experimental Data on Polycrystal Deformation 11
3. MATERIALS AND METHODS 18
3.1. Material 18
3.2. Tensile Specimen 19
3.3. Metallography 20
3.4. DIC Speckle Pattern Application 21
3.5. Experimental Setup 22
3.6. Experimental Procedure 24
3.6.1. EBSD and Orientation Mapping 24
3.6.2. Grain Mask Generation 25
3.6.3. Loading with in-situ Area Scanning Microscopic DIC 27
3.7. Data Analysis 28

3.7.1. DIC Algorithm 28
3.7.2. DIC Post-processing Tools 30
3.7.2.1. Image Stitching 30
3.7.2.2. Data Stitching 30
3.7.2.3. Grain Mask Mapping 31
3.7.2.4. Full-field Outlier Reduction 31
3.7.2.5. Binary Operations 32
3.7.3. DIC Reference Point Variation 32
3.7.4. Slip Trace Identification via Residual Intensity 33
3.8. Numerical Modeling of the Polycrystalline Aggregate 33
4. EVALUATION OF GRAIN-AVERAGED ELASTIC STRAINS 35
4.1. DIC averaging 35
4.2. Estimation of the average grain stress via a partial unload 36
4.3. Aggregate average 38
4.4. Selected individual grain evaluations 41
4.5. Statistics 48
5. EVALUATION OF GRAIN-RESOLVED PLASTIC DEFORMATION . . . 52
5.1. Plastic Deformation Heterogeneity 52
5.2. Grain-Resolved Plasticity 56
5.3. Statistical Interpretations on Grain-Resolved Plasticity 58
5.3.1. Directional Elastic Stiffness versus Strains 58
5.3.2. Schmid Factor versus Strains 60
5.3.3. Area versus Strains 63
5.3.4. Core versus Boundary Strain 63
5.4. Intragrain Plasticity 65
6. CONCLUSIONS 72
REFERENCES 74
APPENDIX A: ON THE SPECTRAL ANALYSIS PARAMETERS AND IMPLEMENTATION 84
APPENDIX B: COPYRIGHTS 87

LIST OF FIGURES

Figure 2.1. Perfect and partial dislocation 7

Figure 2.2. Schmid factor 9

Figure 2.3. SEM micrographs with twin plateau (a) 800x, and (b) 1500x magnification, recorded at the boundary of a tensile-twin-driven band (the separation of band indicated with a dashed line) [41] 12

Figure 2.4. Schmid factor maps of the plate at undeformed state for (a) basal slip, (b) prismatic slip (dash line shows corresponding deformation bands) [54]. 13

Figure 2.5. Comparison of strain maps between: (a) experiment and (b) simulation [37]. 14

Figure 2.6. Comparison of (a) DIC axial strain, (b) prismatic Schmid factor map. The loading is in the vertical direction [56]. 15

Figure 2.7. (a) Orientation maps (b) KAM maps of the initial sample and deformed sample, respectively (c) SF maps (d) IQ maps of the sample with strain at 0% and 11.9%, respectively [59]. 16

Figure 2.8. (a) Young modulus map (b) DIC Elastic Strain (c) CP-FEM analysis of grain in isotropic matrix [45]. 17

Figure 3.1. Tensile specimen after manufactured with WEDM. 19

Figure 3.2. Specimen surface after metallography a) Optical microscopy image (40X), b) SEM image (2000X) 20

Figure 3.3. (a) Speckle pattern and (b) Shannon entropy results over 4x4 grid of microscopic images. 22

Figure 3.4. (a) Schematic demonstration of DIC lines and 3-axis-stage (b) Photo of load frame and microscopic DIC line. 23

Figure 3.5. (a) Stitched microscopic image of ROI overlaid with grain mask, (b) EBSD orientation map of highlighted zone in (a), (c) Close-up view of grain mask overlaying onto microscopic image, (d) and (e) after and before speckle pattern application, (f) Pole figures. . . . 26

Figure 3.6. Strain calculations with (a) Newton-Raphson and (b) convolution based algorithms for same 2D displacement field [69]. 30

Figure 4.1. One dimensional analogy/verification of the stress estimation idea by fitting compliance S over the initial segment of the unload. . . 37

Figure 4.2. (a-b) Full-field average stress-strain curves wrt point O, (c) Full-field average unloading curves wrt point T (u0). 39

Figure 4.3. (a) An $150 \times 180\,\mu m^2$ grain neighborhood over which DIC results are shown with contour plots: (b) total axial strains, ε_{22} at point T (reference point O), (c) incremental axial strain field upon a nominal 15 MPa unload (second unload point u2 calculated with respect to top point T). See Figure 4.2 for load point definitions. . 40

Figure 4.4. (a) DIC image (grain A) RP-T, (b, c, d) RP-specific GMs (T, M, U). ε_{22} data clouds vs. σ_{app}, (e, f) at T, (g) at M, (h) at U, (i) grain A ε_{22} histograms, (j) grain-averaged, $\overline{\varepsilon}_{22}$, $\overline{\varepsilon}_{11}$, $\overline{\varepsilon}_{12}$, (k) Aligned $\overline{\varepsilon}_{22}$ results, (l) different-sized regions R, (m) r, for $\overline{\varepsilon}_{11}(R)$ and $\overline{\varepsilon}_{22}(R)$, (n) $\tilde{S}_{22}(R)$, (o) $\tilde{S}_{11}(R)$, (p) $\tilde{S}_{12}(R)$ vs. $\sqrt{A}$ of region R. 43

Figure 4.5. For grain B, (a) image-grain mask overlay (grain B at center) at reference point T, (b) grain-averaged strain components over the unload, (c) calculated stress slopes $\tilde{S}_{\alpha\beta}$; (d), (e), (f) similarly for grain C; (g), (h), (j) similarly for grain D. For more details, see the caption of Figure 4.4. 45

Figure 4.6. Reference point discrepancy, D (Equation 4.8, root mean square of $\delta\tilde{S}_{\alpha\beta}$ over its independent calculations with different reference points and limited field erosions). 49

Figure 4.7. Experimental grain-averaged stress slopes ($\tilde{S}_{\alpha\beta}$) versus spectral model (DAMASK) predictions ($\tilde{S}_{\alpha\beta,Dam}$) for (a)$\tilde{S}_{22}$, (b)$\tilde{S}_{11}$, and (c)$\tilde{S}_{12}$. . 49

Figure 4.8. For pre-unload point T, experimental grain-averaged stress ($\overline{\sigma}_{\alpha\beta}$) versus spectral analysis (DAMASK) predictions ($\overline{\sigma}_{\alpha\beta,Dam}$) for (a)$\overline{\sigma}_{22}$, (b)$\overline{\sigma}_{11}$, and (c)$\overline{\sigma}_{12}$. In part (b), 4 data points are below the shown range. 50

Figure 4.9. Effective axial compliance comparisons, (a) experimental versus isostress value, (b) spectral analysis (DAMASK) versus isostress value. 51

Figure 5.1. Applied stress vs macro strain curve with highlighted reference and deformed DIC points. 53

Figure 5.2. Histograms of (a) E_{hkl} and (b) absolute maximum Schmid factor. 53

Figure 5.3. Full field ε_{22} map on 5% average uni-axial macro strain 55

Figure 5.4. Full field ε_{11} map on 5% average uni-axial strain 55

Figure 5.5. Full field ε_{12} map on 5% average uni-axial strain 55

Figure 5.6. Grain-averaged $\overline{\varepsilon}_{22}$ map at 5% average uni-axial strain 57

Figure 5.7. Grain-averaged $\overline{\varepsilon}_{11}$ map at 5% average uni-axial strain 57

Figure 5.8. Grain-averaged $\overline{\varepsilon}_{12}$ map at 5% average uni-axial strain 57

Figure 5.9. Strain distribution evolution (a-c) $\overline{\varepsilon}_{22}$, (d-f) $\overline{\varepsilon}_{11}$, (g-i) $\overline{\varepsilon}_{12}$ 59

Figure 5.10. Evolution of plastic strain vs directional stiffness (a-c) E_{hkl} vs $\overline{\varepsilon}_{22}$, (d-f) E_{hkl} vs $\overline{\varepsilon}_{11}$, (g-i) E_{hkl} vs $\overline{\varepsilon}_{12}$, (j-l) E_{hkl} vs $\overline{\varepsilon}_{maxsh}$ 61

Figure 5.11. Evolution of plastic strain vs absolute maximum Schmid factor (a-c) absolute maximum SF vs $\overline{\varepsilon}_{22}$, (d-f) absolute maximum SF vs $\overline{\varepsilon}_{11}$, (g-i) absolute maximum SF vs $\overline{\varepsilon}_{12}$ 62

Figure 5.12. Evolution of plastic strain vs Area (a-c) Area vs $\overline{\varepsilon}_{22}$, (d-f) Area vs $\overline{\varepsilon}_{11}$, (g-i) Area vs $\overline{\varepsilon}_{12}$ 64

Figure 5.13. Strain difference (core strain - boundary strain) distribution evolution (a-c) $\Delta\overline{\varepsilon}_{22}$, (d-f) $\Delta\overline{\varepsilon}_{11}$, (g-i) $\Delta\overline{\varepsilon}_{12}$, (j-l) $\Delta\overline{\varepsilon}_{maxsh}$, (m-o) $\Delta\overline{\omega}_{12}$ 66

Figure 5.14. Average difference in rotation (a-c), $\Delta\overline{\omega}_{12}$ of the boundary and core of the grains vs boundary area / total area. (Note that larger grains have smaller boundary area/total area ratios after a single layer strip-off.) 67

Figure 5.15. Grain-I (a) Residual intensity map. The red line shows the trace of the slip plane of the slip system with absolute maximum SF (Table 5.4) while orange shows the second, (b-c) ε_{22} at 5% uniaxial deformation, (d) DIC reference image, (e-f) ε_{11} map at 5% uniaxial deformation, (g-h) ε_{12} map at 5% uniaxial deformation. 68

Figure 5.16. Grain-II (a) Residual intensity map. The red line shows the trace of the slip plane of the slip system with absolute maximum SF (Table 5.4) while orange shows the second and white lines, third and fourth ones (b) DIC reference image, (c) ε_{22} map over the grain domain at 5% uniaxial deformation. 70

Figure A.1. Representative description of the columnar grain spectral analysis (a) grain map that is directly constructed from EBSD, (b) type-II (grain-averaged) stress, $\overline{\sigma}_{22}$ and (c) type-III stress, σ_{22} results at point T (where stress, σ_{22} in maps are aligned with loading (vertical) direction) 85

Figure A.2. DAMASK simulation, Type-III stress, σ_{22} results for selected region at point T. 85

Figure A.3. Type-II (grain-averaged) stress, $\overline{\sigma}_{22}$ post-processed from Figure A.2. 86

LIST OF TABLES

Table 3.1. Anisotropy ratio and stacking fault energies of materials. 18

Table 3.2. Elastic constants of pure nickel. 18

Table 3.3. Pure nickel elastic constants in stiffness and compliance [4] (first row); anisotropy ratio (AR), extremal values of isostress stiffness and compliance (second row); utilized DAMASK [34] pheno-power law constants for spectral analysis (third row). 34

Table 4.1. Information and results table for selected grains A, B, C, D. Italicized results in parentheses refer to the spectral model. . . . . .

Table 5.1. Slip systems of Grain-I in the domain (Ordered with respect to absolute maximum SF). 69

Table 5.2. Slip systems of Grain-II in the domain (Ordered with respect to absolute maximum SF). 71

LIST OF SYMBOLS

C_{ijkl}	Components of stiffness tensor
E_{hkl}	Young's modulus of a cubic single crystal along direction ⟨hkl⟩
H	Shannon entropy
h_0	Initial hardening ratio
$h(x, y)$	Digital differantiator coefficient
m	Schmid Factor
M	Kernel radius
n	Stress exponent
n_j	Unit vector slip plane normal
p_k	Gray level frequency
S_{ijkl}	Components of compliance tensor
$\tilde{S}_{\alpha\beta}$	Strain slopes
s_i	Unit vector of slip direction
u_i	Displacement vector
$\delta\tilde{S}_{\alpha\beta}$	Standard deviation of strain slopes
$\dot{\gamma}_0$	Reference strain rate
ε_{ij}	Components of infinitesimal strain tensor
$\overline{\varepsilon}_{ij}$	Grain-averaged strain
$\langle\overline{\varepsilon}_{ij}\rangle$	Field-averaged strain
ξ_0	Initial value of plastic flow resistance
ξ_∞	Final value of plastic flow resistance
μ_{ij}	Components of Schmid tensor
σ_{ij}	Components of Cauchy stress tensor
$\overline{\sigma}^T_{\alpha\beta}$	Grain-averaged stress
τ_{ij}	Component of shear stress tensor

LIST OF ACRONYMS/ABBREVIATIONS

2D	Two Dimensional
3D	Three Dimensional
AFM	Atomic Force Microscopy
AR	Anisotropy Ratio
BCC	Base Centered Cubic
CCS	Cyrstal Coordinate System
CI	Confidence Index
CM	Center of Mass
CP	Crystal Plasticity
CPFEM	Crystal Plasticity Finite Element Method
CRSS	Critical Resolved Shear Stress
D	Discrepancy
DAMASK	Düsseldorf Advanced Material Simulation Kit
DIC	Digital Image Correlation
DOF	Depth of Focus
EBSD	Electron Back Scattering Diffraction
FCC	Face Centered Cubic
FE	Finite Element
FFT	Fast Fourier Transform
G-N	Gauss-Newton
GM	Grain Mask
HCP	Hexagonal Closed-Pack
HEM	Homogeneous Equivalent Medium
IC	Inverse Composition
ODF	Orientation Distribution Function
OM	Optical Microscopy
PRISMS-CP	Predictive Integrated Structural Materials Science-Crystal Plasticity

ROI	Region of Interest
RP	Reference Point
RSS	Resolved Shear Stress
SCS	Sample Coordinate System
SEM	Scanning Electron Microscopy
SF	Schmid Factor
SFE	Stacking fault energy
WD	Working Distance
WEDM	Wire Electrical Discharge Machining

1. INTRODUCTION

1.1. Motivation

Digital image correlation (DIC) has become the standard technique for measuring strain fields in industry and academia. The method has no innate length-scale and its microscopy applications (micro-DIC) have allowed novel and comprehensive measurements of material deformation with high spatial resolution and statistical significance. These findings have been particularly significant for the mechanics of polycrystalline aggregates (polycrystals), which are overwhelmingly the most common class of materials in engineering. The complex strain patterning that is inherent to a polycrystal can now be detailed by micro-DIC, offering validation for next-generation models that seek high fidelity at or below the crystallite scale.

However, a formal framework that recognizes individual crystallite domains in the strain maps is typically lacking. The main technical motivation in this thesis seeks answers to basic questions of polycrystal mechanics; "How load/strain is shared among grains in a regular polycrystalline aggregates?". Of course, strain has a dual nature; elastic and plastic. Both will be investigated in this study. Therefore, providing a material field and strain response that belongs only to a particular grain has become the main challenge.

In other words, the main technical challenge is to accurately single out the strain fields of individual grains with the adoption of complementary electron back scatter diffraction (EBSD) for each individual grain over millimeter-sized fields. EBSD will be used to determine the crystallite orientation, the major physical quantity that governs the elastic constants and slip/twin Schmid factors of a particular crystallite. With these aspects, this study will attempt a statistical quantification of the strain data over the grains, searching for trends over crystallite orientation, size, and neighborhood for both elastic and plastic deformation regions.

In the scope of micro-DIC over a polycrystal where each grain is sampled with high intragranular resolution, one can raise an important question. If grain-averaged strains are calculated, is the average sufficiently improved in accuracy to measure the average elastic strain components of a particular grain during elastic unloading? If, further, stress components can be postulated at a load point from such measurements (i.e., by functionally employing a partial unload from the particular point), a sharper premise arises: If one makes high-resolution type-III measurements of (total) strain with micro-DIC, can one estimate type-II (grain-averaged) stresses over the polycrystalline aggregate, imitating the role of the complementary diffraction methods?. Here, the idea of grain-resolved stress estimates using micro-DIC fields (over functionally employed unloads) will be explored along with methodologies to check the viability and sanity of the results.

Additionally, it is known that the deformation of the crystallite in the polycrystalline aggregate is not necessarily similar to that of single crystals because of the complex deformation behavior of polycrystals (unknown loading condition per crystallite). However, one can ask, "Are these average (type-II) plastic strains of particular crystallites somehow linked with area of crystallite and/or Schmid's factors of crystallite and/or elastic constants of the crystallite during the plastic deformation of the aggregate?". The answer to this question requires statistical significance and should be provided in a formal framework.

Furthermore, reciprocal space techniques (SEM, TEM, etc.) already provide native high-resolution over the crystallite domain that can present distinguishable slip behavior (during the deformation of the polycrystalline aggregate) over the crystallite domain when combined with DIC. However, a real space technique of micro-DIC generally does not provide enough resolution to display the slip bands over crystallite domains. A current method (residual intensity) that enables tracking and visualization of the twin bands by integrating optical microscopy and image processing tools might provide sufficient type-III measurements to detect and identify (when combined with EBSD) activated slip system of crystallite in the aggregate.

1.2. Objectives and Scope

This thesis will be built on a unique DIC setup in the Mechanics of Advanced Materials Laboratory at Bogazici University. This is a novel in-situ DIC implementation with area-scanning optical microscopy that achieves elevated intragranular resolution over millimeter-sized fields by employing high resolution [high numerical aperture (NA)] objectives, only made possible by the integration of automated corrective measures into the custom setup (e.g., high magnification, auto-focusing, auto-locating).

The distinguishing feature of the current effort, however, is to form and incorporate a grain mask that will allow singling out strain fields of individual grains and their subzones. As critically, grain orientations are also predetermined over the identical fields by electron back scatter diffraction seek orientation dependencies of both elastic and plastic deformation.

Using this framework, the scientific objectives of the thesis are twofold. The first goal is more methodical and seeks the possible measurement of *elastic* strains at the grain-scale. However, individual-subset accuracy of the DIC method is very limited (the error range is at the 10^{-3} scale). While measuring elastic strain, it is required to have measures to increase accuracy, or namely reduce the effects of the errors (having as many subsets (data points) as possible over a single grain, averaging strain to reduce uncertainty, morphological approaches and DIC reference point alteration) (see Chapter 3).

The second task pertains to the plastic deformation of the polycrystalline aggregate resolved at the intragranular scale. The statistical objective is to seek correlations between grain orientation parameters (e.g., Schmid factor, directional stiffness) and grain deformation measures (e.g., average strain). Local objectives include the identification of slip traces by using a novel residual intensity technique.

During the experimental effort, an extremely comprehensive EBSD combined DIC experiment is performed in terms of statistical significance per intragranular domain (500 data points per grain on average). The study will consider a pure FCC metal instead of BCC and HCP metals that show more varied and complex deformation to focus on fundamental aspects of polycrystal deformation. (A simple material (pure FCC nickel) is selected but with a high anisotropy ratio (= 2.5) to promote the intergranular differences that are to be observed and comparatively evaluated.)

2. BACKGROUND AND LITERATURE REVIEW

Typical isothermal deformation in polycrystalline aggregates is composed of elastic and plastic deformation. Metal elasticity shows limited strains and is well explained by the linear (generalized) Hooke's law. In the case of plastic deformation, crystalline aggregates show more complex and heterogeneous behavior. Although the primary plastic strain accommodation is typically caused by dislocation slip [1], there are some other deformation mechanisms such as twinning, phase transformation, grain boundary sliding, and diffusional flow [2, 3].

2.1. Generalized Hooke's law

For the relation between elastic strains and Cauchy stress components, the generalized Hooke's Law can be described as Equation 2.1 where the stiffness matrix is a 4th rank tensor (C_{ijkl}) with 81 elastic constants. For crystals with cubic symmetry, these 81 elastic constants are reduced to 3 independent elastic constants C_{11}, C_{12}, and, C_{44} in Voigt notation. These constants are well known, particularly for pure metals [4, 5].

The generalized Hooke law in full-tensor notation is given as

$$\sigma_{ij} = C_{ijkl}\varepsilon_{kl} \ . \tag{2.1}$$

Its expression for cubic materials in Voigt notation for the components expressed in native crystal coordinates (1-2-3 axes aligned with $\langle 100 \rangle$ axes) is

$$\begin{bmatrix} \sigma_{11} \\ \sigma_{22} \\ \sigma_{33} \\ \sigma_{23} \\ \sigma_{13} \\ \sigma_{12} \end{bmatrix} = \begin{bmatrix} C_{11} & C_{12} & C_{12} & 0 & 0 & 0 \\ C_{12} & C_{11} & C_{12} & 0 & 0 & 0 \\ C_{12} & C_{12} & C_{11} & 0 & 0 & 0 \\ 0 & 0 & 0 & C_{44} & 0 & 0 \\ 0 & 0 & 0 & 0 & C_{44} & 0 \\ 0 & 0 & 0 & 0 & 0 & C_{44} \end{bmatrix} \begin{bmatrix} \varepsilon_{11} \\ \varepsilon_{22} \\ \varepsilon_{33} \\ 2\varepsilon_{23} \\ 2\varepsilon_{13} \\ 2\varepsilon_{12} \end{bmatrix} \tag{2.2}$$

Inversely, it can be described in terms of compliances as

$$\varepsilon_{IJ} = s_{IJKL}\sigma_{KL} \tag{2.3}$$

and can be written in Voigt notation as

$$\begin{bmatrix} \varepsilon_{11} \\ \varepsilon_{22} \\ \varepsilon_{33} \\ 2\varepsilon_{23} \\ 2\varepsilon_{13} \\ 2\varepsilon_{12} \end{bmatrix} = \begin{bmatrix} s_{11} & s_{12} & s_{12} & 0 & 0 & 0 \\ s_{12} & s_{11} & s_{12} & 0 & 0 & 0 \\ s_{12} & s_{12} & s_{11} & 0 & 0 & 0 \\ 0 & 0 & 0 & s_{44} & 0 & 0 \\ 0 & 0 & 0 & 0 & s_{44} & 0 \\ 0 & 0 & 0 & 0 & 0 & s_{44} \end{bmatrix} \begin{bmatrix} \sigma_{11} \\ \sigma_{22} \\ \sigma_{33} \\ \sigma_{23} \\ \sigma_{13} \\ \sigma_{12} \end{bmatrix}. \tag{2.4}$$

One of the goals of this study is to identify elastic strains that vary from grain to grain in a polycrystalline aggregate. This heterogeneity is correlated with the elastic anisotropy of the crystals. For cubic metals, the relevant quantity is the anisotropy ratio (AR) or Zener ratio [6] that is related to the elastics constants as,

$$AR = \frac{2C_{44}}{C_{11} - C_{12}} \quad or \quad AR = \frac{2(s_{11} - s_{12})}{s_{44}}. \tag{2.5}$$

Another important measure directly related to crystal anisotropy is the stiffness E_{hkl} of a single crystal when it is subjected to a tensile test along the crystal direction hkl,

$$E_{hkl}^{-1} = s_{11} + \frac{(2s_{12} - 2s_{11} + s_{44})(h^2k^2 + k^2l^2 + h^2l^2)}{(h^2 + k^2 + l^2)^2}, \tag{2.6}$$

where E_{111} and E_{100} are the extremal values of this effective stiffness, with their ratio E_{111}/E_{100} typically not too far from AR.

In polycrystals, grains possess different orientations with respect to crystallographic texture. Thus, the crystallographic loading direction hkl of each grain aligned differently (and depends on its orientation). Since stresses usually are imposed in sample coordinates, it is practical to pose Hooke's law is in the sample coordinates for an arbitrary grain. The matrix form of the orientation is used as a change of basis operator to transform native crystal-coordinate components in Equation 2.4 to sample-coordinate components as

$$C_{ijkl} = g_{iI}\, g_{jJ}\, g_{kK}\, g_{lL}\, c_{IJKL}, \tag{2.7}$$

where C_{ijkl} and c_{IJKL} are the components of the stiffness tensor in the sample and crystal coordinates, respectively, and this change of basis is applicable to the compliance tensor.

2.2. Deformation of FCC Crystals and Polycrystals

The Burgers vector of perfect dislocations in FCC is defined through the direction of $\mathbf{b} = \frac{1}{2}\langle 1\ 1\ 0\rangle$. These are the close-packed atomic directions and since the dislocation energy is proportional to $\mathbf{b}^2$, other possible dislocations (that do not change stacking sequence), e.g., $\langle 1\ 0\ 0\ \rangle$are energetically less favorable [1].

The actual slip in FCCs does not involve the motion of a perfect dislocation. Instead, the dislocation dissociates into partials; the two partials attain a characteristic separation and follow each other with a stacking fault between them. These partials are called Shockley partial dislocations and are defined on the right side of $\mathbf{b} = \frac{1}{2}\langle 1\ 1\ 0\rangle = \frac{1}{6}\langle \bar{2}\ 1\ 1\rangle + \frac{1}{6}\langle 1\ 2\ \bar{1}\ \rangle$. The partial dislocations, ($\mathbf{b}_2$ and $\mathbf{b}_3$), and their vectorial relationship with the perfect dislocation $\mathbf{b}_1$ are illustrated in Figure 2.1. When the two partials pass over a region, the shift associated with the perfect dislocation is realized.

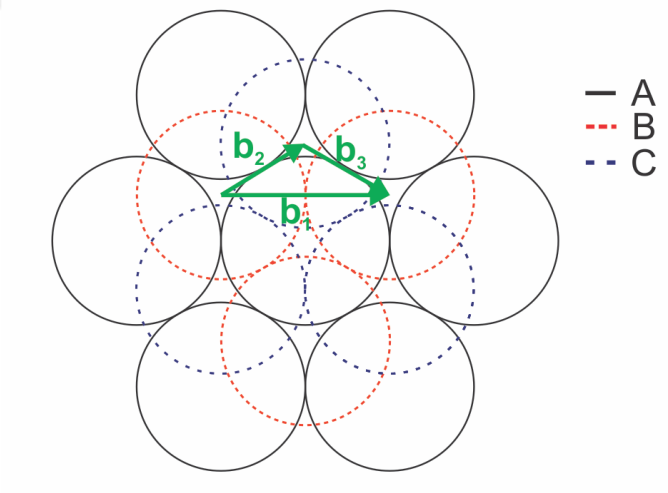

Figure 2.1. Perfect and partial dislocation

The preferred slip systems of FCCs are well-defined as $\{111\}\langle 110\rangle$ (plane and direction) family. Although there are some other non-octahedral slip systems defined for FCC structures [7], these slip systems may only become activated in extreme conditions such as high temperatures and extreme strain levels. These slip systems are ignored in this study since the tensile experiment is conducted at room temperature

and the deformations are relatively small. Therefore, the deformation is dominated by $\{111\}\langle 110\rangle$ slip system family that has total of 12 possible slip systems. This study will focus on activation of these slip systems.

Activation of slip systems, or alternatively yielding of single crystal FCC structures, obeys well-established criteria (Schmid (Equation 2.11 and Equation 2.9)) and Taylor factors [8, 9]). Depending on the applied stress and the crystallographic orientation, each slip system undergoes a distinct resolved shear stress (τ_{RSS}, Equation 2.10 and Equation 2.8). When the resolved shear stress reaches a critical value (τ_{CRSS}) on a single slip system, the plastic deformation starts with slip. Theoretically, the slip system with the highest absolute Schmid Factor (SF), (m), activates before other slip systems for single crystals. The following equations will be used to calculate SFs,

$$\tau^{\alpha}{}_{RSS} = \sigma^{\alpha}{}_{ij} : \mu^{\alpha}{}_{ij}, \tag{2.8}$$

$$\mu^{\alpha}{}_{ij} = s^{\alpha}{}_{i} \otimes n^{\alpha}{}_{j} \tag{2.9}$$

$$\tau^{\alpha}{}_{RSS} = \sigma \cos\phi^{\alpha} \cos\lambda^{\alpha}, \tag{2.10}$$

$$m = \cos\phi^{\alpha} \cos\lambda^{\alpha} \; and \tag{2.11}$$

$$m_{max} = max(|m^{\alpha}|) \tag{2.12}$$

where α is the corresponding slip system (out of total 12 slip system FCC structures), $\mathbf{m}$ is SF, $\boldsymbol{\mu_{ij}}$ is the Schmid tensor, $\mathbf{s_i}$ is the unit vector of slip direction, and, $\mathbf{n_j}$ is the unit vector of slip plane normal. If the stress state and orientation of crystallite are known, Schmid tensor for each slip system can be calculated by Equation 2.9 and resolved shear stresses can be found for each slip system (with the sizeable assumption that the uniaxial stress state applies for each crystallite).

At the crystallite level, due to the complex neighboring and boundary conditions of the grains, the stress state of the individual grains does not necessarily align with the stress state of the bulk. This behavior introduces additional complexity in the plastic deformation of polycrystalline aggregates. Most of the recent deformation models (see Section 2.3) try to tackle this complexity by considering high-fidelity deformation models. However, recent experimental studies show that slips that accumulate in grain

boundaries can initiate and/or transfer slips in neighboring grains [10, 11]. Although the mechanism of slip transfer is not well defined, there are some studies [10–12] investigating the slip transfer mechanism from one grain to another.

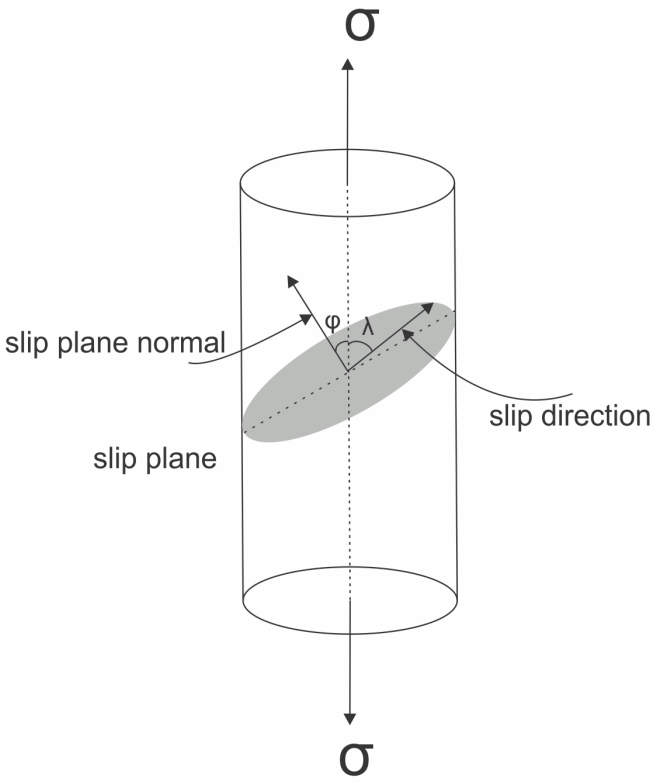

Figure 2.2. Schmid factor

Another type of deformation at the polycrystalline level is grain boundary sliding that generally occurs in very fine grain-sized polycrystals (especially in nano-sized polycrystalline FCC structures). Since dislocation mechanisms become harder to interact within the intragrain domain due to the increase in dislocation density, the polycrystalline aggregate accommodates macro deformation through mechanisms such as sliding of the grain boundary or grain boundary separation, which may yield micro crack formation and crack propagation [13, 14].

2.3. Polycrystal Models

In the literature, polycrystalline deformation models are divided into two main categories: mean-field(*aka* 1-site) and full-field (*aka* n-site) models.

2.3.1. Mean-field Models

The simplest interactions that can be assumed for analytical predictions over polycrystalline aggregates are the isostress and isostrain assumptions. The isostress model [15, 16] appeared first, assuming the same stress state for all crystallites in the aggregate. This simplistic interaction violates compatibility (while trivially satisfying local equilibrium). Later, the isostrain model [9], which assumes the same strain levels for all grains, was proposed. However, this model violates equilibrium (but trivially satisfies compatibility). Both approaches are unrealistic and are rather employed as limiting cases of bulk stiffness (isostrain stiffest, isostress most compliant). More refined mean-field models, called self-consistent models [17, 18] were developed using Eshelby's elliptical inclusion theorem [19]. These models assume that each crystallite interacts with an average medium called homogeneous equivalent medium (HEM). In this scheme, each crystallite factors into the tangent stiffness of the HEM, and an iteration is carried out until HEM properties converge. The self-consistent approach is employed with different constitutive models, e.g., primarily note the elasto-plastic or visco-plastic approaches [20–22]. However, these are still mean-field models that can, by definition, only target the bulk (aggregate average) behavior, and any realistic simulation of intergranular interactions in a crystallite neighborhood is out of the question.

2.3.2. Full-field Models

In the full-field approach, instead of a single site, multiple sites are involved in modelling the polycrystalline aggregates, which allows grains to interact with each other and gives results for both intragranular and intergranular domains. The first ap-

plication [23–27] of this approach was using finite elements (FE) methods that provide high flexibility while modelling complex geometries and complex boundary conditions; however, due to the large number of degrees of freedom and computational limitations, the size of the analyzed microstructures is limited. However, there are recent, robust and flexible FE tools, e.g. PRISMS-CPFE (FE solver) [28] for multiple models (rate-dependent, thermomechanical and cyclic).

As an alternative to FE methods, FFT-based spectral methods [29,30] have been developed. Although these methods offer computational efficiency, boundary conditions should always be periodic that limits the complexity of boundary conditions and geometries but does not limit the size of the domain. Algorithms used in spectral methods are capable of simulating heterogeneous media such as polycrystals[1] , composites, multi-phase materials etc. [31–33].

In this study, a spectral CP tool, DAMASK [34] that utilizes a pheno-power law model, is implemented to simulate deformation over the experiment domain. See details in Section 3.8

2.4. Experimental Data on Polycrystal Deformation

Polycrystalline metallic aggregates have traditionally been regarded as isotropic and homogeneous materials on a macroscopic scale. However, on the microscopic scale, recent studies [35–39] have revealed that polycrystalline aggregates undergo heterogeneous deformation with localized strains. Although most of these studies focus on plastic deformation [40–42], only some consider elastic deformations [43–46]. Elastic or lattice strain measurements are generally in the field of diffraction methods [21], [47], but diffraction applications do not provide any intragrain or subgrain resolution. Furthermore, the overwhelming majority of subgrain-scale investigations of metallic poly-

[1]Although, anisotropic homogeneous polycrystalline structures are deformed uniformly in macro scales, they should be considered as complex composites in micro-scale due to local heterogeneity of deformation originating from crystallographic orientation variation.

crystals cover relatively small portions of the bulk material, and they are conducted using scanning electron microscopes (SEMs).

Recent full-field experiments provide insights for refining and updating CP models. In the field of CP, recent robust models (mostly mean-field models) are embedded in CP simulation tools [27, 28] and these comprehensive simulation tools allow users to simulate different types of deformation models (dislocation density, cyclic loading model, or thermo-mechanical models) in a variety of length scales [48]. However, these deformation models and tools require experimental results [37], [49–52] at different length scales for validation. Fortunately, DIC methods provide these results over large material fields with combined crystal orientation information.

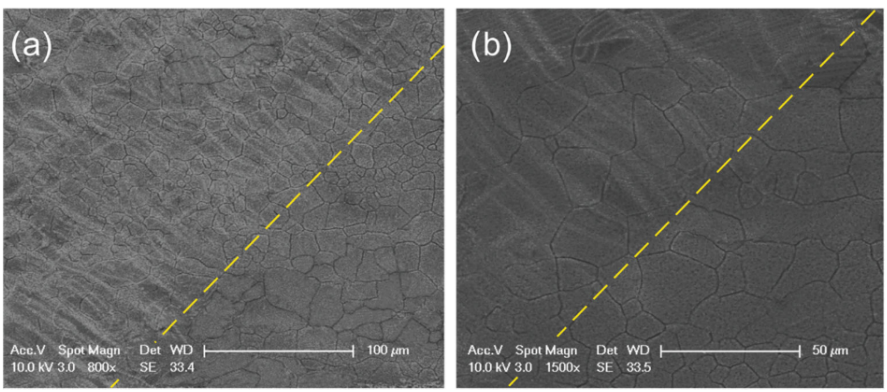

Figure 2.3. SEM micrographs with twin plateau (a) 800x, and (b) 1500x magnification, recorded at the boundary of a tensile-twin-driven band (the separation of band indicated with a dashed line) [41]

In the case of complex and abrupt deformations, there is a wide variety of experimental data available in the literature. Although some of them consider the heterogeneity of the deformation on a meso-scale [35], [41, 42] and show twin traces over grains (Figure 2.3), some of the works provide comprehensive insights into the localization of the strain over morphological structures such as twin bands and grain boundaries and then seek the correlation of deformation with orientation considering Schmid (Figure 2.4) and Taylor factors [40], [53, 54].

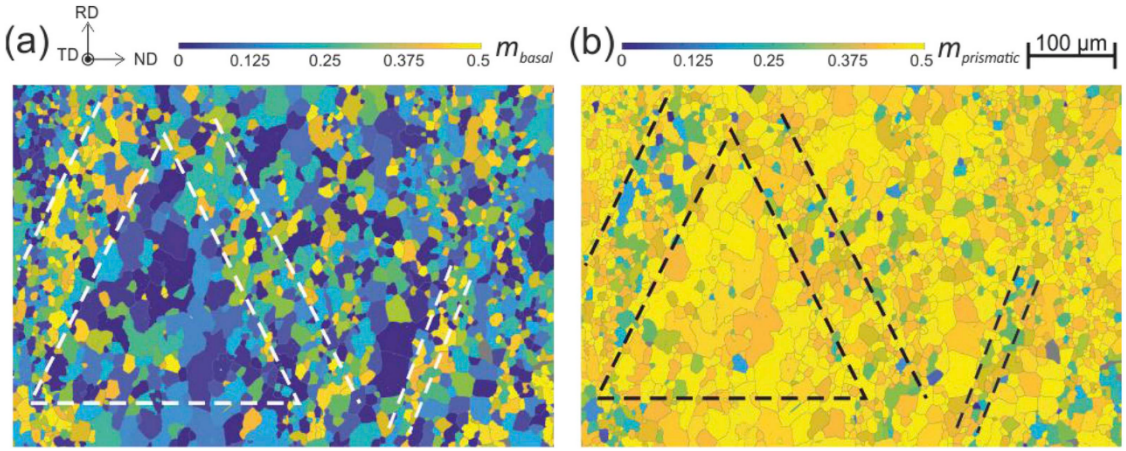

Figure 2.4. Schmid factor maps of the plate at undeformed state for (a) basal slip, (b) prismatic slip (dash line shows corresponding deformation bands) [54].

This study employs optical microscopy DIC, which, despite having limited intragrain resolution compared to SEM variants, offers practical advantages such as not requiring a vacuum and being flexible when combined with other measurement techniques. It provides critical insights [50] into the interaction length-scale of polycrystalline aggregates while covering larger domains through area scanning.

The accuracy and field coverage of optical microscopy DIC experiments have shown improvements with the implementation of automated solutions. For instance, automated working distance adjustment [50], along with the utilization of high magnification lenses featuring a high numerical aperture and combined auto-locate enabled area scanning [54], contribute to the enhancement of results. Consequently, statistical investigation of grain-resolved strain fields and average elastic strains over grains in polycrystalline materials emerges as a significant, yet relatively unexplored, topic in the current literature.

When these grain-resolved domains are integrated with the orientation of each grain by additional EBSD, the grain-resolved deformations can be correlated with the directional stiffness in the elastic zone and slip in the plastic zone for each crystallite in the region. One of the first experiments performed by Raabe et al. [55], on grain-scale deformation in polycrystalline aggregates seek correlation of surface roughness,

grain orientation and Von Misses strains. However, this approach does not offer high intragrain resolutions. Some other studies consider oligocrystal structures, which are produced in laboratory environments. Even though it is hard to incorporate these materials in engineering applications, they still provide a multi-crystal aggregate. A promising study by Zhao et al. [37] with an aluminum oligocrystal structure shows localization of strains over grain boundaries, strain heterogeneity, and slip formation even though there are only a few grains (Figure 2.5). Additionally, this work seeks correlation between finite element results. However, this work does not provide any statistical significance due to the small number of grains.

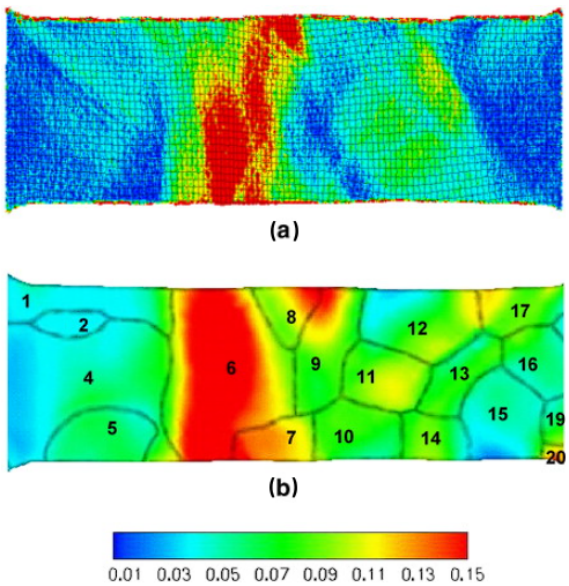

Figure 2.5. Comparison of strain maps between: (a) experiment and (b) simulation [37].

Another, but a larger domain experiment in Zirconium by Padilla et al. [56] aims to establish a statistical relationship between local texture and local heterogeneity. Although this study has an intragranular resolution, the study only focuses on localization of strain over domain and search for correlation between Schmid factors (for prismatic slip systems) and local strains (Figure 2.6) with respect to different load points; however, per grain correlations are not cited.

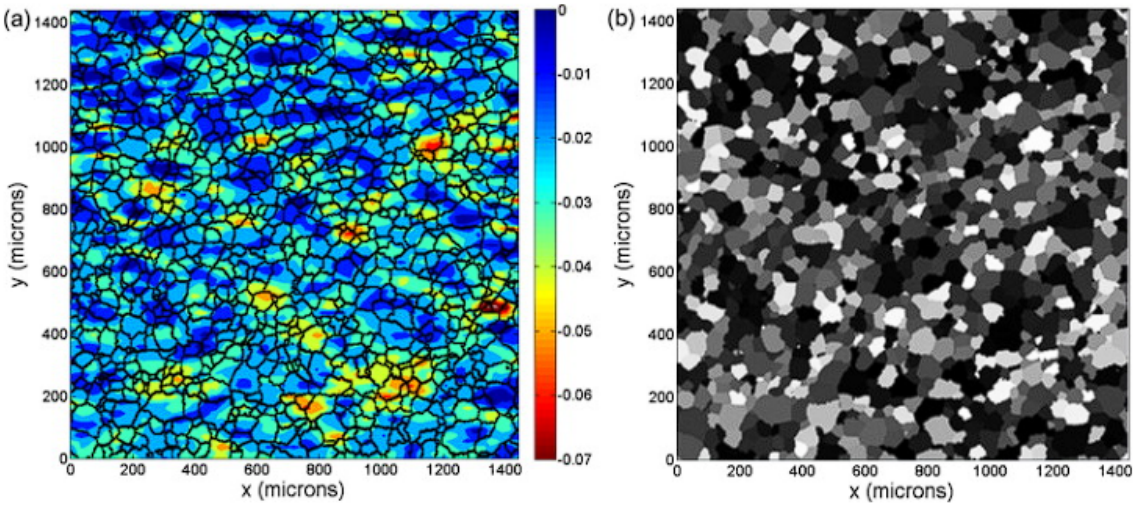

Figure 2.6. Comparison of (a) DIC axial strain, (b) prismatic Schmid factor map. The loading is in the vertical direction [56].

In case of FCC pure nickel, there are some ex-situ experiments that utilize columnar grains [57, 58]. Despite having over 100 grains within the experimental region, these studies did not incorporate any quantitative deformation measurement method. Instead, by applying some cold rolling, they are just using change of area to calculate strains and compare them with theoretical area changes as well as alterations in grain orientation. However, these grains are enormously large and the statistical significance of these works is to investigate orientation evolution rather than deformation. Another in-situ EBSD embedded study by Wu et al. [59] for FCC pure nickel considers the large deformation over a region with multiple grains and investigates both orientation changes and plastic deformation (see Section 2.7). They commented that grains that have a high Schmid factor are more compatible with deformation by intragranular slip and misorientation during deformation. Grains with low Schmid factor accommodate bulk deformation through rotation. However, this study examines only a few grains in the plastic deformation domain.

Another recent work [13] on FCC pure nickel investigates large plastic deformation with both experimental and simulation methods in order to observe grain orientation evolution, grain boundary interfaces, and slip transmission between grains using Luster-Morris geometric compatibility [12]. The study focuses on dislocation pile-ups

and hindrance at Σ 3 boundaries and provides information on rotation of grains to accommodate bulk deformation.

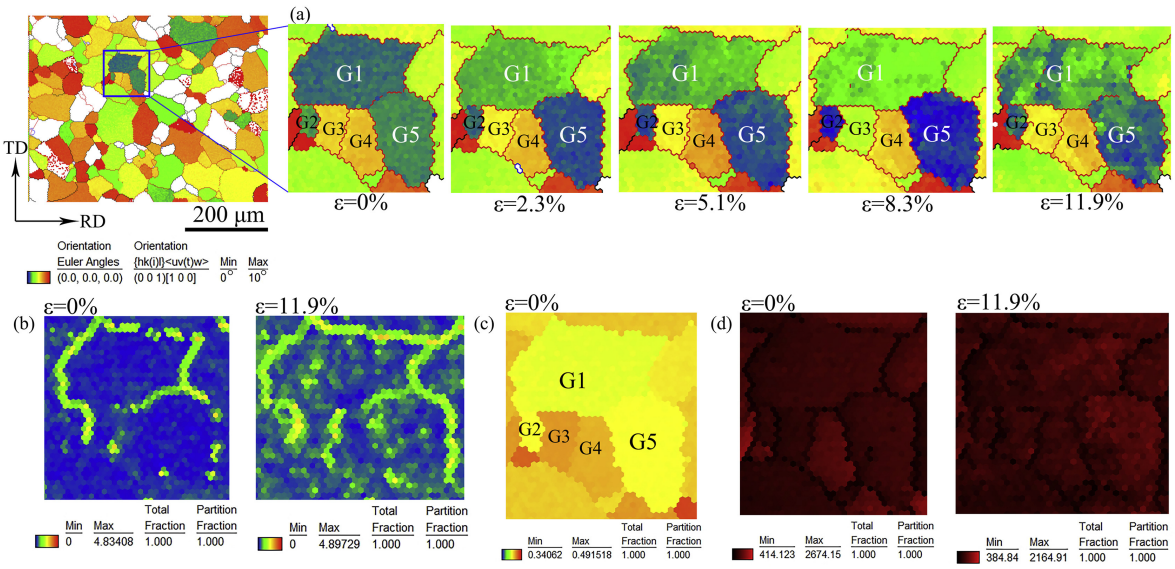

Figure 2.7. (a) Orientation maps (b) KAM maps of the initial sample and deformed sample, respectively (c) SF maps (d) IQ maps of the sample with strain at 0% and 11.9%, respectively [59].

In the case of elastic deformation, except for diffraction methods, there are limited studies with DIC, however, a recent study by Latypov et al. [45], in-situ DIC combined with CP simulations, considers Young's modulus and elastic strain densities near morphological structures to relate initiation of cracks (Figure 2.8). Another recent work [43] also follows a similar approach to relate elastic strains and variation of elastic constants among neighboring grains with localization of plastic strain.

Overall, literature on metallic polycrystalline aggregate deformation is expanding in both modelling and experimentation, which is crucial to validate the models. These models and experiments predominantly focus on plastic deformation, and only a limited portion of the studies address elastic deformation because of the relatively lower accuracy of the DIC methods. In the case of single crystals, generalized Hooke's law based models are always in good agreement with deformation. However, when bulk deformation is considered, factors such as the orientation of the crystallite, crystallite

geometry, neighboring crystallites, and their crystallographic orientations introduce additional complexities to the models. This area remains open for further research. One fold of this dissertation will seek answers to grain-resolved elastic deformation statistics in conjunction with the local stress state, while the other fold will seek answers to grain-resolved plasticity, again in a statistical manner.

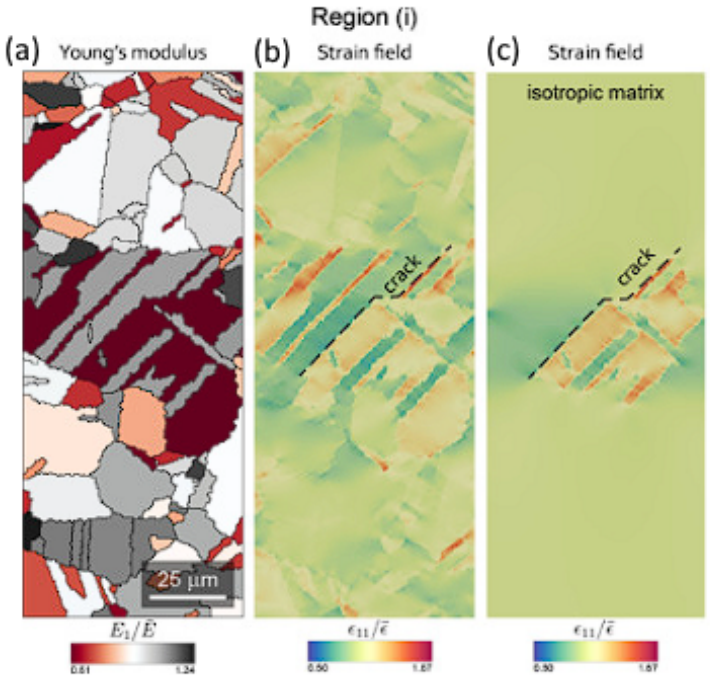

Figure 2.8. (a) Young modulus map (b) DIC Elastic Strain (c) CP-FEM analysis of grain in isotropic matrix [45].

3. MATERIALS AND METHODS

3.1. Material

The candidate materials are mainly chosen among FCC polycrystalline metals because they are less likely to have deformation twin under loading compared to BCC and HCP materials due to their relatively simple deformation slip mechanism. Likewise, lattice structure and stacking fault energy (SFE) are also related to twinning behavior; therefore, materials with high SFE (Table 3.1) materials are less likely to have deformation twining during loading. Since one of the aspects of this study is to measure grain-resolved elastic strain, deformation heterogeneity is important to observe different elastic strains per grain. For this purpose, elastic anisotropy (Zener ratio) (well established measure for directional dependence of elastic deformation of FCC crystals) is considered as another selection criterion for the material in this study.

Table 3.1. Anisotropy ratio and stacking fault energies of materials.

Material	**Anisotropy ratio (AR) [5]**	**Stacking fault energy [mJ/m^2]**
Aluminum	1.19	160-200 [60]
Copper	2.87	70-78 [61]
Nickel	2.5	90 [5]

Table 3.2. Elastic constants of pure nickel.

C_{11}	C_{44}	C_{12}	s_{11}	s_{44}	s_{12}
[GPa]			[TPa^{-1}]		
246.5	124.7	147.3	7.34	8.02	-2.74

An extruded 6.35mm-diameter-nickel-rod with purity of 99.5% was procured from vendor (Alfa-Aesar) under the material code 11454. Chemical analysis also provided by Alfa-Aesar with respect to the material lot number of Q21A030 that shows traces

of other elements in the unit of ppm as follows (C: 200, Cu: 100, Fe: 1100, Mn: 2300, S: 10, Si: 1000)

The rod is heat treated for 4 hours at 750° C, then cooled to room temperature inside the furnace to allow texture relief and grain growth. The average grain size is increased up to ∼30 μm, which is favorable for increasing the number of DIC measurement subsets over a single crystallite (which are directly proportional to the grain area). On the other hand, having enormously larger grain sizes compromises the purpose of the study by reducing the number of grains in the region of interest (ROI) and compromises the macro-homogeneity of the deformation.

3.2. Tensile Specimen

The dog-bone shaped tensile specimen Fig 3.1, which has a cross-section of 3 mm x 3.2 mm with a 6 mm gage length, is manufactured with wire electric discharge machining to minimize the residual stress over specimen surface. Then specimen hot mounted (at 175°C with relatively low pressure) to bakelite for metallographic preparation.

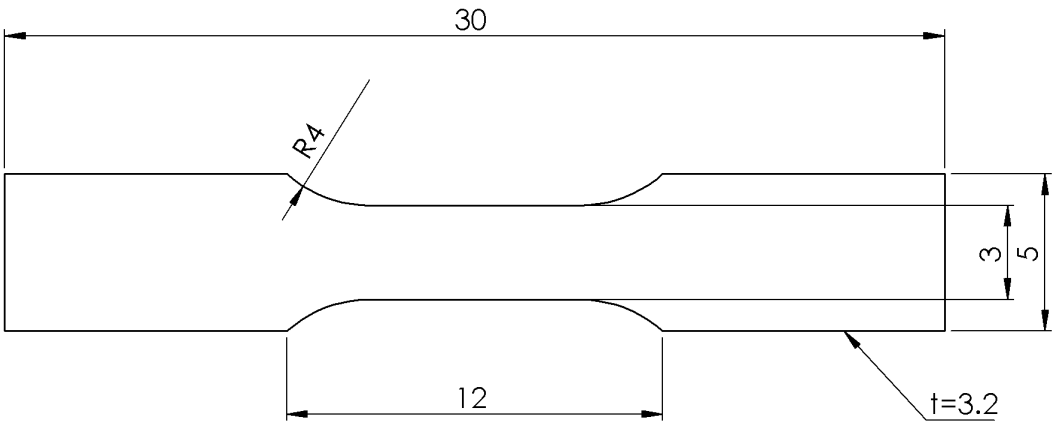

Figure 3.1. Tensile specimen after manufactured with WEDM.

3.3. Metallography

During metallographic preparation of the specimen's surface, rough grinding (P800-1 min.) and gradual fine grinding (P1200-2 mins., P2000-5 mins., P4000-12 mins.) applied with a load of 50N by a cross-rotated automated grinding/polishing device (QATM Saphire 530). Then, the surface of the specimen is polished for over 60 minutes with a load of 10N by using 5nm-particle-sized water-based colloidal silica solution to have a perfectly flat surface for electron back-scatter diffraction. After polishing, the specimen's surface is etched with a diluted (10%) solution of Marble's Reagent [62] for a few seconds to reveal grain boundaries, then polished again for a minute to clean up residual chemicals and oxides on the surface of tensile specimen. This subsequent procedure is conducted for three times to concretize the grain boundaries by allowing the etchant to penetrate all grain boundaries equivalently and improve the surface of the sample Figure 3.2 for EBSD by reducing the residual stresses induced by grinding / polishing.

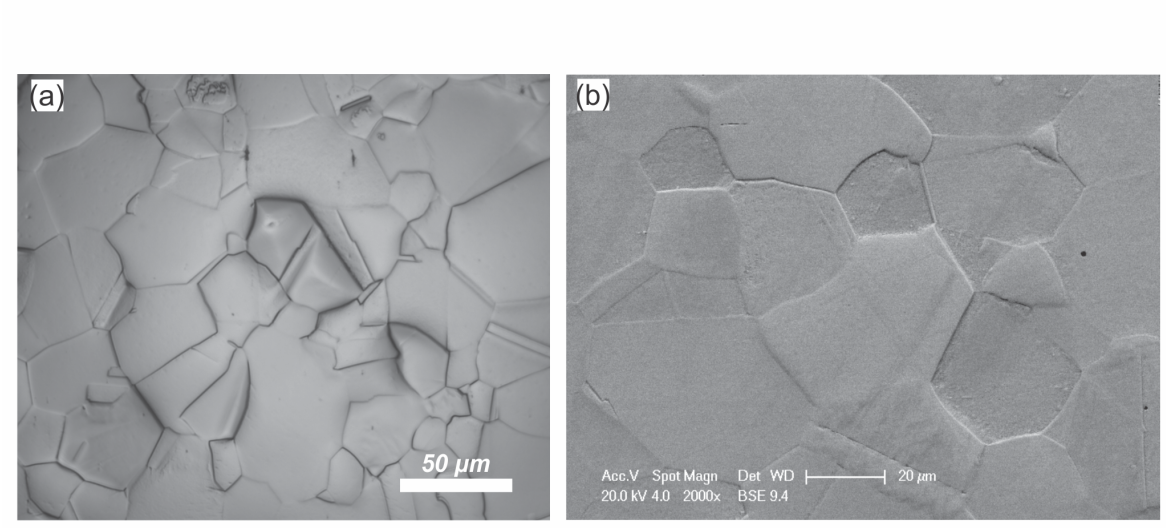

Figure 3.2. Specimen surface after metallography a) Optical microscopy image (40X), b) SEM image (2000X)

3.4. DIC Speckle Pattern Application

The application of speckle patterns is crucial for digital image correlation (DIC) as the size of the speckle pattern directly affects the resolution of DIC, and the uniqueness of subsets depends on the application of the speckle pattern. Traditional speckle pattern application methods for micro-scale optical DIC often employ spraying methods, which have disadvantages such as the formation of bubbles on the specimen surface due to wetting properties and problems related to the spray nozzle.

In this study, speckle patterns were applied using a non-marking tape rather than the traditional direct spraying method. The sticky side of the tape was sprayed with a uniform thin layer of water-diluted (10%) paint, avoiding bubble formation as it can cause surface tension, which alters the density of the paint. The specimen surface was then covered with the tape and a gentle force was applied to form a thin-film layer of suspension between the tape and the specimen surface. Later, the tape was folded back from one of its corners and removed gently by pulling it backward. During this process, the surface tension of the suspension was visible on the parting line between the tape and the specimen surface. It is important to slide the tape down without disturbing the surface tension of the water-based paint suspension during tape removal, unless bubble-like suspension residuals form on the surface.

To evaluate the quality of the speckle pattern, a 4x4 grid of microscopic image scan, Figure 3.3(a) is done after speckle pattern application. Shannon-Entropy based algorithm [63] that gives a measure about content of the image in the manner of distinction (Equation 3.1), is applied to images Figure 3.3(b) to visualize results by formulation of

$$H = -\sum_{k} p_k log_2(p_k), \tag{3.1}$$

where $\mathbf{H}$ is the Shannon entropy and $\mathbf{p_k}$ can be considered as the frequency of gray levels in an image array. The algorithm used in this study mainly is a subset based

algorithm with a very similar to DIC application. Each image is divided into subsets (61x61 pixel^2).

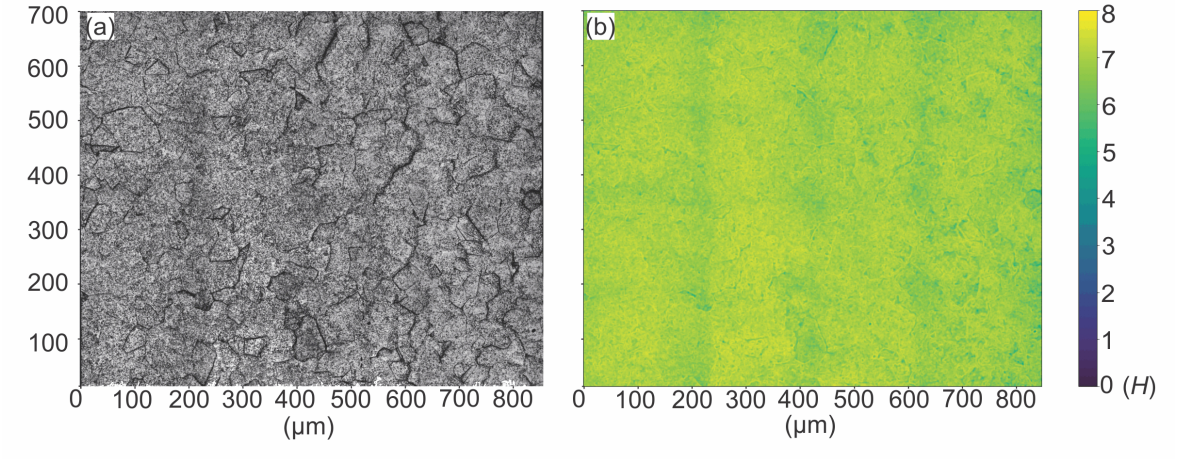

Figure 3.3. (a) Speckle pattern and (b) Shannon entropy results over 4x4 grid of microscopic images.

The results of using non-marking tape, Figure 3.3 lead to better outcomes compared with the traditional direct spraying methods. Specifically, the non-marking tape method resulted in speckle patterns with no paint localization and better pattern homogeneity while providing a repeatable process that can be applied multiple times until the desired pattern is constructed. Furthermore, these advantages were observed while the same paint with an average particle size of 0.4 μm was used in both methods. Overall, the non-marking tape approach is a promising alternative to traditional spraying methods for speckle pattern application in micro-scale optical methods.

3.5. Experimental Setup

In this study, both small strain fields and mild to high strain fields are obtained to investigate the deformation properties of polycrystalline FCC pure nickel mainly in the elastic and also plastic regions. To correlate these deformations with crystallite orientation requires an orientation information of each single crystal over ROI. Coupling strain fields over a known material field requires multiple experimental setups; i) an

in-situ Optical Microscopy DIC setup to obtain strain fields per load and ii) SEM with EBSD detector to gather orientation information prior to tensile test.

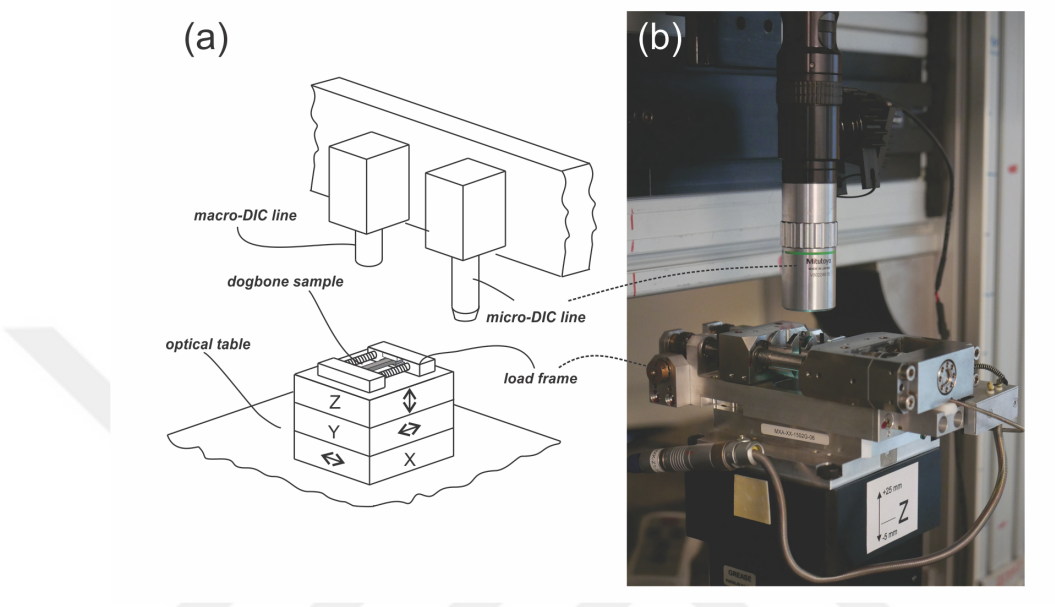

Figure 3.4. (a) Schematic demonstration of DIC lines and 3-axis-stage (b) Photo of load frame and microscopic DIC line.

The main elements of the custom DIC setup shown in Figure 3.4(a-b) are (i) stationary optical lines: macroscopic (FLIR Grasshopper 3 camera, 2.3 MP Sony IMX174 monochrome sensor, Edmund Optics 0.5x telecentric lens) and microscopic (FLIR Grasshopper 3 camera, 5 MP Sony IMX250 monochrome sensor, Navitar Ultra-zoom 6000 tube lens, Mitutoyo M Plan APO 20x objective at 0.1 μm/pixel resolution), (ii) a small form factor tension-compression load frame (10 kN, Kammrath & Weiss), and (iii) an X-Y-Z positioning array (Newport M-ILS series of X-Y, GTS30V for the vertical Z positioner). The entire setup is placed on a vibration isolation table (Newport RS4000). An in-house instrument software is used to orchestrate the automated coordination of cameras and the motion of the stages. During the load application in the experiment, continuous strain monitoring is implemented under the macroscopic line (with live macro-DIC analysis). At selected loads, the sample is sent under the micro-DIC line and micro-DIC area-scans (X-Y) are conducted. These record images of the surface over a predefined grid of overlapping frames as shown in the upper right

corner of Figure 3.4(a-b). The image overlaps allow continuous mergers of both image and data (e.g., strain) fields. In this study, the frame matrix is 13×7, encompassing an overall area of 0.8×1.8 mm^2.

Given the utilized high numerical aperture (NA=0.42) Mitutoyo objective with an extremely limited depth of field (DOF=1.6μm), auto-focusing is vital to avoid de-focusing. Each frame in the automated micro-DIC scan is auto-focused individually. Auto-focusing entails the computerized selection of the image with best focus measure value from an image stack that is recorded with fine increments in the Z-direction. Regarding motion along the Z-direction (either due to out-of-plane deformation of the sample or due to motion imposed by the Z-positioner), a direct concern is the working distance (WD) error. A change in WD would cause a perspective error that would manifest as an artificial biaxial strain field in the DIC results. This strain error goes by δZ/WD; where δZ is the error between the WDs of the reference and the deformed states. In this scheme, the small (1.6μm) DOF is used as an advantage and auto-focusing maintains WD within a factor of the DOF. With the 20 mm WD of this long-WD objective, δZ/WD is dropped below the 10^{-4} order. While this is an order below the typical DIC uncertainty, its prominence as an error source will be elevated by local averaging (that increases accuracy in lieu of spatial resolution).

3.6. Experimental Procedure

3.6.1. EBSD and Orientation Mapping

EBSD analysis of the sample surface is performed at the Metallurgical and Materials Engineering Department of Middle East Technical University. The scanning electron microscope (SEM) of the FEI NOVA Nanosem 430 which is equipped with the EDAX EBSD detector, is employed for the orientation detection of surface grains. To effectively scan the surface, the SEM is set to 20kV and 4.5nm spot size, and the orientation is collected by the EBSD detector with a 3μm step size. Multiple fiducial markers are placed to the surface with a micro-vickers indentation to easily identify the

region of interest over the surface. Two of these markers can be seen on the left and right of the Figure 3.5(a) over a line of approximately 600μm away from the horizontal axis. During the EBSD scan, the grain orientations gathered with a high confidence index (CI[2] =0.68). Due to the large area of the EBSD scan, a relatively high step size is chosen and orientation maps are gathered in three different scans. Orientation maps of scans are then constructed using inverse pole figures (Figure 3.5(b)) which are aligned with loading direction of the tensile specimen. Later, these orientation maps are combined with the grain mask and also used to build geometries for spectral and finite element solvers.

Additionally, texture (Figure 3.5(f)) of the specimen is revealed by the orientation distribution function (ODF) that is generated by EBSD scan. By considering the EBSD data, the orientation distribution of grains can be visualized in terms of pole figures (Figure 3.5(e)) which provides texture information. According to pole figures, the grains over the field show a weak fiber texture (because of the initial heat treatment) for pure nickel, which is used in this study.

3.6.2. Grain Mask Generation

In this study, traditional DIC methods are combined with a grain mask Figure 3.5(a) which enables grain resolved strain output for each grain in the region separately. These masks are generated prior to the application of the speckle pattern to clearly reveal the grain boundaries (Figure 3.5(d)), which are easier to identify before the application of the speckle pattern. The specimen is scanned multiple times (pre-EBSD imaging, EBSD and DIC imaging) with different mountings in different setups (EBSD fixture, tensile grips, etc.) which causes some level of tilt, rotation, and translation for each setup. Multiple spaces and multiple spatial resolutions become the main challenge in generating grain masks. This challenge was overcome by using affine transform techniques.

[2]CI is a parameter that shows the accuracy of orientation measurements. A CI of 0.2 correlates with 95% probability for correct orientation while using at least six Kikuchi bands for orientation identification [64]

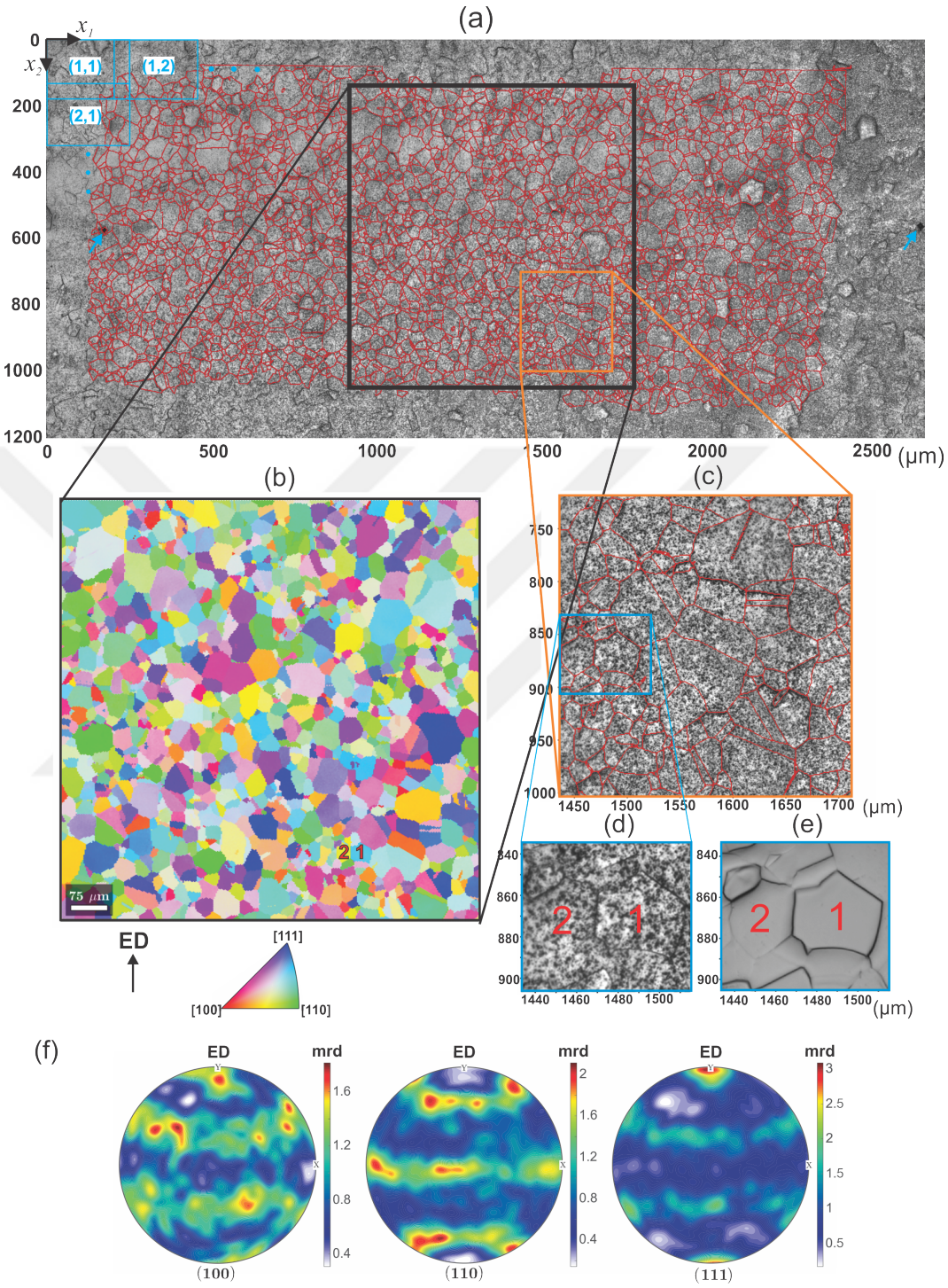

Figure 3.5. (a) Stitched microscopic image of ROI overlaid with grain mask, (b) EBSD orientation map of highlighted zone in (a), (c) Close-up view of grain mask overlaying onto microscopic image, (d) and (e) after and before speckle pattern application, (f) Pole figures.

First, grain boundaries in ROI are revealed manually with a layer-based image processing software and splines tools to mimic grain boundaries correctly over the pre-EBSD imaging, while orientation maps were also employed as an auxiliary tool. Some boundaries (mostly non-etched boundaries), which are not revealed in optical images, are visible in EBSD generated orientation maps. After finalizing the grain mask over the pre-EBSD scanning, this mask was mapped onto the first scan of the DIC imaging. During the mapping, a few dozens of anchor points (same material points in both images) are selected uniformly and correspondingly from the overall zones of both mask and first DIC image scan. Later, the mask is deformed with a uniform affine transformation [65], while the anchor points provide an exact match of the same material points in each image and the generated grain mask was verified by visual inspection. Each closed contour (namely grain) is found over aggregate with the *findContours* algorithm of the opencv library [65]. Each grain is then named with a unique ID.

After DIC scans, displacement fields are known. Having displacement fields can later be used to map grain masks onto different load points, which is called reference point variation of the DIC in this study.

3.6.3. Loading with in-situ Area Scanning Microscopic DIC

A typical tensile curve contains information about the total strain corresponding to the applied stress (except for the elastic portion of the curve). The total strain, denoted as ε_{total}, is the sum of the elastic and plastic strains: $\varepsilon_{total} = \varepsilon_{elastic} + \varepsilon_{plastic}$. The simplest method of distinguishing between elastic and plastic strains is by unloading the material during a tensile test. During unloading, only the elastic strain is recovered. If the DIC algorithm can differentiate between these strains, it becomes possible to measure the elastic strain in a polycrystalline aggregate. However, the current resolution of the point-wise (subset-wise) DIC algorithms is insufficient for directly measuring elastic strains. Nonetheless, by obtaining multiple results from the same material area, specifically grains, it becomes feasible to sense the average elastic

strain. This is why the tensile test in this study encompasses both the loading and the unloading regions (see Section 4).

The accuracy of strain measurements using subset-based DIC analysis requires optimization of various parameters, such as subset sizes, speckle patterns, magnification, intensity of digital images, and focusing. To achieve sub-grain resolution strain measurements, subset sizes should be much smaller than the grain size. Opting for a relatively high magnification (40X) is helpful in increasing the number of subsets per grain. However, this can subsequently lead to focusing issues due to surface tilting or deformation-induced topographic features in the region. To tackle this challenge, an auto-focusing algorithm has been implemented.

A key aspect of this study involves developing a statistical understanding of the grain-resolved elastic and plastic deformations in polycrystals. Therefore, comprehensive area scanning is essential to encompass as many grains as possible within the region of interest. However, area scanning involves resource-intensive post-processing operations. To mitigate this, an auto-locating algorithm has been integrated into the area scanning process. Auto-locating aligns the centers of each image pair (reference and deformed), simplifying the post-processing of image and data stitching. Successful stitching of data and stitching of images per frame requires no physical gaps between each frame at each load point. It is known that when deformation increases, the center position of each frame will shift. This shift can cause physical gaps. As a preventive measure, the overlapping region for each frame is planned as 400 pixels for each side of the frame.

3.7. Data Analysis

3.7.1. DIC Algorithm

To have successful DIC measurements, computational solver is important as well as speckle pattern and optics. DIC algorithm is crucial to calculate displacement fields

between the reference image and the deformed image. To calculate the displacement field for each pair of DIC images, a fast and robust algorithm [66] is implemented. The algorithm uses the Gauss-Newton inverse composition (IC-GN) approach rather than the conventional Gauss-Newton methods (iterative least squares and forward additive) [67, 68] and prevents computational redundancy and increases accuracy.

After the displacement fields **u** and **v** are calculated, then strain can be calculated. For the calculation of the strain, partial derivatives of the displacement fields should be calculated with respect to the **x** and **y** axes. With a displacement field in 2D, infinitesimal strains can be calculated with derivatives of displacement field (Equation 3.2). Due to the nature of DIC, displacement fields contain some errors that are sourced by optics, light conditions, speckle patterns, algorithm, etc. Additionally, the strain response of conventional numerical differentiation methods (like central differences) is significantly affected by the aforementioned errors. In this study, a convolution based differentiator [69] is implemented (Equation 3.3) to smoothen up error signal while calculating strains (Figure 3.6). Strain definition and numerical strain are

$$\varepsilon_{ij} = \tfrac{1}{2}\left(\tfrac{\partial u_i}{\partial x_j} + \tfrac{\partial u_j}{\partial x_i}\right) \tag{3.2}$$

$$\varepsilon_{ij}(k,l) = \tfrac{1}{2}\sum_{x=-M}^{M}\sum_{y=-M}^{M} h(x,y)\Big[u_i(k+x,l+y) + u_j(k+x,l+y)\Big] \tag{3.3}$$

where $\mathbf{h}(\mathbf{x},\mathbf{y})$ is the digital differentiator coefficient, $\mathbf{M}$ is equal to kernel radius and is used to define the neighbor cells in the kernel and $\mathbf{k}$ and $\mathbf{l}$ center coordinates of the kernel (See details [69]). In this study, only the first neighbors ($\mathbf{M} = \mathbf{1}$ with a step size of 10 pixels) are taken into account for the strain calculation to prevent extra smoothing (that may cause loss of local heterogeneity) of the strain signals.

Note that after calculating all the strain components, in-plane maximum shear strain can be calculated with the following equation,

$$\varepsilon_{maxsh} = \sqrt{\left(\frac{\varepsilon_{22} - \varepsilon_{11}}{2}\right)^2 + \varepsilon_{12}^2} \tag{3.4}$$

which can provide supplementary information strain accumulation.

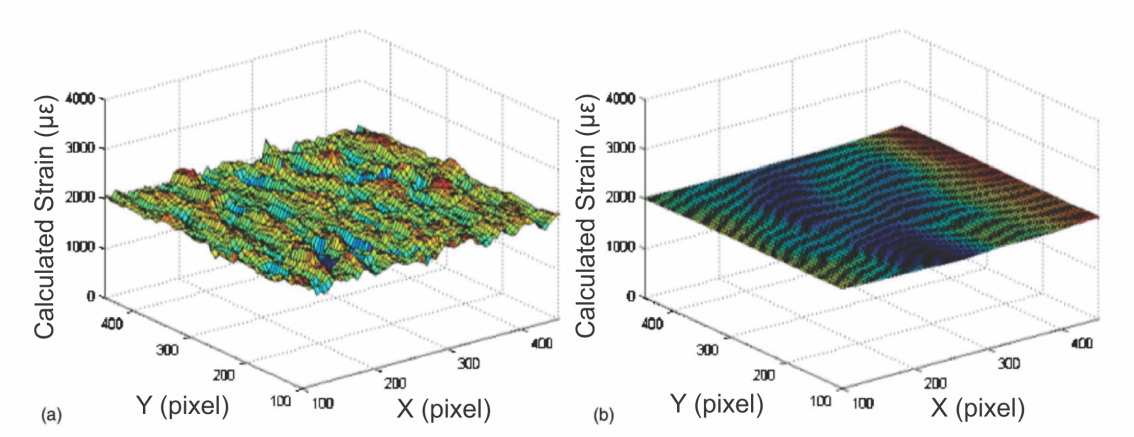

Figure 3.6. Strain calculations with (a) Newton-Raphson and (b) convolution based algorithms for same 2D displacement field [69].

3.7.2. DIC Post-processing Tools

3.7.2.1. Image Stitching. Optical microscopy DIC generally applied with area scan of images to increase the deformation domain over the bulk material. In this study, to include about 4000 grain to the deformation domain, the 2mm x 1mm region is covered with a 13x7 grid of images. An in-house developed scan algorithm, that powered with auto-focusing algorithm and auto-locating algorithm, is used. The auto-focusing algorithm compares different images taken with respect to different positions in the z-direction and finds the best focused image considering the contrast of the image [35]. And the auto-locating algorithm embedded with an FFT-based cross-correlation subroutine [70] that focuses on locating the center displacement of the deformed image with respect to the reference image. With sufficient overlap (400 pixels for both directions) these images are stitched by using sub-pixel stitching algorithm [71] of ImageJ-Fiji [72] without losing any information over the field. After stitching images, ImageJ-Fiji creates a log file of stitching coordinates that latter be used in stitching the displacement, rotation, and strain data fields.

3.7.2.2. Data Stitching. The DIC algorithm takes a frame, divides it into grids, and then compares the displacement using subsets. Subsequently, this 2D displacement field is stored separately for each frame. Despite having sufficient overlaps between

images, the slight x-y offsets between two frames raise concerns regarding stitching data. This is where the image stitching coordinates of ImageJ-Fiji come forward. The data stitching algorithm utilizes these coordinates to establish a global grid for the entire domain. Subsequently, this grid is filled with the data from each frame with the consideration of accurate spacing and physical gaps between images.

3.7.2.3. Grain Mask Mapping. After data stitching, full-field displacement fields are available for each load point of the DIC analysis. Having accurate displacement fields enables mapping the grain mask (that is generated for only the reference load point) to any load point by using a first order rectangular bivariate interpolation algorithm [73]. This algorithm takes displacement fields in the x-y direction and creates first order interpolation functions for both displacement fields. Then the coordinates of the reference grain mask are fed into these functions to find the displacement of each coordinate of the deformed grain mask. Later, using a mapping function (*ndimage.map_coordinates*), grain mask is reconstructed with respect to these displacements without any interpolation or extrapolation of the grain IDs in the original grain mask. Then this mapped grain mask is overlaid with a deformed full field image, and alignments of the features (triple points, boundaries and fiducial marks) are verified with visual inspection.

Grain mask mapping is a crucial method for this study, and it forms the basis of the DIC reference variation method (see Section 3.7.3) that is one of the contribution of this study to the literature, best of author's knowledge.

3.7.2.4. Full-field Outlier Reduction. During the DIC analysis, there are multiple sources of errors that alter displacement results [50], [74, 75]. These errors can cause extreme strain signals, which are easily noticeable. These extreme errors can be eliminated by a standard deviation based outlier reduction algorithm [76]. This algorithm, known as *sigma.clip*, identifies and removes outliers from a distribution that fall beyond the limits of the average signal by ± 3 times the standard deviation ($\pm 3 \times$ std).

Implemented through two recursive steps across full-field strain signals, the algorithm eliminates less than 0.2% of the total signal. This process helps prevent the detrimental effects of erroneous signals on grain averages.

3.7.2.5. Binary Operations. A measure of robustness proposed in this study employs binary morphology over the grain mask (GM), which defines the region of the grain over the strain fields. The idea is that if the GM is stripped of one data layer (only a $1\,\mu m$ band at the outside boundary) and the calculations are repeated, the results should show only (if any) a contained physical change. The reason erosion is considered as a robustness measure in the first place is related to the fact that averaging will tend to annul the effect of outliers inside the averaging region, but is more vulnerable against those on the boundary. So, if we gently alter the boundary by stripping a small distance, huge variations will point to surface outliers and an unreliable estimate, while a contained variation will support the viability of the results.

In application, the reported grain averages already correspond to one-layer-stripped ($n = 1$) grain masks to avoid the outermost data ring that has a significant overlap of the subset with neighboring grains. We will consider analysis after stripping $n = 2, 3, 4$ layers as well (the final with $4\,\mu m$ erosion is still contained compared to the large sizes of the grains, on average $25\,\mu m$) and expect small variations among these.

3.7.3. DIC Reference Point Variation

The DIC reference point variation is an internal measure of robustness that uses multiple load points as the DIC reference, which actually implies a full repetition of the DIC analysis by picking different reference points. While not typically undertaken, this check is available for any in-situ DIC study with numerous data points. If the results are robust, when the DIC reference point is altered, the computed trends should remain equivalent, aside from a trivial shift in strains (since the zero point of strain is shifted to the new reference).

In this study, for reference load points where all analysis will be repeated, we will pick top and full-unload points, T and U (Figure 4.2) as well as point M, the virtual middle point in the unload (Figure 4.2). It should be noted that when the reference point (RP) is changed, virtually all image pairs that are used in the DIC calculations are changed, making it an independent test. Further, the aforementioned strain shift associated with altering the reference is not even a factor when computing the *slopes* of unload.

3.7.4. Slip Trace Identification via Residual Intensity

In this study, a recently developed residual intensity technique [70] is used to identify / enhance slip traces over grains in the polycrystalline aggregate. This technique detects abrupt changes of intensity field over the material field. During the slip and twinning, deformations are concentrated locally over the domain, and these concentrated deformations cause the change of intensity of pixels around deformation.

For a single crystal, the slip is expected to start in the slip system with the highest SF. However, slip patterns may have differences for polycrystals. But the slip is still expected to occur over a high SF slip plane. For the region of interest, we have orientation of grains that enables per grain calculation of each SF of 12 slip systems, as well as their direction and plane traces over the x-y plane (or ROI) can be calculated. These calculated traces of the slip plane and direction can be compared with slip traces emerging over residual intensity maps per load point.

3.8. Numerical Modeling of the Polycrystalline Aggregate

Columnar grain domains for spectral analysis are produced directly from actual EBSD maps using Dream3D [77]. (Since the DAMASK domain is physically an extrusion of the EBSD map, e.g., Figure 3.5(b), its image is excluded for brevity.) The voxel size of the analyses also nominally obey the 3 μm spacing utilized in the EBSD scans. DAMASK spectral analysis is used for its high efficiency with its standard

power-law viscoplastic model [34]. The material constants of the model are tuned to fit the stress-strain curve of the current experiment (shown in the results Section 4, Figure 4.2) within 2%. These constants are provided in Table 3.3. As typical, the high value of the exponent n yields virtual rate independence. To compare directly with the experimental data on unload, DAMASK analysis is also generated with the unload step after plastic loading with multiple intermediate data points. The details of modelling equation, parameters and stress results are given in the Appendix A.

Table 3.3. Pure nickel elastic constants in stiffness and compliance [4] (first row); anisotropy ratio (AR), extremal values of isostress stiffness and compliance (second row); utilized DAMASK [34] pheno-power law constants for spectral analysis (third row).

c_{11}	c_{12}	c_{44}	s_{11}	s_{12}	s_{44}
(in GPa)			(in TPa^{-1})		
246.5	147.3	124.7	7.34	-2.74	8.02
AR	E_{100} ; E_{111} (GPa)		E_{100}^{-1} ; E_{111}^{-1} (TPa^{-1})		
2.51	136.2 ; 303.6		7.34 ; 3.29		
$\dot{\gamma}_0(s^{-1})$	ξ_0	ξ_∞(MPa)	h_0(GPa)	α	n
10^{-3}	29.1	240	0.97	2.25	83.3

4. EVALUATION OF GRAIN-AVERAGED ELASTIC STRAINS

4.1. DIC averaging

The fact that averaging of the DIC fields improves the precision of the average (while sacrificing resolution) is known and commonly utilized (e.g., deriving a stress-strain curve from a tensile test with DIC strain measurement). One way to explain this effect is noting that the DIC strain uncertainty goes by the DIC displacement uncertainty divided by the data spacing and, upon averaging, the effective data spacing is expanded (to the size of the averaging domain)[3] . Thus, averaging roughly reduces the uncertainty of the DIC by a factor $1/n$ where n is the number of data points averaged *over a single dimension*. For an equiaxed grain with N data points *over the area*, $n \sim \sqrt{N}$. Hence, for the characteristic grain sizes and data spacing here, an accuracy gain of around $n \sim 25$ might be postulated for grain-averaged strains. Based on the previously noted local DIC uncertainty, this crude analysis points to a grain-averaged strain uncertainty of approximately 20 $\mu\varepsilon$.

These postulates with uncertainty, however, are based on normal distributions, whereas large-scale (DIC) data is bound to contain outliers. Consequently, all operations (average, standard deviation, etc.) over strain fields are performed with robust estimators in this study, by a recursive removal of points outside three standard deviations (sigma clipping, astropy package [76]) (mentioned as outlier reduction). The number of removed points typically remain very limited, approximately below the order of 0.2% all data points.

[3]For a quick sketch of this notion, consider a one-dimensional displacement array u_i, i=1,...,n+1 and a simplistic determination of strain with $\varepsilon_i = (u_{i+1} - u_i)/\Delta$, where Δ is the grid spacing. The average strain over N data points can easily be simplified to $\overline{\varepsilon} = (u_{n+1} - u_1)/(n\Delta)$, noticing successive cancellations. If δu represents the uncertainty of displacement, the uncertainties in local and averaged strains are $\delta\varepsilon_i = 2\delta u/\Delta$ and $\delta\overline{\varepsilon} = 2\delta u/(n\Delta)$, respectively, where $n\Delta$ is the chord length of the averaging domain.

Grain averages are denoted by overbars, e.g., $\overline{\varepsilon}_{22}$ stands for the grain-averaged axial strain. The designation for full-field average (which is also the average over all grains) is further enveloped by angle brackets, e.g., $\langle\overline{\varepsilon}_{22}\rangle$.

Similarly to diffraction studies, the vertical axis of some plots in this study will be the applied stress (load divided by cross-sectional area), σ_{app}, whereas the horizontal axis is grain-resolved strain. σ_{app}, is equivalent to either true or engineering stress given the limited strains ($< 0.6\%$) here. Also notice,

$$\sigma_{app} \simeq \langle\overline{\sigma}_{22}\rangle \tag{4.1}$$

over a *representative* micro-DIC domain.

4.2. Estimation of the average grain stress via a partial unload

First, consider a one-dimensional (1-D) analogy/verification over the macroscopic tensile test using Figure 4.1. T, U designate the top and fully-unloaded points, respectively. U′ is the (hypothesized) point of full *elastic* unload. Defining U′ is hardly necessary in the 1-D analogy, but will be conceptually important in the actual tensorial case that is brought up next. Suppose elastic compliance $S = d\varepsilon/d\sigma_{app}$ is measured by fitting the data points over an unload, only considering those (shown with blue-bold markers) that largely precede significant reverse plasticity. With trivial trigonometry, the estimate for elastic strain release upon unload is then $\varepsilon_{el} = S\,(\sigma^{T}_{app} - \sigma^{U'}_{app}) = S\,\sigma^{T}_{app}$ with $\sigma^{U'}_{app} = 0$. Also considering $\sigma^{T}_{app} = E\,\varepsilon_{el}$, where E is the tabulated Young's modulus, one gets

$$\sigma^{T}_{app} = E\,(S\sigma^{T}_{app}). \tag{4.2}$$

Here, to serve the analogy, the quantities in the parentheses are experimentally measured whereas E is gathered from literature. Clearly, a trivial equality $\sigma^{T}_{app} = \sigma^{T}_{app}$ ensues with an expected $E = 1/S$ for this 1-D case.

To construct an analogous tensorial case for stress estimation of a grain with orientation $\mathbf{g}$, single crystal elastic constants (Table 3.3) are gathered from literature (in place of E in the 1-D case). σ_{app} now is reduced to a load parameter, proportional

to the measured $\overline{\varepsilon}_{\alpha\beta}$, $\alpha, \beta = 1, 2$ over the partial unload. For each $(\overline{\varepsilon}_{\alpha\beta}, \sigma_{app})$ data set in this range, the stress slope

$$\tilde{S}_{\alpha\beta} = \frac{\partial \overline{\varepsilon}_{\alpha\beta}}{\partial \sigma_{app}} \quad , \ \alpha, \beta = 1, 2 \tag{4.3}$$

is once more found by linear regression. The grain-averaged stress estimate in analogy to Equation 4.2 (with measured quantities again in parentheses below), is then given by,

$$\overline{\sigma}^{TU'}_{\alpha\beta} = \mathbf{C^g}(\tilde{S}_{11}\sigma^T_{app}, \tilde{S}_{22}\sigma^T_{app}, \tilde{S}_{12}\sigma^T_{app}) \tag{4.4}$$

$$\overline{\sigma}^{TU'}_{\alpha\beta} = \overline{\sigma}^{T}_{\alpha\beta} - \overline{\sigma}^{U'}_{\alpha\beta} \tag{4.5}$$

$$\tilde{S}_{\alpha\beta}\sigma^T_{app} = \overline{\varepsilon}^{T}_{\alpha\beta,el} - \overline{\varepsilon}^{U'}_{\alpha\beta,el} \ , \quad \alpha, \beta = 1, 2. \tag{4.6}$$

The complication that the reference state U′ is retained in Equations 4.4-4.6 is physically due to the fact that when the aggregate is elastically unloaded (with the aggregate average taking a value of $\sigma^{U'}_{app} = 0$ at U′), individual grains do not have to realize a zero stress state (but rather just a zero sum.) we will further discuss $\overline{\sigma}^{U'}_{\alpha\beta}$ as a type-II residual stress field. Currently, note that $\overline{\sigma}^{T}_{\alpha\beta} \gg \overline{\sigma}^{U'}_{\alpha\beta}$ is typical, in which case, the point-T stress is approximated well by Equation 4.4, i.e., $\overline{\sigma}^{T}_{\alpha\beta} \simeq \overline{\sigma}^{TU'}_{\alpha\beta}$.

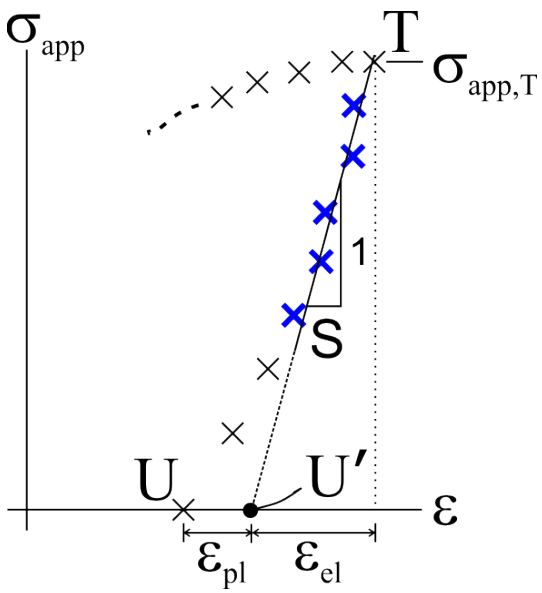

Figure 4.1. One dimensional analogy/verification of the stress estimation idea by fitting compliance S over the initial segment of the unload.

The linear operator $\mathbf{C^g}$ in Equation 4.4 stands for the elastic constitutive relationship for orientation $\mathbf{g}$ that is embedded in the traction-free boundary conditions of this surface measurement. The role of linear regression (in defining $\tilde{S}_{\alpha\beta}$ in Equation 4.3 or S in Figure 4.1) is to enhance the accuracy of elastic strain estimate (Equation 4.6) by using multiple data points.

Writing out the terms of Equation 4.3 by incorporating Equation 4.1,

$$\tilde{S}_{22} = \frac{\partial \overline{\varepsilon}_{22}}{\partial \langle \overline{\sigma}_{22} \rangle},\ \tilde{S}_{11} = \frac{\partial \overline{\varepsilon}_{11}}{\partial \langle \overline{\sigma}_{22} \rangle},\ \tilde{S}_{12} = \frac{\partial \overline{\varepsilon}_{12}}{\partial \langle \overline{\sigma}_{22} \rangle} \tag{4.7}$$

explains the switch to a neutral term, stress slope, for $\tilde{S}_{\alpha\beta}$. Specifically, the numerator-denominator components of both $\tilde{S}_{11}$ and $\tilde{S}_{12}$ do not agree, making these two merely slopes with respect to the loading parameter, σ_{app}. Only $\tilde{S}_{22}$, while noting it is a division of grain average to aggregate average, can be considered an *effective* compliance.

4.3. Aggregate average

Figure 4.2(a) shows the results of the DIC analysis (conducted with reference point O) averaged over the entire micro-DIC domain [Figure 3.5(a)], denoted by $\langle \overline{\varepsilon}_{22} \rangle$, $\langle \overline{\varepsilon}_{11} \rangle$ for axial and transverse strains, respectively. This plot shows the entire load history with all the points at which area-scanned micro-DIC data is collected. The unload we will focus on, has 11 points numbered u0,...,u10 with the top (T), middle (M), and full-unload (U) points coincident with u0, u5 and u10, as shown. The aggregate-average $\langle \overline{\varepsilon}_{12} \rangle$ is extremely limited [range shown in Figure 4.2(a)], with numbers around 1/30th the axial strains. Normally, this would only be noted as a perfectly acceptable approximation to the targeted uniaxial stress state, however, we further zoom into the very limited strain interval of $\langle \overline{\varepsilon}_{12} \rangle$ in Figure 3.5(b) to present that the $\mu\varepsilon$ trends of $\langle \overline{\varepsilon}_{12} \rangle$ (over initial linear ramp, plasticity, and unload) are also resolved, attesting to the amplified sensitivity of the DIC measurement upon averaging. Through the comparison of Figure 4.2(a) and (b), we note the stylistic choice of sticking to $\mu\varepsilon$ (microstrain) units all through the manuscript. This is to promote the fair evaluation of the varying strain

ranges in the plots, noticing the magnitudes [as in Figure 4.2(b)] that are outside the typical DIC accuracy.

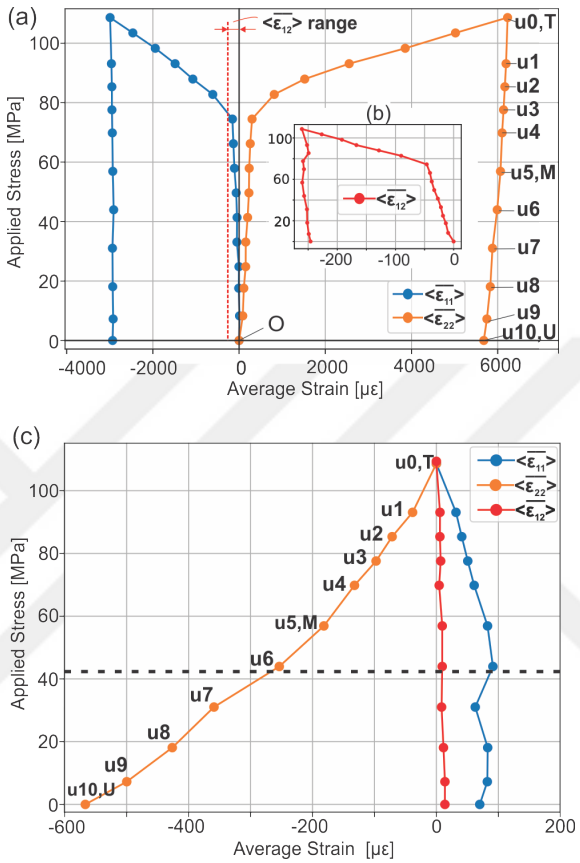

Figure 4.2. (a-b) Full-field average stress-strain curves wrt point O, (c) Full-field average unloading curves wrt point T (u0).

Figure 4.2(c) (another plot in this category) zooms into the unload for full-field averages. The DIC here is conducted with respect to point T, yielding a zero strain value at T for a direct presentation of strains that are realized over the unload. There is a linear trend in $\langle\overline{\varepsilon}_{22}\rangle$ and $\langle\overline{\varepsilon}_{11}\rangle$ in the initial segment of the unload that falters after u6, signified by a dashed line in Figure 4.2(c). The partial unload range over which the behavior of the polycrystal is regarded to be virtually elastic is accordingly determined, and u1,...,u6 are taken as the unload points over which the slopes are henceforth determined. The slopes of the aggregate data in Figure 4.2(c) for $\partial\langle\overline{\sigma}_{22}\rangle/\partial\langle\overline{\varepsilon}_{22}\rangle$ and $\partial\langle\overline{\sigma}_{22}\rangle/\partial\langle\overline{\varepsilon}_{22}\rangle$ (again, recall Equation4.1) over the range u1-u6 are 240 and -710 GPa, respectively. Both fits have a r-squared value above 0.98. The division of these slopes

yields a Poisson ratio, $-\partial\langle\bar{\varepsilon}_{11}\rangle/\partial\langle\bar{\varepsilon}_{22}\rangle$, of 0.338. The domain-averaged DAMASK results over the unload are largely consistent with 232 GPa for axial stiffness and 0.3 for Poisson's ratio. With $\langle\bar{\varepsilon}_{12}\rangle$ remaining near null as well; these type-I results describe a perfectly sensible elastic unload (of an uniaxial stress state) in the prescribed range, u1-u6. As a side point, the typical elastic Poisson ratio of 0.3 (output from both experiment and model results) can be put in perspective of the typical 0.5 that is virtually equal to the division of point T's total transverse strain ($-3215\,\mu\varepsilon$) to its total axial strain ($6450\,\mu\varepsilon$) in Figure 4.2(a) at the end of the loading. This is the ideal value of the strain ratio after isochoric plastic strains dominate in a (transversely) isotropic material—sensible given the transverse isotropy of the extruded sample [42].

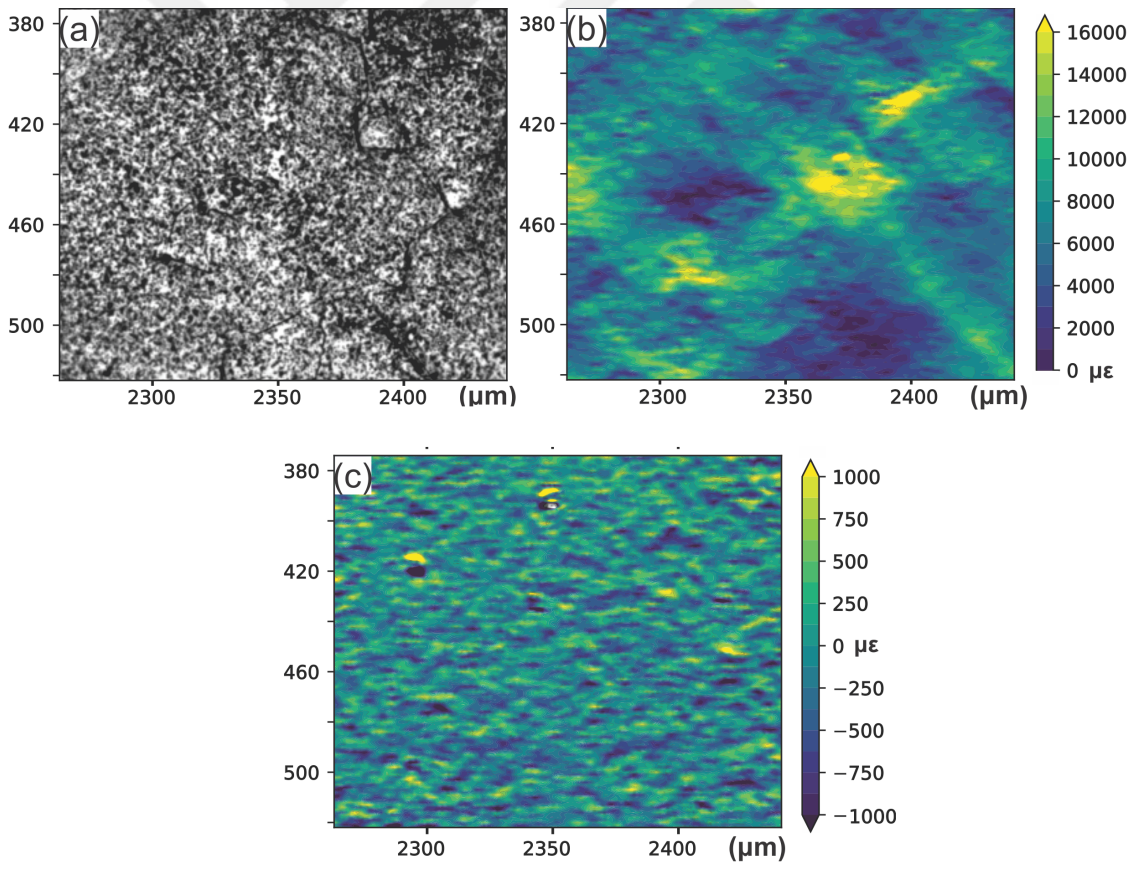

Figure 4.3. (a) An $150 \times 180\,\mu m^2$ grain neighborhood over which DIC results are shown with contour plots: (b) total axial strains, ε_{22} at point T (reference point O), (c) incremental axial strain field upon a nominal 15 MPa unload (second unload point u2 calculated with respect to top point T). See Figure 4.2 for load point definitions.

Plastic strains that are out of the general scope of the current treatise admit themselves to spatially-resolved results; e.g., consider the total axial strain results at point T in a selected material neighborhood [Figure 4.3(a)], contour plotted in Figure 4.3(b). The ε_{22} fields (that rise above the measurement uncertainty) describe the typical physical picture of polycrystal plasticity with loose $\pm 45^{\circ}$ banded formations [38].

Figure 4.3(c), which shows the contrasting and more topical point, presents ε_{22} fields over a small unload, with a DIC comparison of point u2 with respect to point T. Though, obviously the colorbar had to be adjusted for much smaller magnitudes of the DIC fields (about 1000 $\mu\varepsilon$), the field values are still significantly above the elastic strain signal [e.g., observe the full-field average value 70 $\mu\varepsilon$ over Figure 4.2(c)] and the spatial distributions present mere noise. In other words, the physical DIC signal is buried below the noise floor, and, consequently, the (elastic) strains over the partial unload do not admit any spatially-resolved representation. The next section delves into the premise of the study—locally averaging these fields over respective grains—and evaluating if the corresponding noise cancellation (recall Section 4.1) can yield (type-II) physical measurements.

4.4. Selected individual grain evaluations

Figure 4.4 brings together all salient features of the proposed grain-resolved assessment, specialized to a well-behaved grain called grain A. The first row pertains to morphology. Recall stitched image fields at different reference points (RPs) T, M and U are independent as well as the grain masks (GMs); GM-mapping for different RPs have been detailed in Section 3.7.2.3. The declared local confirmation in this section is presented here. Figure 4.4(a) is the bare image crop (about grain A) from RP-T image fields, whereas Figure 4.4(b) is the GM generated for RP-T overlaid on this crop. Figure 4.4(c) and (d) are the equivalent plots from image fields and GMs of RP-M and RP-U, respectively. Through the visible triple point on the left side (marked with an arrow) as well as other prominent features/speckles, note that each GM correctly identifies the grain(s) despite the natural variations in $x_1 - x_2$ axes among the

field coordinates of the three load points [apparent over a close inspection of the axes in Figure 4.4(b-d)] This also means that, without adequate GM-mapping, the field correspondences would not be correct.

The second row (Figure 4.4(e-h) presents the statistics of the data cloud inside the grain (3228 total data points with the default single layer erosion, Section 3.7.2) when independent DIC calculations made with respect to RPs T, M and U. Specifically, the second unload point (u2) result in Figure 4.4(e) corresponds to u2 image analyzed with respect to load-T image where as the same point in Figure 4.4(h) corresponds to u2-image analyzed with respect to load-U image. The zero-strain in each DIC set is naturally carried to the corresponding RP, and the zero-axis marked with dashes passes through T, M and U in Figure 4.4(e), (g), and (h), respectively.

The blue and pink shades in Figure 4.4(e-h) correspond to the one and two standard deviation (σ, 2σ) envelopes of the grain-A data cloud for each DIC analysis over the unload. For RP-T, Figure 4.4(e) boundaries can be corresponded with actual histograms for selected data points, provided in Figure 4.4(i). The data percentage inside (σ and 2σ) envelopes at each DIC point is calculated (for RP-T, ε_{22}, median 69.8 and 95.4%, respectively) and, this near conformance to the Gaussion-distribution bounds (68.3 and 95.5%), applies to all RP and strain components (ε_{22}, ε_{11}, ε_{12}). Note, for brevity, Figure 4.4(e-i) addresses data statistics for ε_{22} only. At the center of each cloud in Figure 4.4(e-h), there is the grain average shown with markers. The main point, further highlighted by adding a single data point (CM at the centroid of the grain) over the envelopes and a data-range zoom in Figure 4.8(f), is clear: although individual data points are severely scattered (noise much larger than signal), their mean demonstrates the physical trend of the unload similar to the full-field average, Figure 4.2(c).

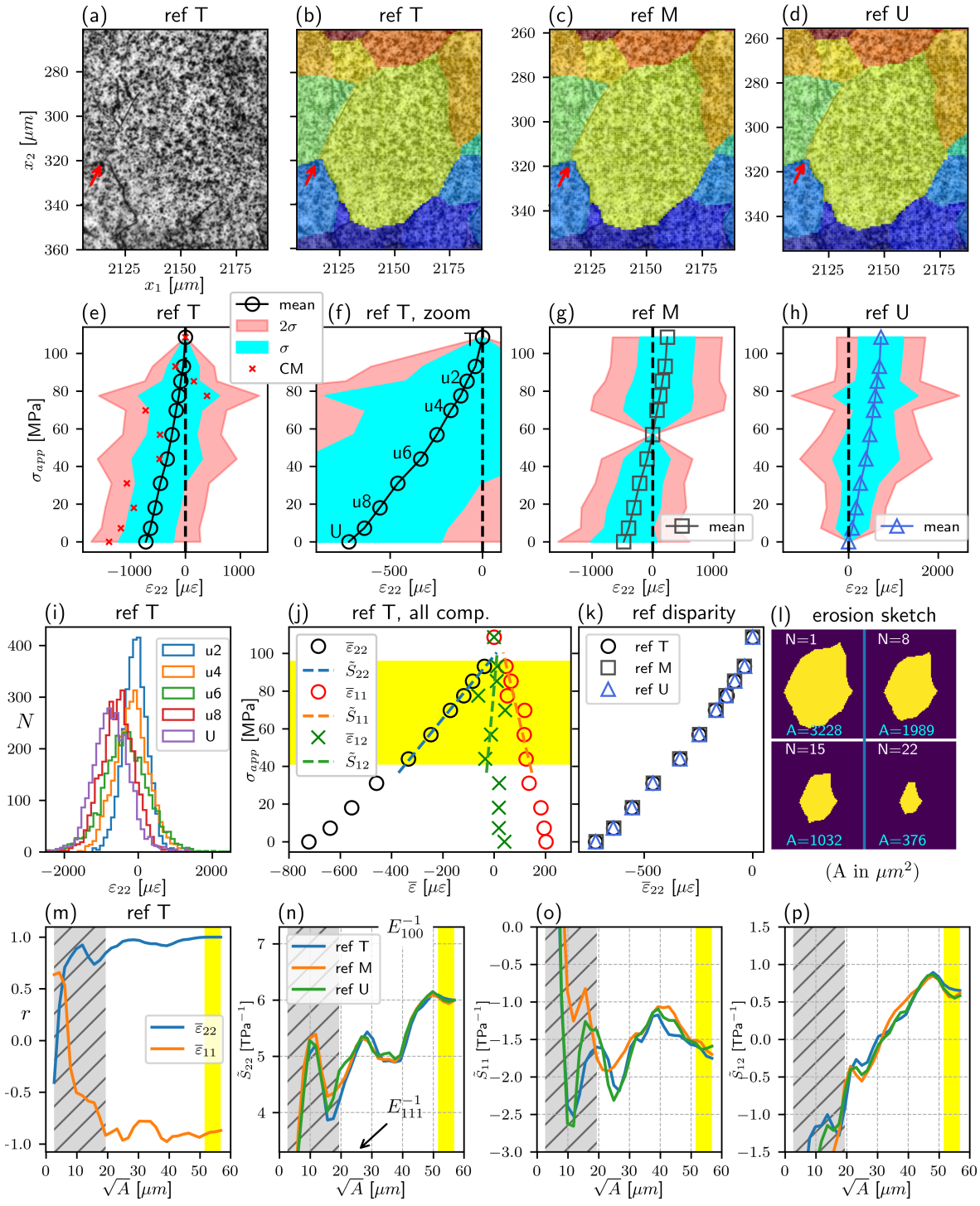

Figure 4.4. (a) DIC image (grain A) RP-T, (b, c, d) RP-specific GMs (T, M, U). ε_{22} data clouds vs. σ_{app}, (e, f) at T, (g) at M, (h) at U, (i) grain A ε_{22} histograms, (j) grain-averaged, $\bar{\varepsilon}_{22}$, $\bar{\varepsilon}_{11}$, $\bar{\varepsilon}_{12}$, (k) Aligned $\bar{\varepsilon}_{22}$ results, (l) different-sized regions R, (m) r, for $\bar{\varepsilon}_{11}(R)$ and $\bar{\varepsilon}_{22}(R)$, (n) $\tilde{S}_{22}(R)$, (o) $\tilde{S}_{11}(R)$, (p) $\tilde{S}_{12}(R)$ vs. $\sqrt{A}$ of region R.

The grain averages for all components are put together in Figure 4.4(j), again with sensible behavior observed in each. The linear fits (performed in the fitting interval u1-u6, highlighted with yellow) are added to the figure and labeled by their slopes, $\tilde{S}_{\alpha\beta}$. These averages correspond to RP-T calculations, but that is hardly important for grain A with exceptionally low RP-discrepancy. Also, valid for other components, this is presented for ε_{22} in Figure 4.4(k); the data points are virtually coincident when RP-M and -U grain-averages [from Figure 4.4(g), and (h)] are appropriately shifted[4] on to the RP-T results.

Figure 4.4(l) presents the process of producing consecutively larger regions about the grain core, though by a backwards process of layer-by-layer stripping (layers counted by n, Section 3.7.2) from the full grain mask. Each region can be called R with a corresponding area, A. (Recall, with the virtual 1 μm data-spacing, A also corresponds to the number of data points in R.)

If the entire process of region-averaging and linear fitting is carried out for all R, and the results are plotted against corresponding area (more precisely, $\sqrt{A}$ in μm for easier understanding and homogeneous data spacing), Figure 4.4(n-p) are generated for the slopes $\tilde{S}_{\alpha\beta}$ and Figure 4.4(m) for the correlation coefficient, r. The robustness criteria of near-equivalence-of-$\tilde{S}_{\alpha\beta}$ over $n = 1, .., 4$ concerns only the last four data points in these graphs, highlighted by the vertical yellow band. Inclusion of the rest is for discussion. For visualizing the left limit of the graphs, $A \to 1$, one can simply look at the centroid (CM) data in Figure 4.4(e) to note that the linear fit to this level of noise is very meaningful. The correlation coefficients in Figure 4.4(m) only reach decent values when the averaging domains are sufficiently large. Below this, as the figurative gray-shading indicates, the $\tilde{S}_{\alpha\beta}$ values are not to be considered. The use of r (instead of its square) in Figure 4.4(m) allows highlighting the different-sense correlations of $\overline{\varepsilon}_{22}$ and $\overline{\varepsilon}_{11}$ with σ_{app} over the plot. (Note the much smaller $\overline{\varepsilon}_{12}$ is hardly correlated with

[4]The strain-shift value for RP-M (RP-U) is objectively determined as the distance between the center of mass of the linear fit for the RP-M (RP-U) data and the RP-T data. Only the latter fit is shown, labeled as $\tilde{S}_{22}$ in Figure 4.4(j).

σ_{app}, making its r-values non-informative and small—in general, $r \to 0$ for zero-slope data.)

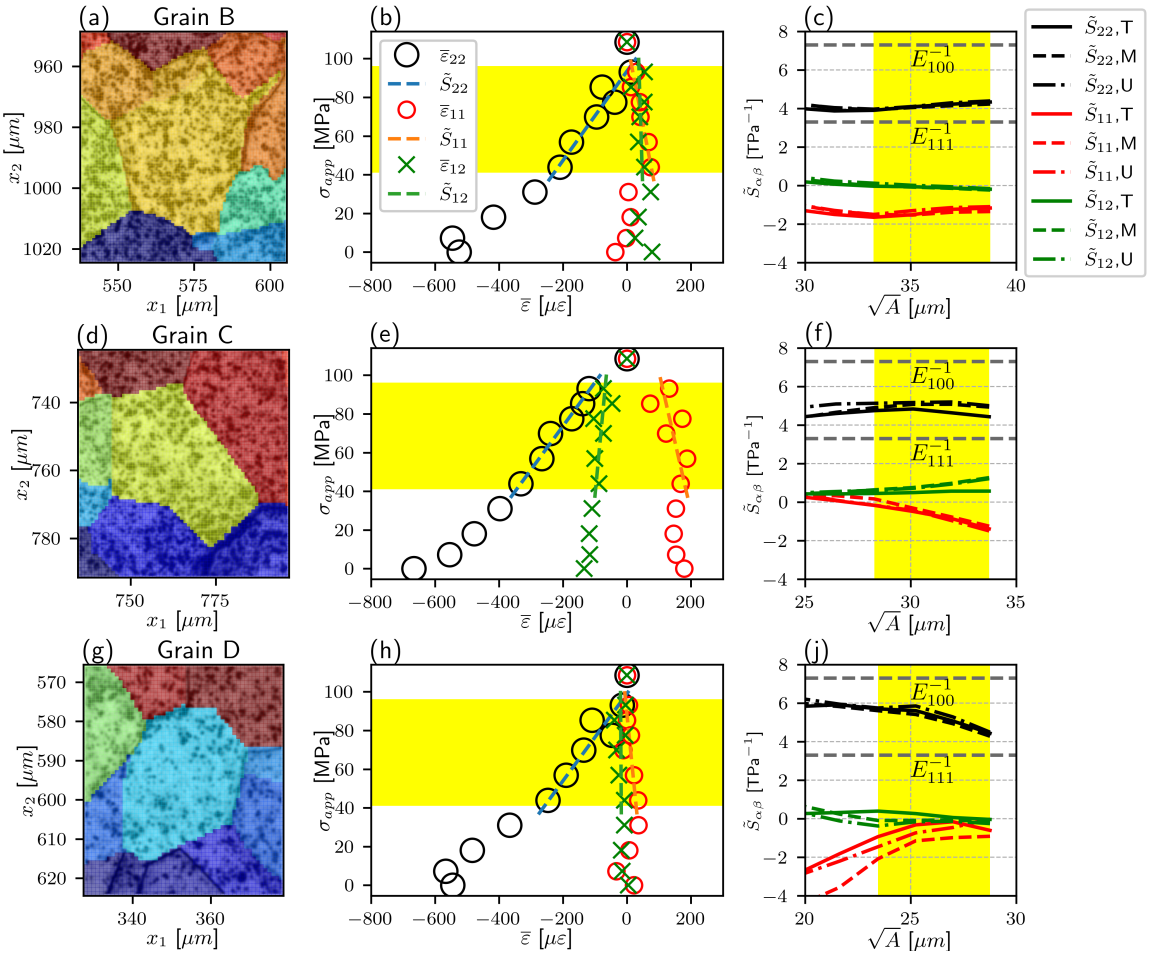

Figure 4.5. For grain B, (a) image-grain mask overlay (grain B at center) at reference point T, (b) grain-averaged strain components over the unload, (c) calculated stress slopes $\tilde{S}_{\alpha\beta}$; (d), (e), (f) similarly for grain C; (g), (h), (j) similarly for grain D. For more details, see the caption of Figure 4.4.

Leaving the intra-grain variations of stress-slopes to Discussion, let us emphasize the main function of independent-RP calculations: RP-T, RP-M and RP-U calculations yield a strong agreement for $\tilde{S}_{\alpha\beta}$ in Figure 4.4)(n-p) in the robustness-criterion range (yellow band). To quantify, the standard deviations, $\delta\tilde{S}_{\alpha\beta}$ of 12 data points in this band are provided in the grain-A row of Table 4.1 (column 6). Discrepancy, D, the RMS-value defined in Equation 4.8 is placed under $\delta\tilde{S}_{\alpha\beta}$ in parentheses. $D = 0.06$ is

two orders below $\tilde{S}_{22}$ for this grain. The means of the 12 data points, on the other hand, are reported as $\tilde{S}_{\alpha\beta}$ in the table (column 5). These are used as the estimations that are fed to the grain-averaged stress calculation of Equation 4.4. The resulting type-II estimates for point-T stress state are provided in the last column.

The orientation of grain-A is provided as a matrix in Table 4.1 where the emphasized second row corresponds to the crystal direction that is aligned with σ_{app} (i.e., this is the hkl in E_{hkl}). From the first order stiffness/compliance measure of E_{hkl}/E_{hkl}^{-1} provided in the same table, grain A is on the compliant side. Notice $\tilde{S}_{22} = 6.01\,\mathrm{TPa}^{-1}$, that could be called effective compliance (Section 4.2) admits a comparison with $E_{hkl}^{-1} = 5.8\mathrm{TPa}^{-1}$. In fact, the limiting values of isostress compliances from Table 3.3 are reasonable reference points, employed as axis limits in Figure 4.4(n). Three more grains (called B, C, and D) that cover a range of elastic stiffness (e.g., inspect E_{hkl} in Table 4.1) are shown in Figure 4.5 with condensed results. In Figure 4.5, each row corresponds to a grain. The first and second column are analogous to Figure 4.4(b) and (j) whereas the third column is a combination of Figure 4.4(n-p) about the robustness-criterion (yellow) band ($n = 1, ..., 4$).

Inspecting Table 4.1, one notes more limited $\tilde{S}_{22}$ for these stiffer grains. In this sense, it is important to look at $\overline{\varepsilon}_{22}$ data together in Figure 4.4(j), Figure 4.5(b), (e), and (h) where the strain-axis ranges are kept identical [also with an eye on the field average in Figure 4.2(c)]. There is noticeable variation in $-\tilde{S}_{11}/\tilde{S}_{22}$, that can be perceived as a grain-effective Poisson's ratio. Large variations in this quantity are also supported by the spectral simulation (italicized in Table 4.1) despite the more regulated predictions in the loading direction ($\tilde{S}_{22}$, $\overline{\sigma}_{22}^{T}$) compared to the experiment.

As we will discuss further later, the spectral simulation should not be taken at all as *bare truth* but as a sanity comparison. $\tilde{S}_{12}/\tilde{S}_{22}$ column validates the expected small values of shear compared to axial strains (sense unimportant).

Table 4.1. Information and results table for selected grains A, B, C, D. Italicized results in parentheses refer to the spectral model.

G	**Orientation** $[\mathbf{g}_{ij}]$	**Area** $(\boldsymbol{\mu}\mathbf{m}^2)$	E_{hkl} (GPa) E_{hkl}^{-1} (TPa^{-1})	$\tilde{S}_{22}$, $\tilde{S}_{11}$, $\tilde{S}_{12}$ (TPa^{-1})	$\delta\tilde{S}_{22}$, $\delta\tilde{S}_{11}$, $\delta\tilde{S}_{12}$ D (r.m.s.) (TPa^{-1})	$-\frac{\tilde{S}_{11}}{\tilde{S}_{22}}$	$\frac{\tilde{S}_{12}}{\tilde{S}_{22}}$	$\overline{\sigma}_{22}^T$, $\overline{\sigma}_{11}^T$, $\overline{\sigma}_{12}^T$ (MPa)
A	0.95 −0.07 0.30 **-0.05 0.92 0.38** −0.30 −0.38 0.88	3433	172 (5.80)	6.01, -1.62, 0.63 (*4.95, -1.92, -0.19*)	0.04, 0.07, 0.06 (0.06)	0.27 (*0.39*)	0.10 (*-0.04*)	125, 25, 16 (*99, 7, -2*)
B	0.75 0.24 0.60 **-0.56 0.73 0.39** −0.35 −0.64 0.68	1654	268 (3.62)	4.14, -1.37, -0.08 (*4.55, -1.03, -0.32*)	0.15, 0.17, 0.09 (0.14)	0.33 (*0.25*)	-0.02 (*-0.08*)	119, -4, -1 (*116, -2, 9*)
C	0.78 0.62 −0.11 **-0.57 0.62 -0.54** −0.27 −0.48 0.84	1264	301 (3.32)	4.93, -0.68, 0.77 (*4.20, -0.62, -0.51*)	0.22, 0.5, 0.26 (0.35)	0.14 (*0.14*)	0.16 (*-0.12*)	162, 8, 3 (*122, 6, 4*)
D	0.81 0.13 −0.57 **-0.38 0.86 -0.34** 0.44 −0.50 0.75	932	209 (4.78)	5.20, -0.82, -0.06 (*4.57, -1.29, -0.75*)	0.53, 0.55, 0.20 (0.46)	0.16 (*0.28*)	-0.01 (*-0.16*)	131, 32, -4 (*122, 5, 2*)

The experimental stress results in Table 4.1 are largely sane in terms of proximity to the effective uniaxial stress, with comparatively low $\overline{\sigma}^T_{11}$ and $\overline{\sigma}^T_{12}$, as well as $\overline{\sigma}^T_{22}$ values that are comparable to the applied stress at point T, $\sigma^T_{app} = 108.1$ MPa.

4.5. Statistics

While the difficult premise that entails searching for very subtle strain magnitudes has been shown over selected grains, the stern quality of the necessary measurement is not realized on a wide scale over the aggregate. Figure 4.6 presents the histogram of discrepancy, D,

$$D = \sqrt{\frac{1}{3}(\delta\tilde{S}^2_{11} + \delta\tilde{S}^2_{22} + \delta\tilde{S}^2_{12})} \tag{4.8}$$

the devised measure of internal consistency. D is most heavily decided by the consistency of slopes when DIC analyses are repeated with respect to different reference loads. For the delicate quantity of $\tilde{S}_{\alpha\beta}$ over an unload, few grains did well with this objectivity measure, and D magnitudes are typically comparable to (or bigger than) actual effective compliances, as shown in Figure 4.6.

To select some *sane* grains, first, an arbitrary D limit (=0.6 TPa^{-1}) is set about an order below the effective compliance and marked on the Figure. (Note, if, e.g., D is demanded to be an order lower, only the most stellar grain, grain A, would meet the limit.) Applying another filter on data linearity[5] , Figure 4.7 and Figure 4.8 plot the stress-slopes and type-II stresses for 43 selected grains in the y-axes. These are put in comparison with full-field spectral analysis (DAMASK) predictions in the x-axes. The horizontal and vertical ranges, in the square plots of Figure 4.7, are kept equal with a 45° near-equality band is placed to aid the eye. This does not imply that SA results are *true*, and equality would mean validation for experimental data points. It is rather a sanity check, and more suited than one against simple isostress results in a limited sense: experimental $\tilde{S}_{22}$ versus SA-$\tilde{S}_{22}$ in Figure 4.7(a) still appear to be less dispersed

[5]This is a combined limit $r(\varepsilon_{22})r(\varepsilon_{11}) < -0.4$ to allow some decent grains, e.g., grain C, with stellar $r(\varepsilon_{22})$ but poor $r(\varepsilon_{11})$ grains [see Figure 4.5(e)]. Over the selected 43 grains, mean $r(\varepsilon_{22}) = 0.88$ whereas mean $r(\varepsilon_{11}) = -0.73$ decidedly worse. This can be in part due to the even more limited $r(\varepsilon_{11})$ signal.

than $\tilde{S}_{22}$ versus isostress-$\tilde{S}_{22}$ in Figure 4.9(a). Rms-difference between experiment and model data points in Figures 4.7(a) and 4.9(a) are 1.38 and 1.71 TPa^{-1}, respectively. The comparison of spectral analysis versus isostress in 4.9(b) is informative as well. Here, the rms-difference is 0.98 TPa^{-1}, but the more important statistical difference between the two is the spread of the compliances and how much the spectral analysis regulates them into a narrow band. (For reference, note the extreme case of regulating the compliance results into a band of zero thickness: This would be the isostrain assumption—with fixed strain values (over the partial unload) for all grains, the slope with respect to σ_{app} would yield a constant line.)

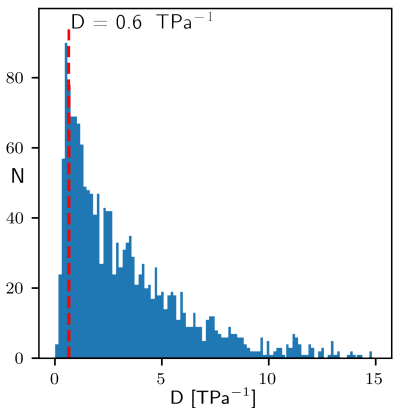

Figure 4.6. Reference point discrepancy, D (Equation 4.8, root mean square of $\delta\tilde{S}_{\alpha\beta}$ over its independent calculations with different reference points and limited field erosions).

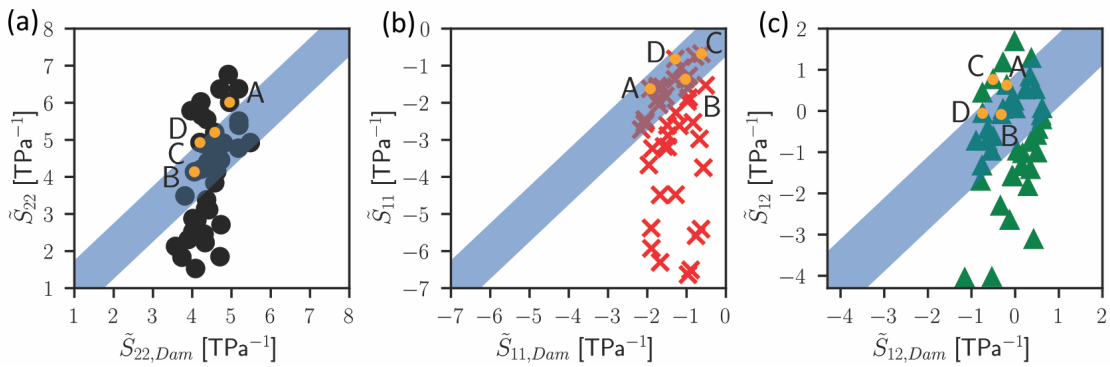

Figure 4.7. Experimental grain-averaged stress slopes ($\tilde{S}_{\alpha\beta}$) versus spectral model (DAMASK) predictions ($\tilde{S}_{\alpha\beta,Dam}$) for (a)$\tilde{S}_{22}$, (b)$\tilde{S}_{11}$, and (c)$\tilde{S}_{12}$.

The perceived over-regulation of the spectral analysis seems to play a part in the data cloud to be rotated vertically in Figure 4.7(a). There is higher confidence on the $\tilde{S}_{22}$ experimental data here as the highest-signal data channel. The average (with the proper grain area weighting) $\tilde{S}_{22}$ of the data cluster in Figure 4.7(a) is found to be 4.1 TPa^{-1} which is in good agreement with the compliance of the bulk (Section 4.3; 1/240 GPa = 4.17 TPa^{-1}) In Figure 4.7(a), multiple data points clustered about 2-3 and 6-7 TPa^{-1} ranges seem to corroborate a larger span of effective compliance in actual fields compared to the spectral model.

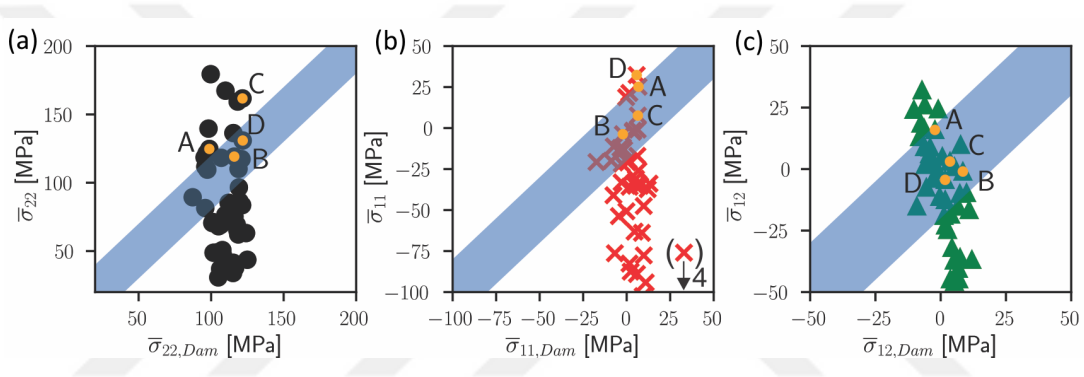

Figure 4.8. For pre-unload point T, experimental grain-averaged stress ($\overline{\sigma}_{\alpha\beta}$) versus spectral analysis (DAMASK) predictions ($\overline{\sigma}_{\alpha\beta,Dam}$) for (a)$\overline{\sigma}_{22}$, (b)$\overline{\sigma}_{11}$, and (c)$\overline{\sigma}_{12}$. In part (b), 4 data points are below the shown range.

The overregulation of the spectral analysis is likely a factor that affects experiment-model comparison in the remaining plots of Figure 4.7 and Figure 4.8. Regardless though, if one just focuses on the y-axis (experimental data), the dispersion is clearly worse for $\tilde{S}_{11}$ and $\overline{\sigma}_{11}$ shown in Figure 4.7(b) and Figure 4.8(b). Area-weighted average of these yield -2.75 TPa^{-1} and -38 MPa, respectively; and neither really check out against the bulk behavior, the former yielding an effective Poisson's ratio of about 0.65 ($\neq$ 0.3) and the latter not coming close to the ideal 0. On the other hand, $\tilde{S}_{12}$ and $\overline{\sigma}_{12}$, both with ideal bulk values of zero, fare considerably better on their area-weighted averages, -0.44 TPa^{-1} and -5.5 MPa, each roughly an order below the corresponding axial values.

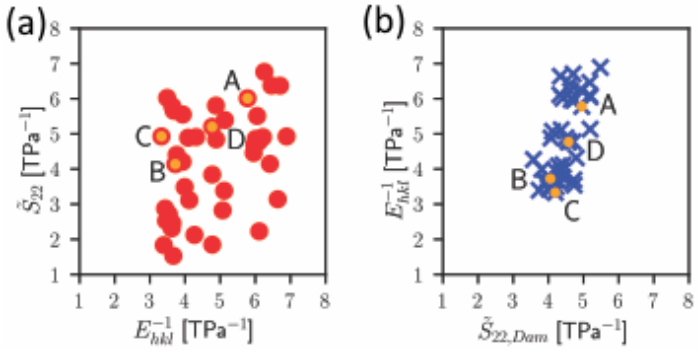

Figure 4.9. Effective axial compliance comparisons, (a) experimental versus isostress value, (b) spectral analysis (DAMASK) versus isostress value.

Though $\overline{\sigma}_{22}$ results will incur error from all stress slopes (including $\tilde{S}_{11}$), they also largely present bulk sanity, with an area-weighted average (87 MPa) within 20% of the nominal stress. In summary, the statistics of considerable grains is rare and, further, confidence is not uniform in such a set, as noted by a comparison to grain A. It is observed that obtaining accurate results is particularly testing in the transverse direction. In axial and in-plane shear components, the averages largely satisfy sanity checks.

5. EVALUATION OF GRAIN-RESOLVED PLASTIC DEFORMATION

5.1. Plastic Deformation Heterogeneity

Recall that the tensile test is combined with macro-DIC imaging to monitor macroscopic deformation in real time. At desired strain levels, the area-scanning micro-DIC data collection (a much lengthier process) is performed by sending the sample under the microscopic optics using automated setup software. In this section, we first reveal the entire loading curve of the experiment in Figure 5.1 where the applied stress is plotted against the field-averaged macro-DIC uniaxial strain values. In this loading regime, unload at about 0.6% in Figure 5.1 has already been considered in great detail regarding the evaluation of elastic strain and stress (Section 4). The focus of this section is on the more appreciable plastic strains that are induced after this segment. In the plastic straining phase, three deformation stages are reported in this treatise, at 1.65%, 3.34% and 5%, highlighted with red markers in Figure 5.1. Note that an approximately uniform increase in plastic deformation (about 1.65%) is induced between each step.

The distribution of E_{hkl} (Equation 2.6) and the absolute maximum Schmid factor (Equation 2.12) are shown in Figure 5.2, as supplementary information about the aggregate. E_{hkl} shows an expected distribution that covers both the theoretical maximum values ($\sim$ 303 GPa) and the minimum values ($\sim$ 137 GPa) for pure nickel. A similar distribution is also seen for the calculated absolute maximum Schmid factors, where the values of maximum (0.5) and minimum (0.28) are in good agreement with the theoretical ones.

The length-scales of mechanical fields have been categorized previously as type-I (aggregate average), type-II (intergranular), and type-III (intragranular). The tensile curve (Figure 5.1) shows a typical type-I measurement that represents a generic macroscopic or field average measurement. The strain maps, which retain the full micro-DIC

resolution of the study, show type-III data. Figures 5.3, 5.4, and 5.5 show this type of map for the strain components ε_{22}, ε_{11}, and ε_{12}, respectively. These are provided only at the macroscopic 5% load point for brevity. Each plot is overlaid with the stitched image to investigate strain over different morphological features. x_1 and x_2 correspond to the horizontal and vertical directions (respectively) in these maps, with the loading direction aligned with x_2.

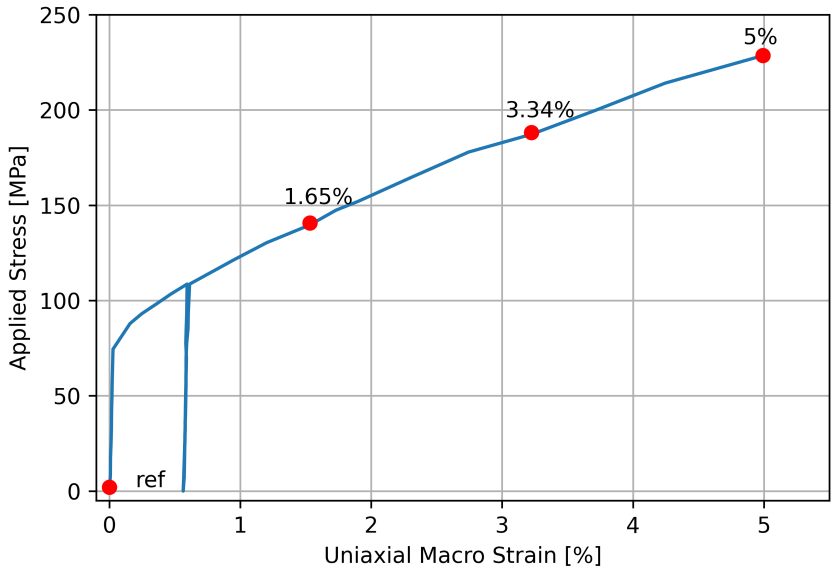

Figure 5.1. Applied stress vs macro strain curve with highlighted reference and deformed DIC points.

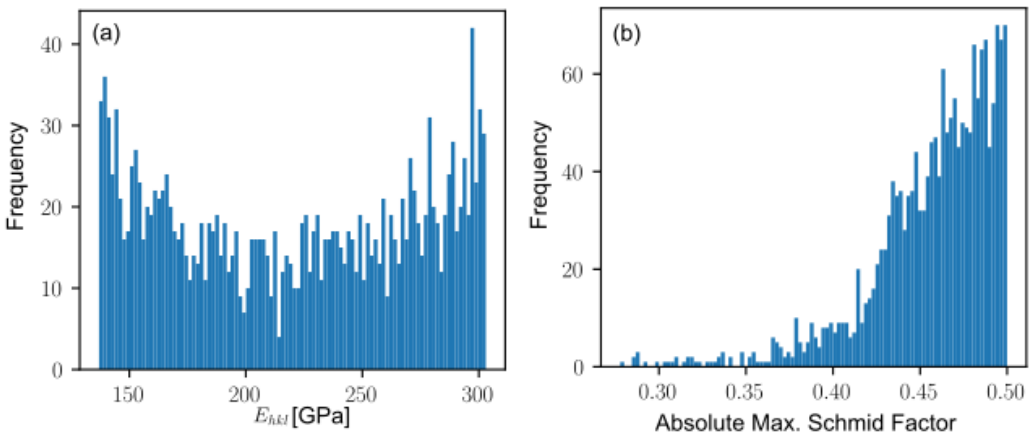

Figure 5.2. Histograms of (a) E_{hkl} and (b) absolute maximum Schmid factor.

The data shown in these maps are again subjected to outlier removal (see Section 3.7.2.4) with sigma-clipping. However, it is known that the intragrain plastic strain distributions can be even more localized than the elastic strain distributions. To avoid discarding physical data points, instead of the 3 times standard deviation (which has been utilized in the elastic data evaluation), outlier removal limits are extended to 4 times the standard deviation (i.e., for ε_{22} strain signal, limits are $\langle\overline{\varepsilon}_{22}\rangle \pm 4 \times \text{std}$, note that $\langle\overline{\varepsilon}_{22}\rangle$ is the full-field average). Nevertheless, only very limited data, 0.01% are removed for all strain components with this criterion, and the field response of these components is gathered accurately after these removals.

In the case of ε_{22} field map (Figure 5.3), average strain over the micro-DIC domain is calculated as 4.97% (in perfect consistency with the macro-DIC average) with a standard deviation of 1.8%. High standard deviation is a sign of strain heterogeneity, which is visible on the map with severe strain localizations. These localizations have a tendency to be aligned with morphological features, e.g., grain boundaries and triple points. Some of the localization bands also reveal slip traces within crystallites attesting to the intragrain resolution will be shown more clearly with local maps in Section 5.4.

The map ε_{11} (Figure 5.4) shows localizations similar to the map ε_{22}. As expected, on average, it has a negative strain about -2.48% with a standard deviation of 1.5%. Compared to ε_{22}, the apparent Poisson ratio ($\nu = -\frac{\langle\overline{\varepsilon}_{11}\rangle}{\langle\overline{\varepsilon}_{22}\rangle}$) of the field averages has a value of 0.49 which agrees very well with the theoretical ratio of 0.5 for the isochoric plasticity of (transversely) isotropic aggregates. In case of ε_{11} field response, there are multiple zones with a positive strain response (opposite to the expected Poisson effect). In case of uniaxial loading of a single crystal, it is not possible to observe positive ε_{11} strains. However, during polycrystal deformation, numerous factors can cause the formation of a positive ε_{11} signal. Complex neighborhood interactions with different stiffness grains and the existence of a free surface could be considered to be the main factors behind the formation of these positive ε_{11} at relatively large plastic deformation level (5% uniaxial loading).

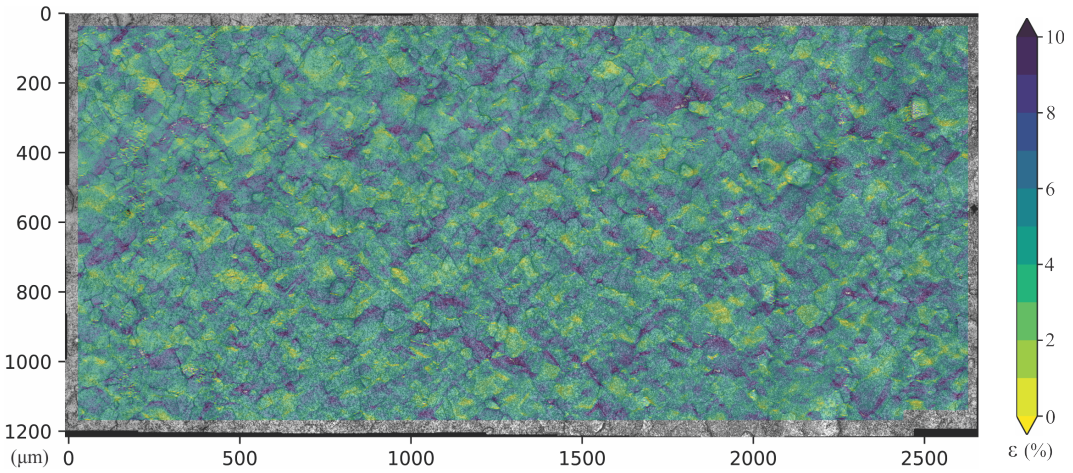

Figure 5.3. Full field ε_{22} map on 5% average uni-axial macro strain

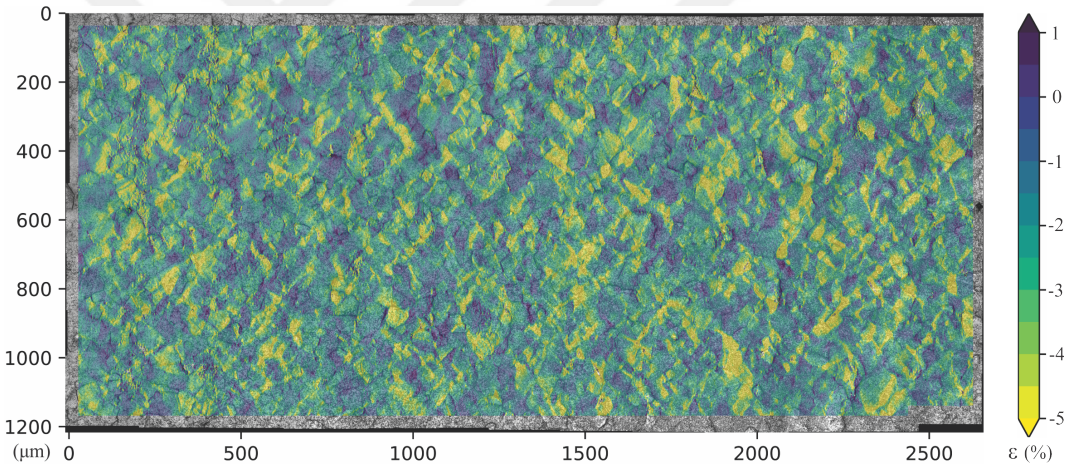

Figure 5.4. Full field ε_{11} map on 5% average uni-axial strain

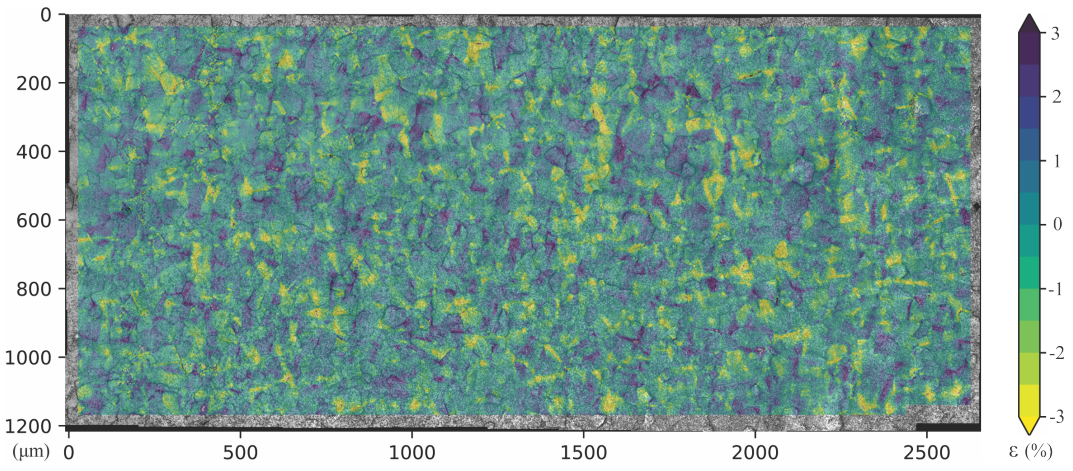

Figure 5.5. Full field ε_{12} map on 5% average uni-axial strain

5.2. Grain-Resolved Plasticity

Type II fields, or, namely, grain-averaged fields, are also investigated for plastic strains. Mean crystallite strain is the most basic measure that can describe strain sharing among crystallites while providing additional insight, particularly in a statistical context. Fortunately, the framework of this thesis provides the grain masks (see Section 3.6.2) that enables singling out grains. Also, crystallographic orientations gathered from EBSD analysis can be projected to each grain to have directional mechanical properties and Schmid factors. Approximately 4000 grains in the full field region are taken into account; however, only 2000 of them have reliable orientation data in terms of confidence index (see Section 3.6.1) and distinguishable geometry.

The grain-averaged (type-II) strain maps at 5% macroscopic strain are calculated by utilizing grain mask (Section 3.6.2) and plotted in Figures 5.6, 5.7 and 5.8 for axial, transverse, and shear strains, respectively. As the grain averages are determined, the outermost data layer in each grain is again stripped (see Section 3.7.2.5) to eliminate subsets that are excessively shared with neighbor grains (in the extreme, consider a subset (61x61 pixels) that is centered at a triple point that has information from 3 different grains).

All these figures clearly show heavy strain heterogeneity among grains. For each component of the strain ($\overline{\varepsilon}_{22}$, $\overline{\varepsilon}_{11}$ and $\overline{\varepsilon}_{12}$), the area-weighted field averages are calculated as 5.01%, -2.46% and -0.12%, respectively, with the corresponding standard deviations per grain, 1.56%, 1.35% and 1.03%, respectively. When these type-II standard deviations are compared with the standard deviations at full (1 μm) resolution (previous section), the standard deviation decreases in the type-II results (the expected smoothing effect of averaging). However, area-weighted strain averages are in good agreement with micro-DIC field averages.

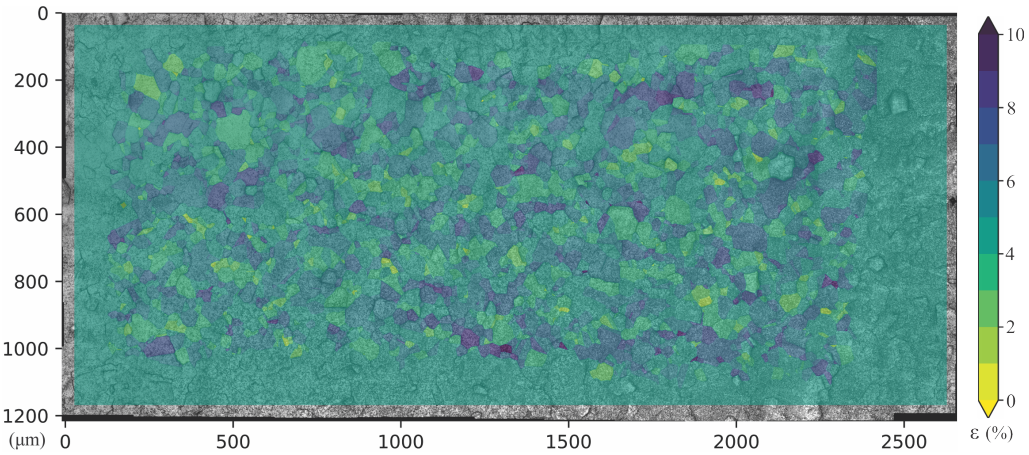

Figure 5.6. Grain-averaged $\overline{\varepsilon}_{22}$ map at 5% average uni-axial strain

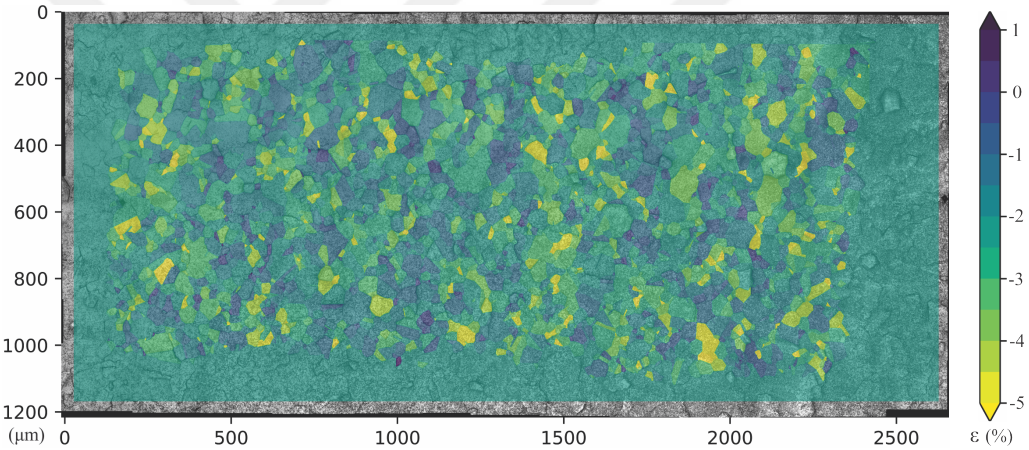

Figure 5.7. Grain-averaged $\overline{\varepsilon}_{11}$ map at 5% average uni-axial strain

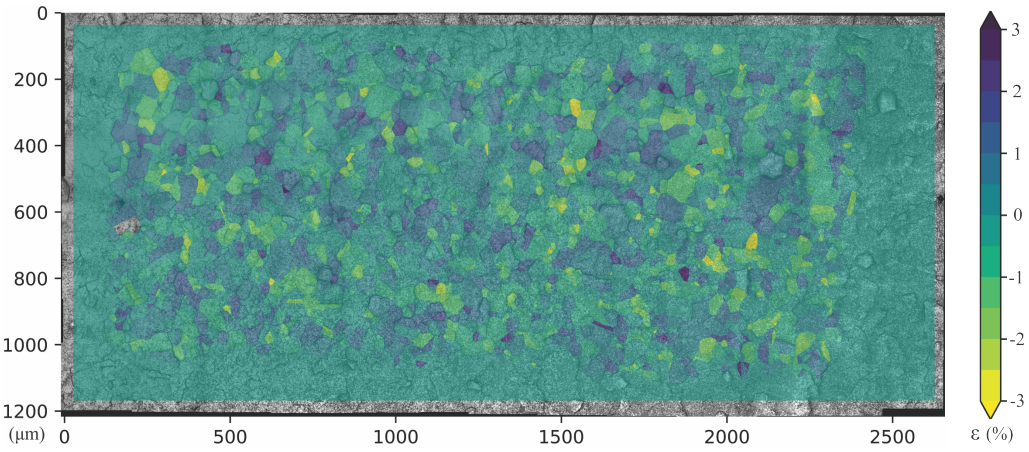

Figure 5.8. Grain-averaged $\overline{\varepsilon}_{12}$ map at 5% average uni-axial strain

5.3. Statistical Interpretations on Grain-Resolved Plasticity

Having a grain-averaged strain signal and crystallographic orientation for nearly 2000 grains allows us to seek trends in these statistically significant results. The grain-averaged strain distribution for each plastic deformation point (Figure 5.1) is given in Figure 5.9. In these figures, the evolution of grain-averaged strain distributions over the three load points is investigated. In Figure 5.9, the columns correspond to macroscopic uniaxial strain at 1.65%, 3.34%, 5% and rows correspond to grain-averaged axial normal strain, transverse normal strain and in-plane shear strains. In the case of, axial strain, $\overline{\varepsilon}_{22}$ (Figure 5.9(a-c)), although histograms have similar shapes, the range of strains increases as the distributions naturally shift toward the positive side with increasing mean strains. A similar behavior is observed for transverse normal strain, $\overline{\varepsilon}_{11}$ (Figure 5.9(d-f)) but in the negative sense. As mentioned in Section 5.1, some of the positive ε_{11} clusters make grain averages ($\overline{\varepsilon}_{11}$) positive as well, yielding a limited number of grains with positive $\overline{\varepsilon}_{11}$. On the other hand, the evolution of in-plane shear strain, $\overline{\varepsilon}_{12}$ distribution (Figure 5.9(g-i)) shows an expanding behavior on both directions. Although this behavior is a coherent sign of plastic deformation heterogeneity, the mean value and the median value of the distribution remain close to zero, indicating macroscopic adherence to the uniaxial mechanical fields. To quantify, the full-field average shear strain ($\langle\overline{\varepsilon}_{12}\rangle$=$-0.14\%$ at 5% uniaxial deformation) is relatively small and close to zero.

5.3.1. Directional Elastic Stiffness versus Strains

Another statistical trend that we will investigate using type-II fields is the association between directional elastic stiffness vs. grain-averaged strain. The directional elastic stiffness, namely E_{hkl} (stiffness that is aligned with the loading direction of the specimen), can be calculated by crystallographic orientation of the grain (Equation 2.6). Then, scatter plots of E_{hkl} versus $\overline{\varepsilon}_{22}$ (Figure 5.10(a-c)) are produced at each load point. For each plot, a trend line (1D linear fit) is also added to the figures to provide the sense of the behavior (whether increasing, decreasing, or constant). In

addition to the trend line, interval averages are plotted with an error bar. To calculate interval averages, data is divided with equal spacing (30 steps) of E_{hkl} and the error bar represents ± the standard deviation of each interval. A noticeable negative trend (showing a decreasing $\overline{\varepsilon}_{22}$ strain with increasing E_{hkl}) is observed even after the plastic strains become dominant, which is the anticipated behavior but with a serious degree of scatter.

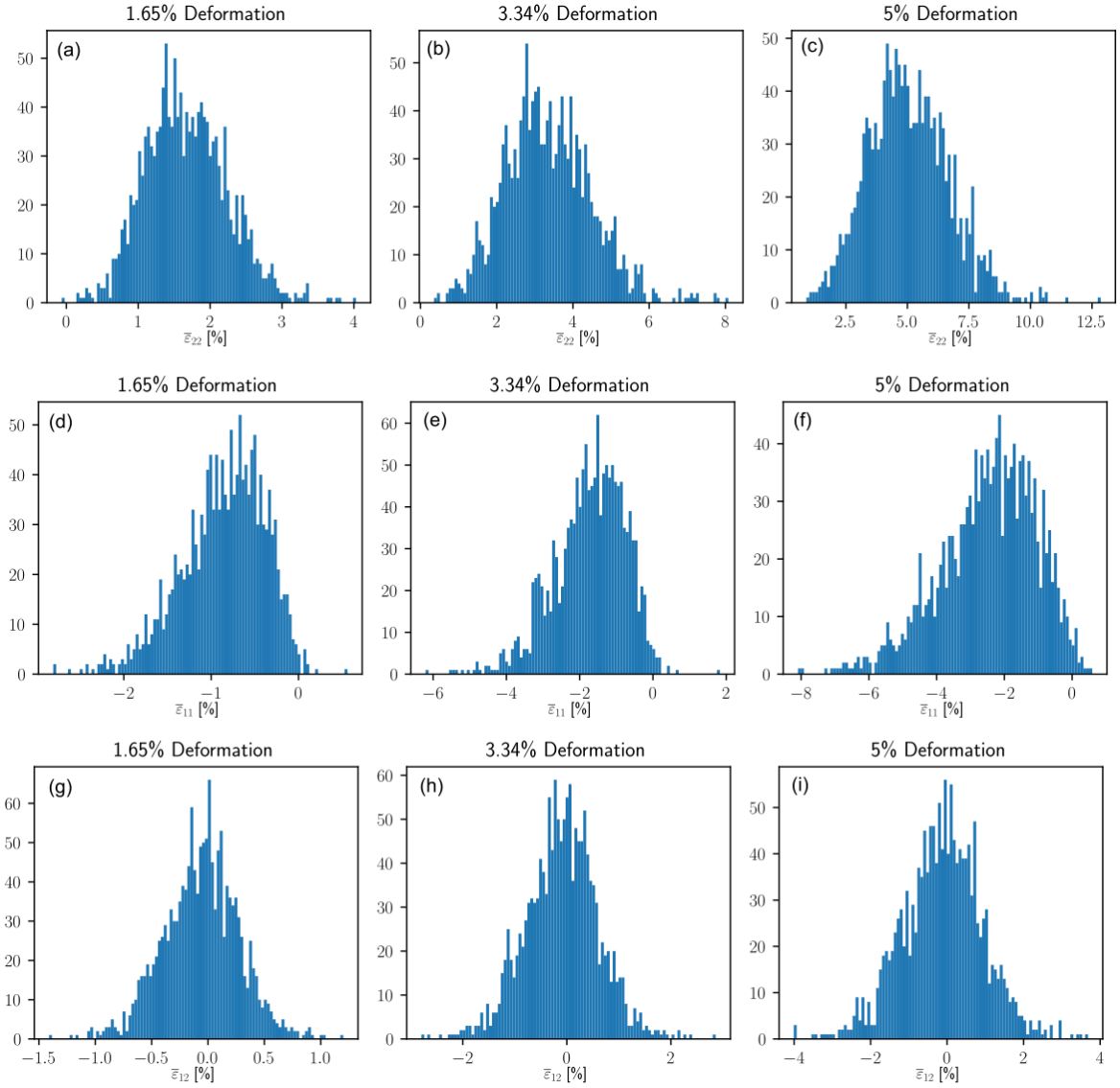

Figure 5.9. Strain distribution evolution (a-c) $\overline{\varepsilon}_{22}$, (d-f) $\overline{\varepsilon}_{11}$, (g-i) $\overline{\varepsilon}_{12}$

In the case of $\overline{\varepsilon}_{11}$ (Figure 5.10(d-f)) versus E_{hkl}, though the trend is not as significant, there is a positive correlation that strengthens with increasing deformation.

Although the 1.65% deformation shows a slight slope for $\overline{\varepsilon}_{11}/\mathrm{E}_{hkl}$, at the 5% deformation, the trend becomes steeper and visible to the naked eye. Furthermore, the scatter plots of E_{hkl} versus $\overline{\varepsilon}_{12}$ are provided in Figure 5.10(g-i) with no significant trends. The trend lines stay around "0" shear strain which is an expected behavior of the bulk during the tensile test.

Lastly, the scatter of the E_{hkl} versus $\overline{\varepsilon}_{maxsh}$ (Equation 3.4) scatter is given in Figure 5.10(j-l) which shows similar trends as $\overline{\varepsilon}_{22}$ and $\overline{\varepsilon}_{11}$. This behavior also strengthens the notion that grains with high directional elastic stiffness are likely to have less plastic strain compared to grains with low elastic stiffness values while providing additional insights.

5.3.2. Schmid Factor versus Strains

The next statistical trend we will investigate is absolute maximum Schmid factor versus type-II strains. With the celebrated Schmid law, the Schmid factor determines which slip system will be resolved in a higher stress state (assuming that the type-I uniaxial stress state holds locally). In a polycrystal, it has been observed that second or rarely third absolute maximum SF slip systems are also activated instead of slip system with the absolute maximum SF (likely due to the lack of information on the actual local stress state).

The scatter plots in Figure 5.11 depict the relationship between the absolute maximum Schmid factor and the type-II strain components. We find only a limited trend between SF and grain-averaged strains. $\overline{\varepsilon}_{11}$ vs. m_{max} and $\overline{\varepsilon}_{maxsh}$ vs. m_{max} have more significant trends than other strain components. These trends shows that grains with a low absolute maximum Schmid factor generally tend to have less strain compared to others.

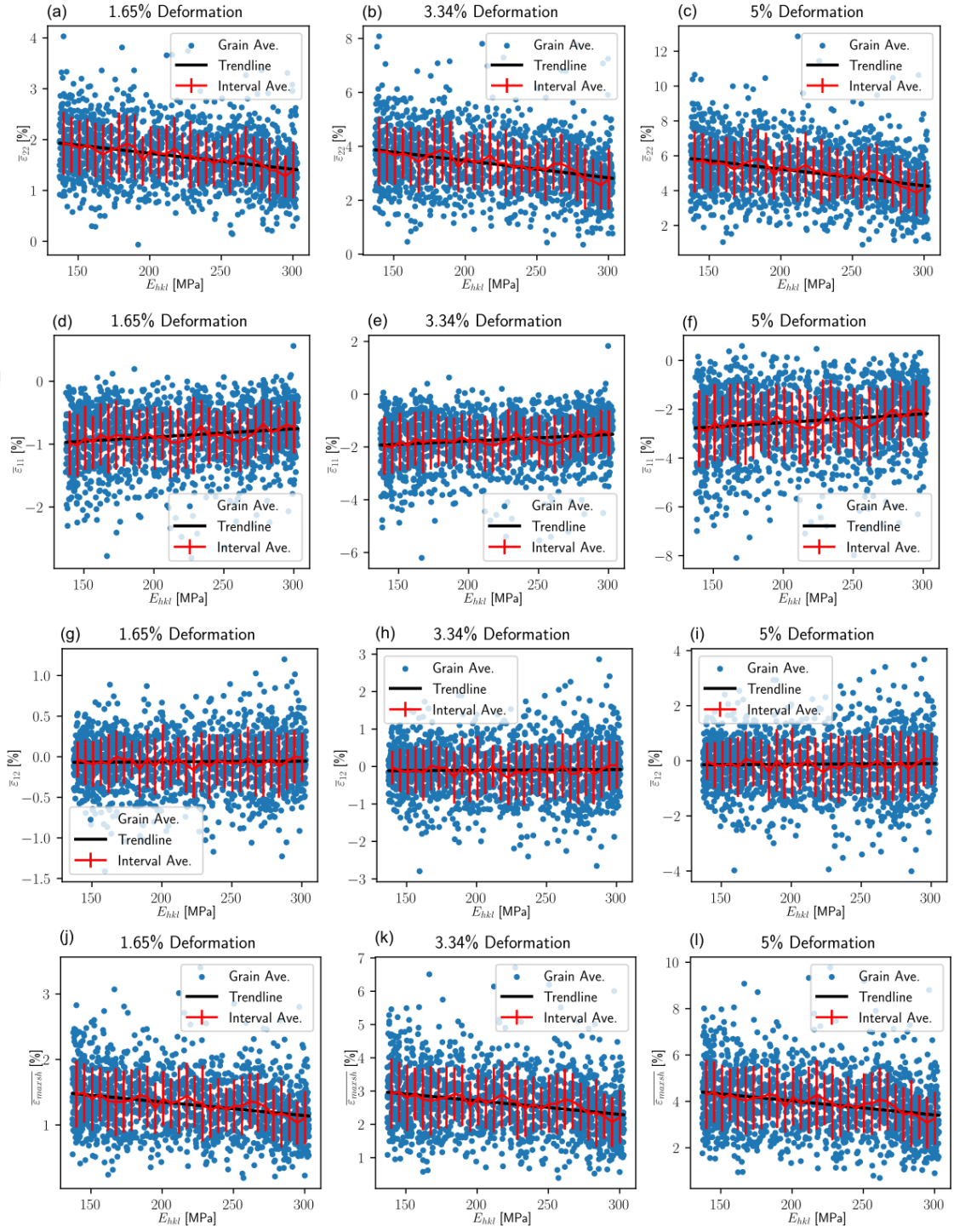

Figure 5.10. Evolution of plastic strain vs directional stiffness (a-c) E_{hkl} vs $\overline{\varepsilon}_{22}$, (d-f) E_{hkl} vs $\overline{\varepsilon}_{11}$, (g-i) E_{hkl} vs $\overline{\varepsilon}_{12}$, (j-l) E_{hkl} vs $\overline{\varepsilon}_{maxsh}$

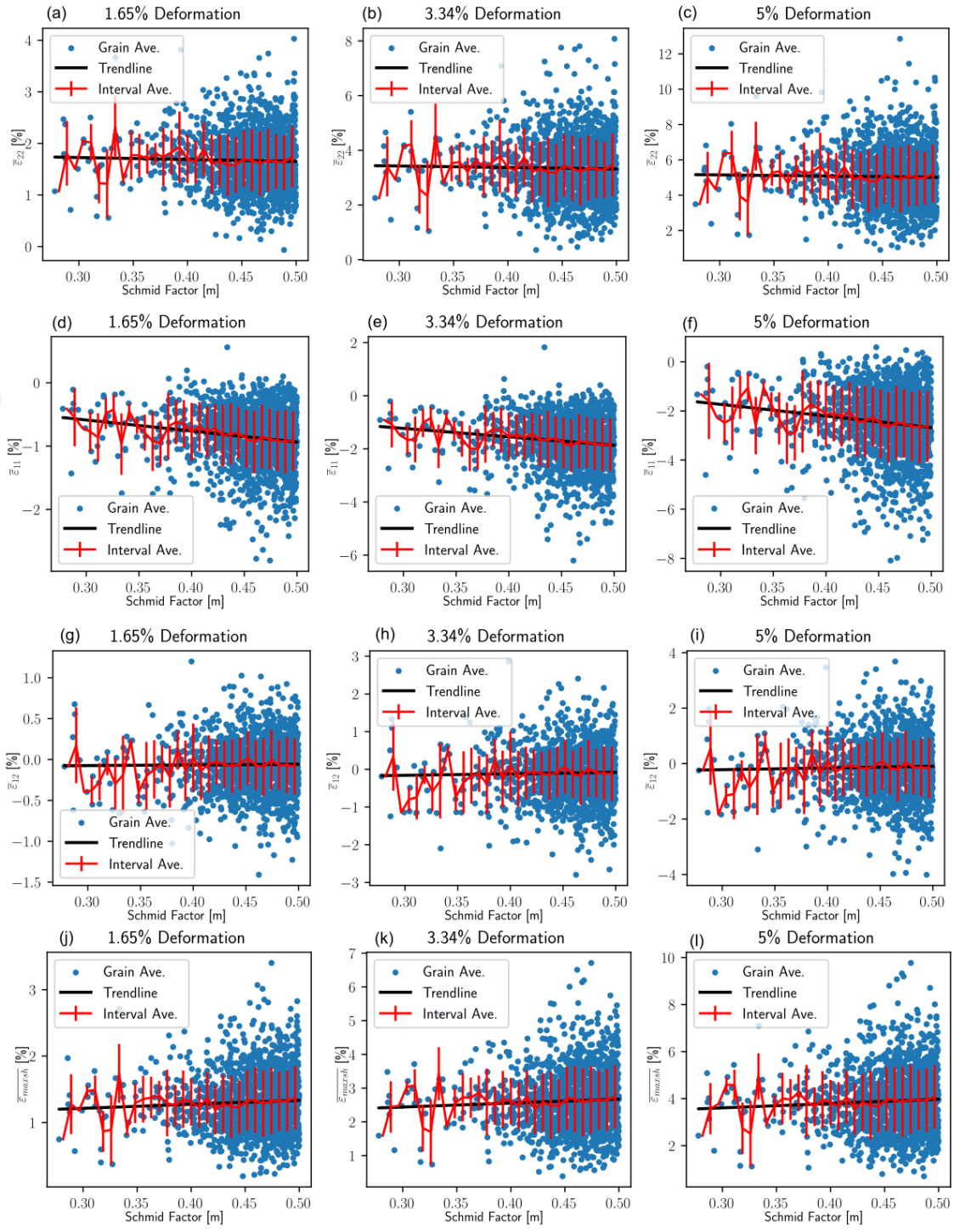

Figure 5.11. Evolution of plastic strain vs absolute maximum Schmid factor (a-c) absolute maximum SF vs $\overline{\varepsilon}_{22}$, (d-f) absolute maximum SF vs $\overline{\varepsilon}_{11}$, (g-i) absolute maximum SF vs $\overline{\varepsilon}_{12}$

5.3.3. Area versus Strains

In terms of morphological characteristics, the trends with the grain area are explored in Figure 5.12. The plots are made with the square root of the grain area, which crudely corresponds to the grain size in μm. While the deformation is evolving, the association between grain areas and grain-averaged strain remains constant. The only distinguishable observation is that grains with relatively large areas tend to exhibit less strain variations, and their strain levels are very close to the average strain of the bulk. Although Hall-Petch behavior defines that polycrystals tend to have a higher yield strength with respect to decreasing average grain sizes (between different polycrystalline aggregates, not within the individual aggregate). That is why observed trends are not direct proofs/disproofs for Hall-Petch behavior, and additionally most of the smaller grains have strains similar to the average of the bulk.

5.3.4. Core versus Boundary Strain

In literature, there are some studies [35, 36], [53] that mention higher strain accumulation over grain boundaries. To attest to this notion, the average boundary and average total strains of each grain are statistically investigated. Already used method of grain stripping (binary erosion, see Section 3.7.2.5) is utilized to collect strain data for the boundary segments of each grain. A better measure for strain differences ($\Delta\epsilon = \epsilon_{core} - \epsilon_{boundary}$) is also introduced for each grain to display strain variations that enables native comparison of boundary vs. core strain of the grains.

To assess the localization of strains, all grains are stripped for a single layer (1 μm thickness, because this is the smallest resolution of the DIC analysis). Then, average strains are calculated for this stripped-off layer, which is called the boundary segment, and also calculated for the rest of the grain, which is called the core of the grain. Due to the different grain sizes, area of the grain boundary segment / total grain area ratio is in the range of 5-60% on the entire aggregate (the average ratio is 20%). Then, the strain differences are calculated and shown in Figure 5.13.

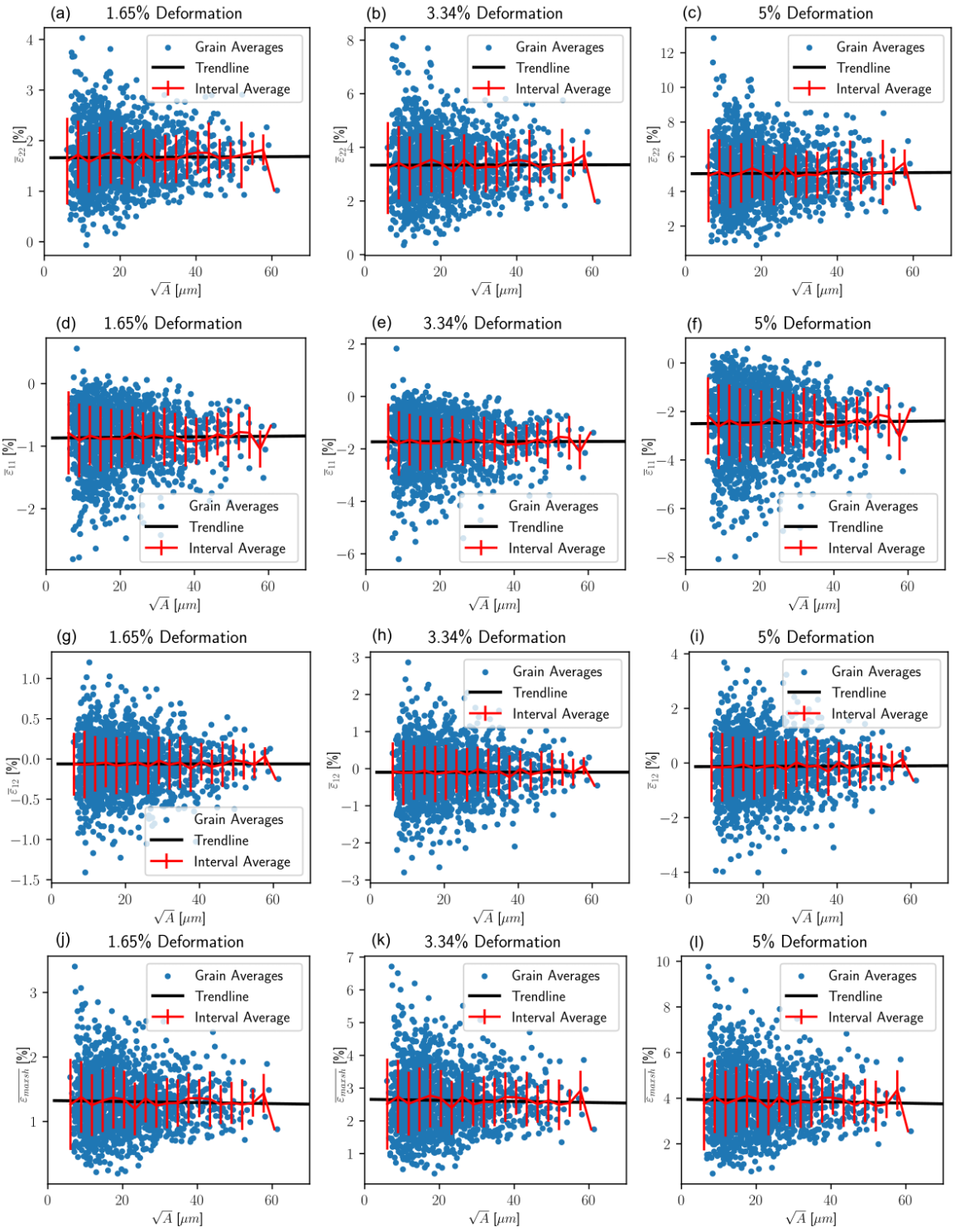

Figure 5.12. Evolution of plastic strain vs Area (a-c) Area vs $\overline{\varepsilon}_{22}$, (d-f) Area vs $\overline{\varepsilon}_{11}$, (g-i) Area vs $\overline{\varepsilon}_{12}$

In the case of $\Delta\bar{\varepsilon}_{22}$, $\Delta\bar{\varepsilon}_{11}$ and $\Delta\bar{\varepsilon}_{12}$, (Figure 5.13(a-i)) it is observed that with increasing deformation, the range of strain differences increases; however, it is difficult to mention that there are higher strains over the boundary segments of grains. The mean and the median values of the strain distributions observed in this study are approximately zero. But it is clear that in some grains there are strain localizations over the boundaries, whether it is higher or lower than the average strain of the core. Additionally, $\Delta\bar{\varepsilon}_{maxsh}$ (Figure 5.13(j-l)) is considered as a measure of the localization of the deformation; however, the findings are similar to those of the above-mentioned strains.

Finally, trends are searched for the rotation of the boundary and core segments of grains. As discussed in the introduction, a study on plastic deformation of pure nickel suggested that grain with larger areas accommodates to deformation by rotating rather than straining. However, in Figure 5.14(a-c), it is seen that grains with larger areas do not necessarily show this behavior; on the contrary, most larger grains show rotations similar to those of smaller ones. Note that the horizontal axis of the figure is the percentage of the boundary area over the total area of the grain, providing additional information about stripping, which causes the variety of the percentage value (Note that larger grains has low core vs boundary ratios.). Furthermore, by referring to Figure 5.13(m-o), distribution of the rotation difference is similar to the strain differences.

5.4. Intragrain Plasticity

The previous section (section 5.3) considers only type-II (grain-averaged) strain results; however, having a grain mask, orientation, and intragranular resolution enables this study to explore type-III deformation results over the grain domains. In particular, slip trace identification with the novel residual intensity parameter (Section 3.7.4) provides complementary morphological results with high spatial resolution within a grain. The sample results for a representative grain-I with a 3270 μm^2 area are given at 5% uniaxial deformation in Figure 5.15.

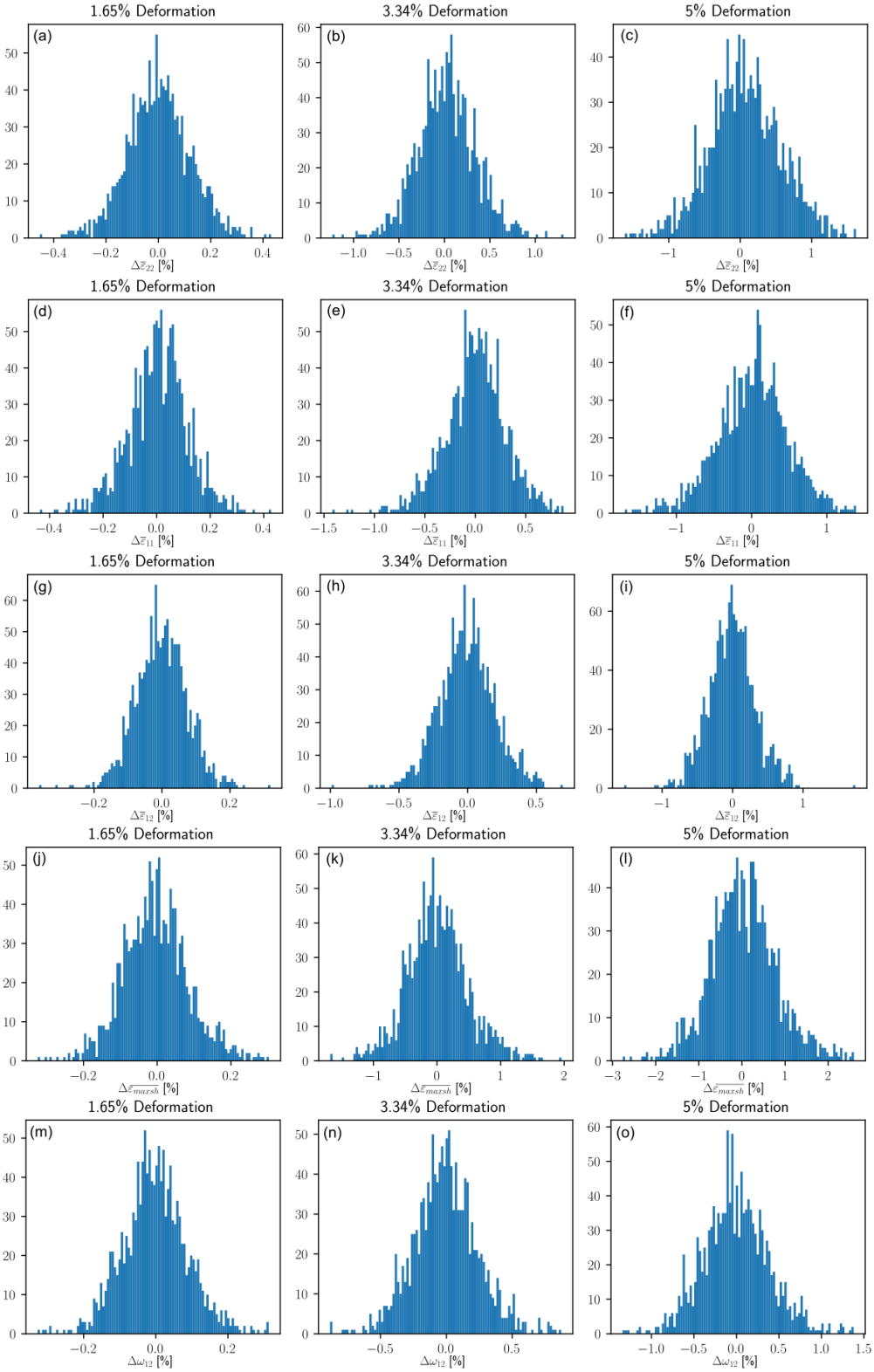

Figure 5.13. Strain difference (core strain - boundary strain) distribution evolution (a-c) $\Delta\overline{\varepsilon}_{22}$, (d-f) $\Delta\overline{\varepsilon}_{11}$, (g-i) $\Delta\overline{\varepsilon}_{12}$, (j-l) $\Delta\overline{\varepsilon}_{maxsh}$, (m-o) $\Delta\overline{\omega}_{12}$

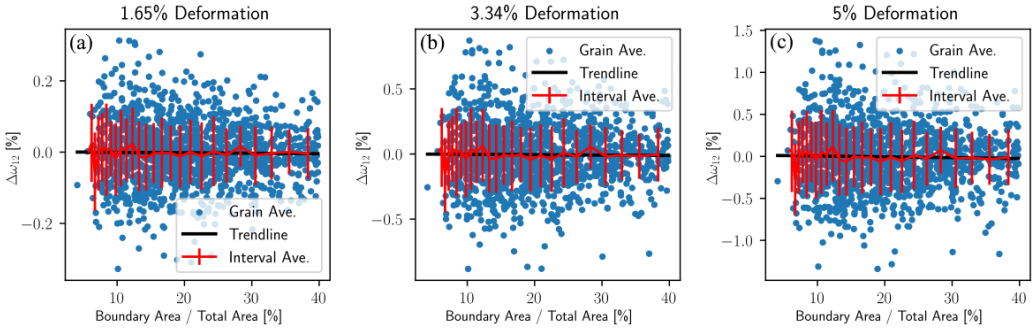

Figure 5.14. Average difference in rotation (a-c), $\Delta\overline{\omega}_{12}$ of the boundary and core of the grains vs boundary area / total area. (Note that larger grains have smaller boundary area/total area ratios after a single layer strip-off.)

The most significant morphological intragrain finding is the activated slip system in the grain (Grain-I), shown in Figure 5.15(a). This image is generated using the residual intensity method. It shows slip traces not only within the center grain but also discernible traces over the neighbors. Using the crystallographic orientation, the SFs of all 12 slip systems for this grain are calculated (Table 5.4). The calculated slip planes (the four planes of the $\langle 111 \rangle$ family) are then projected over the image with different colors. For example, the red line represents the slip plane associated with the absolute maximum SF (as indicated in the first row of the table), while the orange line corresponds to the slip plane of the second highest SF system (second row in the table), and the white lines represent the third and fourth rows of the table. The slip plane traces generated via residual intensity and those calculated slip planes exhibit complete alignment, offering confirmation for the successful integration of EBSD and micro-DIC.

The strain response of the Grain-I is gathered from a total of 3270 subsets by comparing reference (Figure 5.15(d)) and deformed image. Although the DIC analysis does not have enough resolution to provide strain localizations over the slips detected on the residual intensity map, the strain signal (Figure 5.15(b-c) and (e-h)) within the grain still shows evident heterogeneity and localization. For example, in the case of ε_{22}, the grain-averaged strain, $\overline{\varepsilon}_{22}$ is 4.65% with a standard deviation of 1.6%. While the upper left zone of the grain is receiving nearly 3% strain, some of the lower parts

are receiving a strain signal of nearly 6%. In addition, in the case of ε_{11} and ε_{12}, there is clear evidence of strain accumulations over or near grain boundaries, for example, the right grain boundary has less ε_{11} strain (approximately -1%) while the upper boundary has a higher magnitude (approximately -4%). All of these preliminary findings represent a modest attempt at type-III deformation results over this large data set. More grains will be investigated in the future work of this study.

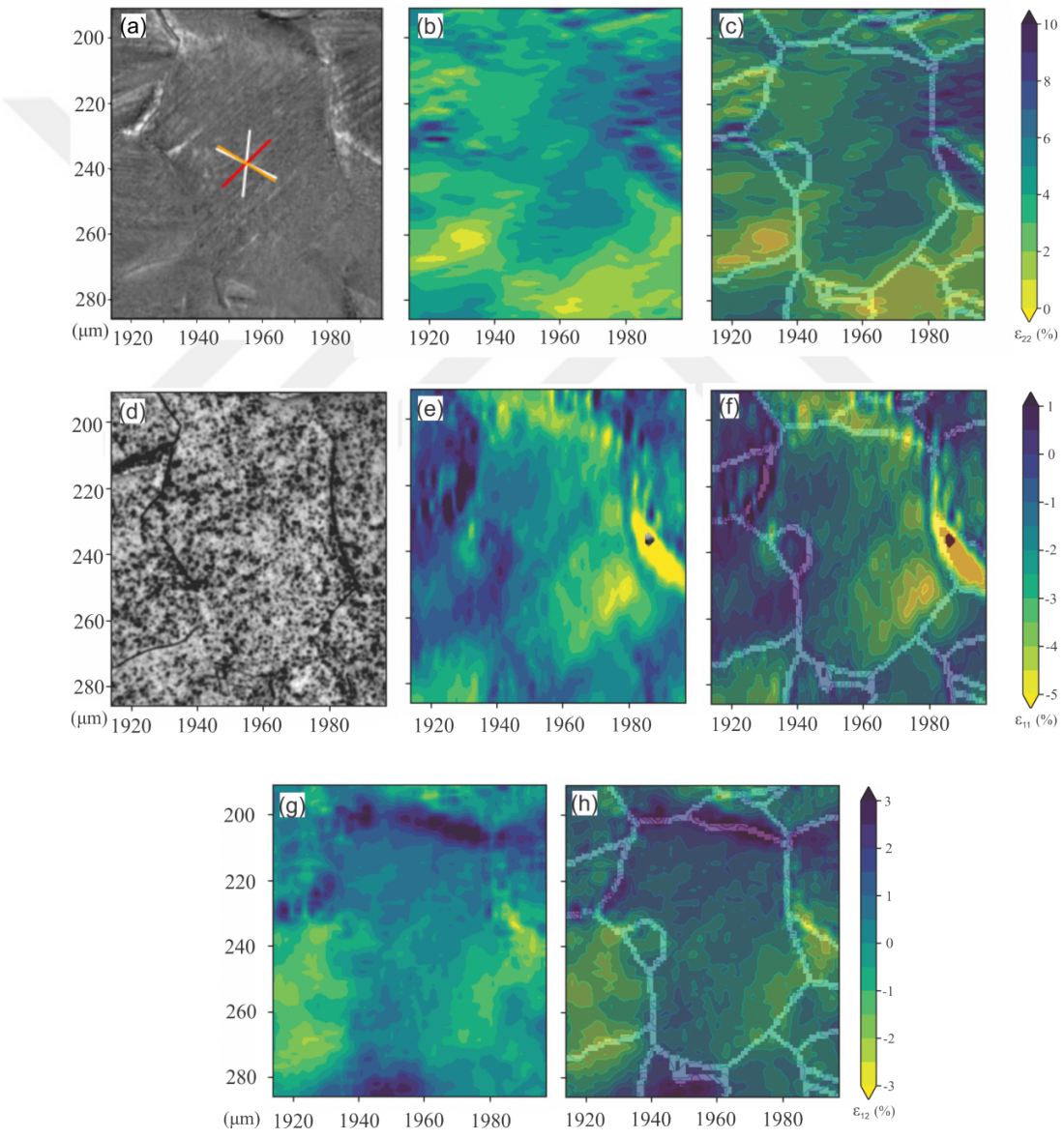

Figure 5.15. Grain-I (a) Residual intensity map. The red line shows the trace of the slip plane of the slip system with absolute maximum SF (Table 5.4) while orange shows the second, (b-c) ε_{22} at 5% uniaxial deformation, (d) DIC reference image, (e-f) ε_{11} map at 5% uniaxial deformation, (g-h) ε_{12} map at 5% uniaxial deformation.

Although slip might be expected over the slip system with the largest absolute maximum SF, some of the grains do not always comply. For example, Grain-II in Figure 5.16, in this particular grain, the slip is accumulated over the second maximum SF slip system instead of the first (see Table 5.4) (note that local stress state is unknown and this particular slip system may have the highest resolved shear stress, τ_{RSS}). The alignment of the calculated (from reciprocal space measurement, EBSD) slip system (second absolute maximum SF) has a perfect match with the signal that comes from the residual intensity channel (real space measurement, optical imaging).

Table 5.1. Slip systems of Grain-I in the domain (Ordered with respect to absolute maximum SF).

No.	**Schmid Factor**	**Slip Plane (CCS)**	**Slip Direction (CCS)**	**Slip Plane (SCS)**	**Slip Direction (SCS)**
1	0.487	$(1,-1,1)$	$[1,0,-1]$	$(0.62,-0.63,0.46)$	$[0.78,0.5,-0.38]$
2	-0.452	$(-1,1,1)$	$[1,0,1]$	$(-0.84,0.09,0.53)$	$[0.51,-0.17,0.84]$
3	0.391	$(1,1,-1)$	$[1,-1,0]$	$(0.44,0.9,-0.08)$	$[0.90,-0.44,-0.04]$
4	-0.336	$(-1,1,1)$	$[1,1,0]$	$(-0.84,0.09,0.53)$	$[0.4,0.76,0.51]$
5	0.248	$(1,-1,1)$	$[1,1,0]$	$(0.62,-0.63,0.46)$	$[0.4,0.76,0.51]$
6	-0.239	$(1,-1,1)$	$[0,1,1]$	$(0.62,-0.63,0.46)$	$[-0.38,0.27,0.88]$
7	0.224	$(1,1,-1)$	$[1,0,1]$	$(0.44,0.9,-0.08)$	$[0.51,-0.17,0.84]$
8	0.194	$(1,1,1)$	$[1,-1,0]$	$(0.22,0.35,0.91)$	$[0.90,-0.44,-0.04]$
9	0.169	$(1,1,1)$	$[1,0,-1]$	$(0.22,0.35,0.91)$	$[0.42,-0.52,-0.74]$
10	-0.167	$(1,1,-1)$	$[0,1,1]$	$(0.44,0.9,-0.08)$	$[0.38,0.27,0.88]$
11	0.096	$(-1,1,1)$	$[0,1,-1]$	$(-0.84,0.09,0.53)$	$[-0.11,0.93,-0.34]$
12	-0.025	$(1,1,1)$	$[0,1,-1]$	$(0.22,0.35,0.91)$	$[-0.11,0.93,-0.34]$

The residual intensity channel is providing a complementary and better resolution signal than DIC (while the DIC resolution is limited with subset-size and spacing, the residual intensity channel provides resolution per pixel). This complementary signal also provides some insight about out-of-plane deformation. For example, at the

upper right boundary of Grain II, there is no boundary information on the residual intensity image, which is an expected result (see reference [70]) and show that there is no deformation on this particular boundary. However, in the lower left boundary, some protrusion or intrusion (out-of-plane or into-plane motion sense is not known.) is observed, which is clear evidence of relative out-of-plane deformation over the boundary segment among grains because no grain boundaries normally show in the residual intensity image due to substractive nature of this method (see reference [70]).

During the SF calculation, the grain loading direction is chosen as the loading direction of the bulk; however, a single grain in the polycrystalline aggregate might have a much more complex loading condition due to the effects of neighboring grains and surface condition. This behavior is already observed in the literature and is not surprising, but having a large number of grains with perfectly identified slip traces might provide statistically significant insights about grain interactions during deformation, which will be one of the main topics of future work of this study.

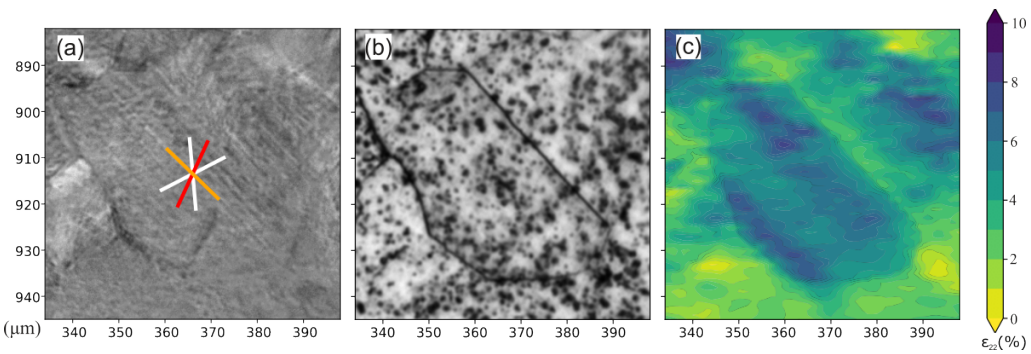

Figure 5.16. Grain-II (a) Residual intensity map. The red line shows the trace of the slip plane of the slip system with absolute maximum SF (Table 5.4) while orange shows the second and white lines, third and fourth ones (b) DIC reference image, (c) ε_{22} map over the grain domain at 5% uniaxial deformation.

Table 5.2. Slip systems of Grain-II in the domain (Ordered with respect to absolute maximum SF).

No.	**Schmid Factor**	**Slip Plane (CCS)**	**Slip Direction (CCS)**	**Slip Plane (SCS)**	**Slip Direction (SCS)**
1	0.463	$(1, 1, -1)$	$[1, 0, 1]$	$(0.64, 0.06, -0.77)$	$[0.73, 0.29, 0.62]$
2	0.458	$(1, 1, 1)$	$[1, 0, -1]$	$(0.84, 0.71, 0.19)$	$[0.67, -0.51, -0.54]$
3	0.406	$(1, -1, 1)$	$[1, 1, 0]$	$(0.50, -0.23, 0.83)$	$[0.81, 0.47, -0.36]$
4	0.401	$(1, 1, 1)$	$[1, -1, 0]$	$(0.68, 0.71, 0.19)$	$[0.59, -0.68, 0.44]$
5	0.374	$(1, 1, -1)$	$[1, -1, 0]$	$(0.64, 0.06, -0.77)$	$[0.59, -0.68, 0.44]$
6	0.37	$(-1, 1, 1)$	$[1, 1, 0]$	$(-0.46, 0.88, 0.12)$	$[0.81, 0.47, -0.36]$
7	0.34	$(1, -1, 1)$	$[1, 1, -1]$	$(0.50, -0.23, 0.83)$	$[0.67, -0.51, -0.54]$
8	-0.33	$(-1, 1, 1)$	$[1, 1, 1]$	$(-0.46, 0.88, 0.12)$	$[0.73, 0.29, 0.62]$
9	0.09	$(1, 1, -1)$	$[1, 1, 1]$	$(0.64, 0.06, -0.77)$	$[0.14, 0.97, 0.19]$
10	0.07	$(1, -1, 1)$	$[0, 1, 1]$	$(0.50, -0.23, 0.83)$	$[0.14, 0.97, 0.19]$
11	0.06	$(1, 1, 1)$	$[0, 1, -1]$	$(0.84, 0.71, 0.19)$	$[0.08, 0.18, -0.98]$
12	-0.04	$(-1, 1, 1)$	$[0, 1, -1]$	$(-0.46, 0.88, 0.12)$	$[0.08, 0.18, -0.98]$

6. CONCLUSIONS

This dissertation has emerged from the basic questions of polycrystal mechanics "How do grains share load and strain?" and "Is it possible to have accurate grain-resolved strain signal with OM-DIC?" and evolved into a vast study in the realm of OM-DIC by integrating and incorporating reciprocal space material field measurements with real space material field measurements.

One significant outcome of this study is the development of a framework that enables sampling results from different types of deformations (in the diffraction nomenclature: Type-I, Type-II and Type-III) by utilizing OM-DIC. Type-I deformation corresponds to field/aggregate average. Additionally, this framework has utilized a grain mask that has enabled sampling Type-II (grain-averaged) deformation results in both the elastic and plastic deformation regions. Finally, a relatively high resolution in-house OM-DIC setup has provided a modest sampling of Type-III (intragrain) deformation. The grain masking methodology that enables sampling strain signal per crystallite is introduced to obtain Type-II and Type-III results directly for a specific grain. The grain mask alone has only provided morphological information (revealing boundaries between grains with metallography) of the grains that has also combined with the crystallographic orientation of grains to utilize a statistical evaluation of deformation mechanics (both elasticity and plasticity) per crystallite. However, these objectives, of course, require a high spatial resolution and highly accurate microscopic DIC strain signal. To advance the resolution, accuracy, and field coverage of the OM-DIC, the experimental setup incorporated high numerical aperture optics, along with novel automated measures (auto-focusing and material field correction). Additionally, the speckle pattern (a primary factor in DIC accuracy) is introduced with a new methodology and with extreme caution.

The first achievement of the dissertation is the measurement of grain-averaged elastic deformation. Unloading (which is assumed to precipitate a purely elastic re-

sponse for the aggregate) with fine intervals during the tensile test allows us to uniquely evaluate the linearity of the response. Then, for each step, OM-DIC analysis is repeated by altering the DIC reference points to test the objectivity of the results. While providing variation of intragrain strain signals per load point and per reference point, this multi-reference-point OM-DIC analysis has then combined with a binary operation to average the strains over varying size domains of a grain, which is also named grain stripping in the dissertation. By introducing the statistical linearity measure of correlation, it has been observed that average elastic strain slopes per grain (for limited portion of grains) may converge towards a constant value, while averaging domain over the same material field increases per load point. Later, the aforementioned methods have been applied to calculate strain slopes with a sufficient precision to instigate a unique method to estimate the stress state of a crystallite.

The second achievement of the dissertation lies in the measurement of grain-resolved plastic deformation. OM-DIC has provided good accuracy in detecting strain heterogeneity over full-field. Then, with the introduction of the grain mask, the grain-averaged plastic strains were calculated, and certain statistical correlations between the grain-averaged strains and various crystallite features (area, axial stiffness, Schmid factor, etc.) were investigated. Furthermore, intragranular (Type-III) plastic deformations are revealed with OM-DIC. Predictions for activated slip systems are confirmed by the slip traces revealed with the novel residual intensity method. Additionally, this study has already provided statistically significant data for slip interaction between grains and the neighborhood for future research.

To sum up, this dissertation utilizes a method-driven innovative approach and integrated reciprocal space and real space measurements to provide statistical correlations in both elastic and plastic deformation fields over polycrystalline aggregates. The presented data and ideas offer bridging of length scales among type-I, type-II and type-III deformations results as well as new channels (such as the type-II grain stress) to improve fidelity of future polycrystalline models estimated from DIC.

REFERENCES

1. Hull, D. and D. J. Bacon, *Introduction to Dislocations*, 5th edn., Elsevier, Oxford, 2011.

2. Dowling, N., *Mechanical Behavior of Materials: Engineering Methods for Deformation, Fracture, and Fatigue*, Pearson, New York, 2013.

3. Dieter, G. E. and D. Bacon, *Mechanical Metallurgy*, Vol. 3, McGraw-hill, New York, 1976.

4. Freund, L. B. and S. Suresh, *Thin Film Materials*, Cambridge University Press, Cambridge, 2004.

5. Hertzberg, R. W., *Deformation and Fracture Mechanics of Engineering Materials*, 4th edn., J. Wiley & Sons, New York, 1996.

6. Zener, C. M. and S. Siegel, "Elasticity and Anelasticity of Metals.", *The Journal of Physical Chemistry*, Vol. 53, No. 9, pp. 1468–1468, 1949.

7. Caillard, D. and J.-L. Martin, "Glide of Dislocations in Non-octahedral Planes of fcc Metals: A Review", *International Journal of Materials Research*, Vol. 100, No. 10, pp. 1403–1410, 2009.

8. Schmid, E., "Bemerkungen über die Plastische Deformation von Kristallen", *Zeitschrift für Physik*, Vol. 22, No. 1, pp. 328–333, 1924.

9. Taylor, G. I., "Plastic Strain in Metals", *Journal of the Institute of Metals*, Vol. 62, pp. 307–324, 1938.

10. Bieler, T., R. Alizadeh, M. Peña-Ortega and J. Llorca, "An Analysis of (the lack of) Slip Transfer between Near-cube Oriented Grains in Pure Al", *International Journal of Plasticity*, Vol. 118, pp. 269–290, 2019.

11. Alizadeh, R., M. Peña-Ortega, T. Bieler and J. LLorca, "A Criterion for Slip Transfer at Grain Boundaries in Al", *Scripta Materialia*, Vol. 178, pp. 408–412, 2020.

12. Luster, J. and M. A. Morris, "Compatibility of Deformation in Two-phase Ti-Al Alloys: Dependence on Microstructure and Orientation Relationships", *Metallurgical and Materials Transactions A*, Vol. 26, No. 7, pp. 1745–1756, 1995.

13. Lin, Y., L. Han and G. Wang, "Relationship Between $\Sigma 3$ Boundaries, Dislocation Slip, and Plasticity in Pure Nickel", *Materials*, Vol. 16, No. 7, 2023.

14. Wei, Y. and L. Anand, "Grain-boundary Sliding and Separation in Polycrystalline Metals: Application to Nanocrystalline fcc Metals", *Journal of the Mechanics and Physics of Solids*, Vol. 52, No. 11, pp. 2587–2616, 2004.

15. Sachs, G., "Zur Ableitung einer Fliessbedingung", *Z. Ver, Dtsch. Ing.*, Vol. 72, pp. 734–736, 1928.

16. Reuß, A., "Berechnung der Fließgrenze von Mischkristallen auf Grund der Plastizitätsbedingung für Einkristalle.", *ZAMM-Journal of Applied Mathematics and Mechanics/Zeitschrift für Angewandte Mathematik und Mechanik*, Vol. 9, No. 1, pp. 49–58, 1929.

17. Kröner, E., "Kontinuumstheorie der Versetzungen und Eigenspannungen", *Angewandte Mathematik*, Vol. 5, pp. 1–179, 1958.

18. Budianski, B. and T. Te Wu, *Theoretical Prediction of Plastic Strains of Polycrystals*, No. 12, Harvard University, Cambridge, 1961.

19. Eshelby, J. D., "The Determination of the Elastic Field of an Ellipsoidal Inclusion, and Related Problems", *Proceedings of the royal society of London. Series A. Mathematical and physical sciences*, Vol. 241, No. 1226, pp. 376–396, 1957.

20. Hutchinson, J., "Elastic-plastic Behaviour of Polycrystalline Metals and Composites", *Proceedings of the Royal Society of London. A. Mathematical and Physical Sciences*, Vol. 319, No. 1537, pp. 247–272, 1970.

21. Clausen, B., T. Lorentzen and T. Leffers, "Self-consistent Modelling of the Plastic Deformation of f.c.c. Polycrystals and its Implications for Diffraction Measurements of Internal Stresses", *Acta Materialia*, Vol. 46, No. 9, pp. 3087–3098, 1998.

22. Hutchinson, J. W., "Bounds and Self-consistent Estimates for Creep of Polycrystalline Materials", *Proceedings of the Royal Society of London. A. Mathematical and Physical Sciences*, Vol. 348, No. 1652, pp. 101–127, 1976.

23. Becker, R., "Analysis of Texture evolution in Channel Die Compression—I. Effects of Grain Interaction", *Acta Metallurgica et Materialia*, Vol. 39, No. 6, pp. 1211–1230, 1991.

24. Mika, D. P. and P. R. Dawson, "Effects of Grain Interaction on Deformation in Polycrystals", *Materials Science and Engineering: A*, Vol. 257, No. 1, pp. 62–76, 1998.

25. Barbe, F., S. Forest and G. Cailletaud, "Intergranular and Intragranular Behavior of Polycrystalline Aggregates.Part 2: Results", *International Journal of Plasticity*, Vol. 17, No. 4, pp. 537–563, 2001.

26. Raabe, D., M. Sachtleber, Z. Zhao, F. Roters and S. Zaefferer, "Micromechanical and Macromechanical Effects in Grain Scale Polycrystal Plasticity Experimentation and Simulation", *Acta Materialia*, Vol. 49, No. 17, pp. 3433–3441, 2001.

27. Roters, F., P. Eisenlohr, T. R. Bieler and D. Raabe, *Crystal Plasticity Finite Element Methods*, Wiley-VCH, Weinheim, 2010.

28. Yaghoobi, M., S. Ganesan and S. Sundar, "PRISMS-plasticity: An Open-source Crystal Plasticity Finite Element Software", *Computational Materials Science*, Vol. 169, p. 109078, 2019.

29. Roters, F., P. Eisenlohr, C. Kords, D. Tjahjanto, M. Diehl and D. Raabe, "DAMASK: the Düsseldorf Advanced MAterial Simulation Kit for Studying Crystal Plasticity Using an FE Based or a Spectral Numerical Solver", *Procedia IUTAM*, Vol. 3, pp. 3–10, 2012.

30. Moulinec, H. and P. Suquet, "Fast Numerical Method for Computing the Linear and Nonlinear Properties of Composites", *Comptes Rendus de l'Académie des Sciences. Série II*, Vol. 318, pp. 1417–1423, 1994.

31. Lebensohn, R., "N-site Modeling of a 3D Viscoplastic Polycrystal Using Fast Fourier Transform", *Acta Materialia*, Vol. 49, pp. 2723–2737, 2001.

32. Brenner, R., R. Lebensohn and O. Castelnau, "Elastic Anisotropy and Yield Surface Estimates of Polycrystals", *International Journal of Solids and Structures*, Vol. 46, No. 16, pp. 3018–3026, 2009.

33. Eisenlohr, P., M. Diehl, R. A. Lebensohn and F. Roters, "A Spectral Method Solution to Crystal Elasto-viscoplasticity at Finite Strains", *International Journal of Plasticity*, Vol. 46, pp. 37–53, 2013.

34. Roters, F., M. Diehl, P. Shanthraj, P. Eisenlohr, C. Reuber, S. L. Wong, T. Maiti, A. Ebrahimi, T. Hochrainer, H. O. Fabritius, S. Nikolov, M. Friák, N. Fujita, N. Grilli, K. G. Janssens, N. Jia, P. J. Kok, D. Ma, F. Meier, E. Werner, M. Stricker, D. Weygand and D. Raabe, "DAMASK – The Düsseldorf Advanced Material Simulation Kit for Modeling Multi-Physics Crystal Plasticity, Thermal, and Damage

Phenomena from the Single Crystal up to the Component Scale", *Computational Materials Science*, Vol. 158, No. December 2018, pp. 420–478, 2019.

35. Aydıner, C. C. and M. A. Telemez, "Multiscale Deformation Heterogeneity in Twinning Magnesium Investigated With in situ Image Correlation", *International Journal of Plasticity*, Vol. 56, pp. 203–218, 2014.

36. Carroll, J., W. Abuzaid, J. Lambros and H. Sehitoglu, "An Experimental Methodology to Relate Local Strain to Microstructural Texture", *Review of Scientific Instruments*, Vol. 81, No. 8, p. 83703, 2010.

37. Zhao, Z., M. Ramesh, D. Raabe, A. M. Cuitiño and R. Radovitzky, "Investigation of Three-dimensional Aspects of Grain-scale Plastic Surface Deformation of an Aluminum Oligocrystal", *International Journal of Plasticity*, Vol. 24, No. 12, pp. 2278–2297, 2008.

38. Efstathiou, C., H. Sehitoglu and J. Lambros, "Multiscale Strain Measurements of Plastically Deforming Polycrystalline Titanium: Role of Deformation Heterogeneities", *International Journal of Plasticity*, Vol. 26, pp. 93–106, 2010.

39. Kammers, A. D. and S. Daly, "Digital Image Correlation under Scanning Electron Microscopy: Methodology and Validation", *Experimental Mechanics*, Vol. 53, p. 1743–1761, 2013.

40. Ross, F. M., *Microscopic Strain Localization and Damage in Multi-phase Alloys*, Ph.D. Thesis, Massachusetts Institute of Technology, 2022.

41. Shafaghi, N., E. Kapan and C. C. Aydıner, "Cyclic Strain Heterogeneity and Damage Formation in Rolled Magnesium via in situ Microscopic Image Correlation", *Experimental Mechanics*, Vol. 60, p. 735–751, 2020.

42. Kapan, E., N. Shafaghi, S. Uçar and C. C. Aydıner, "Texture-dependent Character of Strain Heterogeneity in Magnesium AZ31 under Reversed Loading", *Materials Science and Engineering A*, Vol. 684, pp. 706–711, 2017.

43. Stinville, J.-C., M. Echlin, D. Texier, F. Bridier, P. Bocher and T.M.Pollock, "Sub-Grain Scale Digital Image Correlation by Electron Microscopy for Polycrystalline Materials during Elastic and Plastic Deformation", *Experimental Mechanics*, Vol. 56, pp. 197–216, 02 2016.

44. Goulmy, J., D. Depriester, F. Guittonneau, L. Barrallier and S. Jégou, "Mechanical Behavior of Polycrystals: Coupled in situ DIC-EBSD Analysis of Pure Copper under Tensile Test", *Materials Characterization*, Vol. 194, p. 112322, 2022.

45. Latypov, M. I., J.-C. Stinville, J. R. Mayeur, J. M. Hestroffer, T. M. Pollock and I. J. Beyerlein, "Insight into Microstructure-sensitive Elastic Strain Concentrations from Integrated Computational Modeling and Digital Image Correlation", *Scripta Materialia*, Vol. 192, pp. 78–82, 2021.

46. Stinville, J., M. Charpagne, F. Bourdin, P. Callahan, Z. Chen, M. Echlin, D. Texier, J. Cormier, P. Villechaise, T. Pollock and V. Valle, "Measurement of Elastic and Rotation Fields during Irreversible Deformation Using Heaviside-digital Image Correlation", *Materials Characterization*, Vol. 169, p. 110600, 2020.

47. Aydıner, C. C., D. W. Brown, N. A. Mara, J. Almer and A. Misra, "In situ X-ray Investigation of Freestanding Nanoscale Cu–Nb Multilayers under Tensile Load", *Applied Physics Letters*, Vol. 94, No. 3, p. 031906, 2009.

48. Diehl, M., P. Shanthraj, P. Eisenlohr and F. Roters, "Neighborhood Influences on Stress and Strain Partitioning in Dual-phase Microstructures: An Investigation on Synthetic Polycrystals with a Robust Spectral-based Numerical Method", *Meccanica*, Vol. 51, No. 2, pp. 429–441, 2015.

49. Githens, A., S. Ganesan, Z. Chen, J. Allison, V. Sundararaghavan and S. Daly, "Characterizing Microscale Deformation Mechanisms and Macroscopic Tensile Properties of a High Strength Magnesium Rare-earth Alloy: A Combined Experimental and Crystal Plasticity Approach", *Acta Materialia*, Vol. 186, pp. 77–94, 2020.

50. Türkoğlu, O. and C. C. Aydıner, "Enabling Digital Image Correlation with High-Resolution Microscopic Optics via Working Distance Automation: Advancing Resolution and Accuracy Limits", *SEM2022: Advancements in Optical Methods, Digital Image Correlation & Micro-and Nanomechanics*, Vol. 4, pp. 49–56, Springer International Publishing, Cham, 2023.

51. Lim, H., J. Carroll, C. Battaile, T. Buchheit, B. Boyce and C. Weinberger, "Grain-scale Experimental Validation of Crystal Plasticity Finite Element Simulations of Tantalum Oligocrystals", *International Journal of Plasticity*, Vol. 60, pp. 1–18, 2014.

52. Máthis, K., G. Csiszár, J. Čapek, J. Gubicza, B. Clausen, P. Lukáš, A. Vinogradov and S. Agnew, "Effect of the Loading Mode on the Evolution of the Deformation Mechanisms in Randomly Textured Magnesium Polycrystals – Comparison of Experimental and Modeling Results", *International Journal of Plasticity*, Vol. 72, pp. 127–150, 2015.

53. Ashby, M. F., "The deformation of plastically non-homogeneous materials", *The Philosophical Magazine: A Journal of Theoretical Experimental and Applied Physics*, Vol. 21, No. 170, pp. 399–424, 1970.

54. Üçel, İ. B., E. Kapan, O. Türkoğlu and C. C. Aydıner, "In situ Investigation of Strain Heterogeneity and Microstructural Shear Bands in Rolled Magnesium AZ31", *International Journal of Plasticity*, Vol. 118, p. 233–251, 2019.

55. Raabe, D., M. Sachtleber, H. Weiland and G. Scheele, "Grain-scale Micromechanics of Polycrystal Surfaces during Plastic Straining", *Acta Materialia*, Vol. 51, pp. 1539–1560, 2003.

56. Padilla, H. A., J. Lambros, A. J. Beaudoin and I. M. Robertson, "Relating Inhomogeneous Deformation to Local Texture in Zirconium through Grain-scale Digital Image Correlation Strain Mapping Experiments", *International Journal of Solids and Structures*, Vol. 49, p. 18–31, 2012.

57. Wu, G. L., A. Godfrey, D. J. Jensen and Q. Liu, "Deformation Strain Inhomogeneity in Columnar Grain Nickel", *Scripta Materialia*, Vol. 53, No. 5, pp. 565–570, 2005.

58. Wu, G. L., A. Godfrey, G. Winther, D. Juul Jensen and Q. Liu, "Evolution of Orientations and Deformation Structures within Individual Grains in Cold Rolled Columnar Grained Nickel", *Acta Materialia*, Vol. 59, No. 14, pp. 5451–5461, 2011.

59. Wu, X., H. Suo, Y. Ji, J. Li, L. Ma, M. Liu, Z. Zhang and Q. Wang, "Systematical Analysis on the Grain Orientation Evolution of Pure Nickel under Plastic Deformation by Using in-situ EBSD", *Materials Science and Engineering A*, Vol. 792, No. 7, p. 139722, 2020.

60. Zhao, Y., X. Liao, Y. Zhu, Z. Horita and T. Langdon, "Influence of Stacking Fault Energy on Nanostructure Formation under High Pressure Torsion", *Materials Science and Engineering: A*, Vol. 410-411, pp. 188–193, 2005.

61. Murr, L. E., *Interfacial Phenomena in Metals and Alloys*, Addison-Wesley, Boston, 1975.

62. Vander Voort, G., *Metallography, Principles and Practice*, ASM International, New York, 1999.

63. Liu, X. Y., R. L. Li, H. W. Zhao, T. H. Cheng, G. J. Cui, Q. C. Tan and G. W. Meng, "Quality Assessment of Speckle Patterns for Digital Image Correlation by Shannon Entropy", *Optik*, Vol. 126, No. 23, pp. 4206–4211, 2015.

64. Field, D. P., "Recent Advances in the Application of Orientation Imaging", *Ultramicroscopy*, Vol. 67, No. 1-4, pp. 1–9, 1997.

65. Bradski, G., "The OpenCV Library", *Dr. Dobb's Journal of Software Tools*, Vol. 120, pp. 122–125, 2000.

66. Pan, B., K. Li and W. Tong, "Fast, Robust and Accurate Digital Image Correlation Calculation Without Redundant Computations", *Experimental Mechanics*, Vol. 53, pp. 1277–1289, 2013.

67. Blaber, J., "Digital Image Correlation Algorithms", 2015, `https://www.ncorr.com/index.php/dic-algorithms`, accessed on August 1, 2023.

68. Sutton, M. A., J.-J. Orteu and H. W. Schreier, *Image Correlation for Shape, Motion and Deformation Measurements: Basic Concepts, Theory and Applications*, Springer, New York, 2010.

69. Pan, B., "Full-field Strain Measurement Using a Two-dimensional Savitzky-Golay Digital Differentiator in Digital Image Correlation", *Optical Engineering*, Vol. 46, p. 033601, 3 2007.

70. Özdür, N. A., I. B. Üçel, J. Yang and C. C. Aydıner, "Residual Intensity as a Morphological Identifier of Twinning Fields in Microscopic Image Correlation", *Experimental Mechanics*, Vol. 61, pp. 499–514, 2020.

71. Preibisch, S., S. Saalfeld and P. Tomancak, "Globally Optimal Stitching of Tiled 3D Microscopic Image Acquisitions", *Bioinformatics*, Vol. 25, No. 11, pp. 1463–1465, 2009.

72. Rueden, C. T., J. Schindelin, M. C. Hiner, B. E. DeZonia, A. E. Walter, E. T. Arena and K. W. Eliceiri, "ImageJ2: ImageJ for the Next Generation of Scientific Image Data", *BMC Bioinformatics*, Vol. 18, No. 1, p. 529, 2017.

73. Virtanen, P. and et al., "SciPy 1.0: Fundamental Algorithms for Scientific Computing in Python", *Nature Methods*, Vol. 17, pp. 261–272, 2020.

74. Acciaioli, A., G. Lionello and M. Baleani, "Experimentally Achievable Accuracy Using a Digital Image Correlation Technique in Measuring Small-magnitude (<0.1%) homogeneous strain fields", *Materials*, Vol. 11, No. 5, pp. 1–14, 2018.

75. Haddadi, H. and S. Belhabib, "Use of Rigid-body Motion for the Investigation and Estimation of the Measurement Errors Related to Digital Image Correlation Technique", *Optics and Lasers in Engineering*, Vol. 46, No. 2, pp. 185–196, 2008.

76. Astropy Collaboration and et al., "The Astropy Project: Sustaining and Growing a Community-oriented Open-source Project and the Latest Major Release (v5.0) of the Core Package", *The Astrophysical Journal*, Vol. 935, No. 2, p. 167, 2022.

77. Groeber, M. A. and M. A. Jackson, "DREAM.3D: A Digital Representation Environment for the Analysis of Microstructure in 3D", *Integrating Materials and Manufacturing Innovation*, Vol. 3, p. 56–72, 2014.

APPENDIX A: ON THE SPECTRAL ANALYSIS PARAMETERS AND IMPLEMENTATION

The reader is referred to Reference [34] for further details. The simplified form of the crystal plasticity stress relation in which these parameters can be observed is as follows

$$\dot{\xi}^{\alpha} = {h_0}^{s-s}(1 + h^{\alpha}_{\text{int}}) \times \sum_{\alpha'=1}^{N_s} \left|\dot{\gamma}^{\alpha'}\right| \left|1 - \frac{\xi^{\alpha'}}{\xi^{\alpha'}_{\infty}}\right|^{a} \text{sgn}\left(1 - \frac{\xi^{\alpha'}}{\xi^{\alpha'}_{\infty}}\right) h^{\alpha\alpha'} \tag{A.1}$$

where α' is the index for slip systems.

$\dot{\gamma_0}$: Reference strain rate,

ξ_0 : Initial slip-system resistance,

ξ_∞ : Bounding slip-system resistance (max. slip-system resistance),

h_0 : Initial hardening,

n : Stress exponent,

a : Hardening exponent.

The 3-D image of the analysis domain is shown in Figure A.1, with a grain map (generated from EBSD data directly) and with axial stress fields at point T of the paper. The major point of this figure is to show the columnar grain morphology that, by definition, does not match the unknown subsurface morphology of the polycrystal at hand.

To better portray the stresses, planar contour plots are provided in the following figures in a central region of the domain shown in Figure A.1. This crop improves the resolution of the plots as they appear on the document. The model has ($3\mu m$ voxels) intragranular resolution and it automatically outputs type-III results as shown in Figure A.2. Normally, type-II stresses need to be only calculated from the type-III model fields, but to help with visualization, we generated a type-II plot as well in Figure A.3. Here, the fields are grain-averaged and these values are assigned to the voxels.

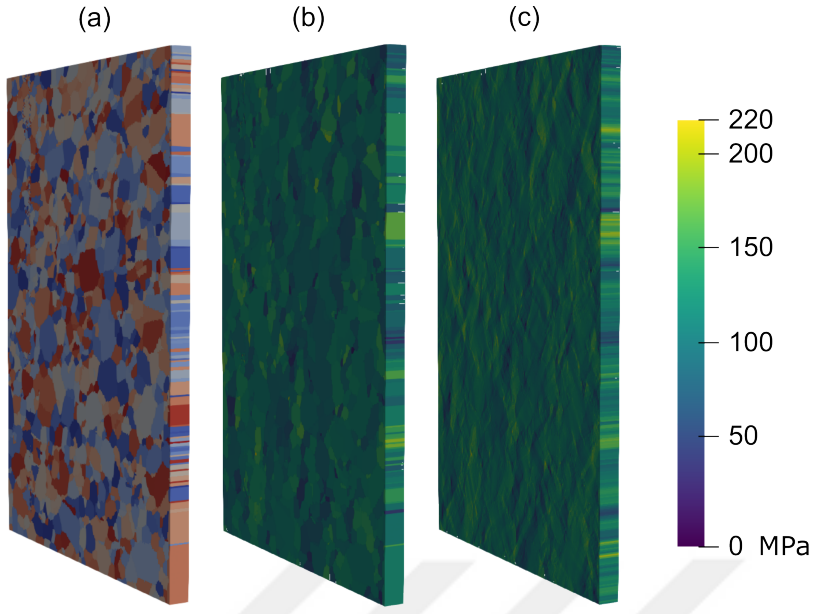

Figure A.1. Representative description of the columnar grain spectral analysis (a) grain map that is directly constructed from EBSD, (b) type-II (grain-averaged) stress, $\overline{\sigma}_{22}$ and (c) type-III stress, σ_{22} results at point T (where stress, σ_{22} in maps are aligned with loading (vertical) direction)

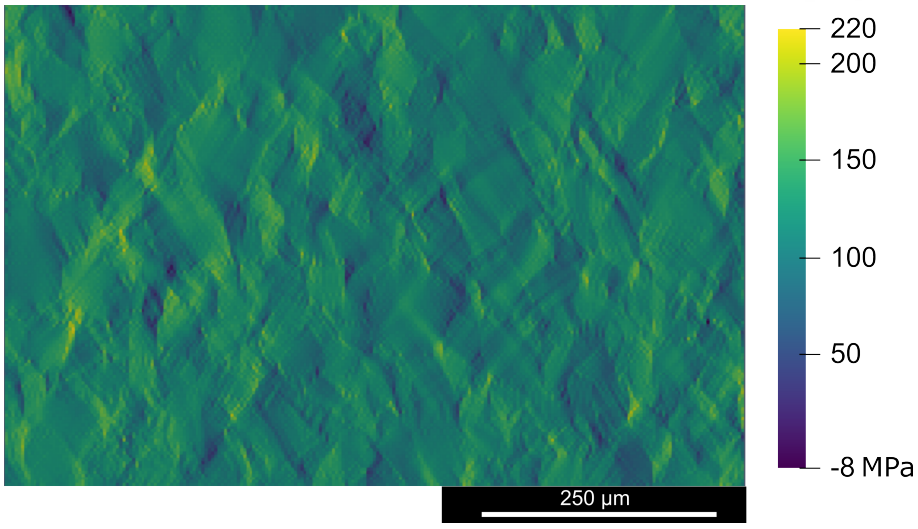

Figure A.2. DAMASK simulation, Type-III stress, σ_{22} results for selected region at point T.

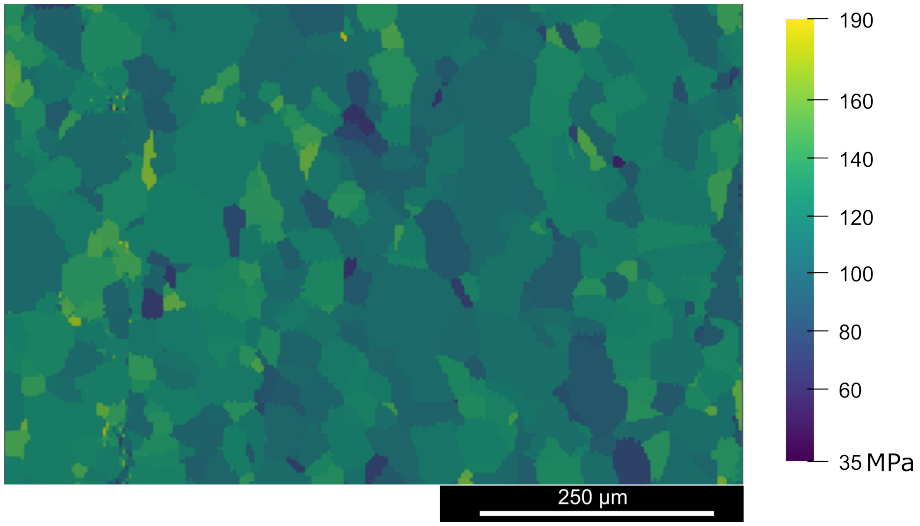

Figure A.3. Type-II (grain-averaged) stress, $\overline{\sigma}_{22}$ post-processed from Figure A.2.

APPENDIX B: COPYRIGHTS

All adopted/reused figures are captioned with citations. The following figures have copyright permissions under the license order numbers of 5721900416977 for Figure 2.3 [41], 572023027277 for Figure 2.5 [37], 5720221508764 for Figure 2.6 [56], 5720221350754 for Figure 2.7 [59], 5720221097567 for Figure 2.8 [45] and 1445907-1 for Figure 3.6 [69], which are officially obtained from copyright.com.

All other figures and illustrations belong to the author. Some of the images that emerged in this thesis study and were transferred to the publisher's copyright were used in accordance with the publisher's policy on the reuse of the author's own writings and graphics found on the publisher's own network page.